UNIVERSITY OF SOUTHAMPTON

Modelling the Controls on Melt Generation During Continental Extension and Breakup

by

John J. Armitage

A thesis submitted in partial fulfillment for the
degree of Doctor of Philosophy

in the
Faculty of Engineering, Science and Mathematics
School of Ocean & Earth Sciences

December 2008

UNIVERSITY OF SOUTHAMPTON

ABSTRACT

FACULTY OF ENGINEERING, SCIENCE AND MATHEMATICS
SCHOOL OF OCEAN & EARTH SCIENCES

Doctor of Philosophy

MODELLING THE CONTROLS ON MELT GENERATION DURING
CONTIENTAL EXTENSION AND BREAKUP

by John J. Armitage

Rifting is the process that leads to the formation of oceans. Rifting is the break up of continents, leading to the formation of new oceanic floor between the two continental plates. Although the concept of continental rifting is accepted within the scientific community, it is still debated what controls the volume and composition of igneous material generated at these constructive plate boundaries. Here I present the results of dynamic modelling of rifted margins. I have explored the consequences of margin and mantle structure on the melt generated during continental extension and breakup. The central aim is to understand how melting affects the rifting of continents, especially in the North Atlantic. In order to understand the enigmatic melt production observed around the North Atlantic various tools are developed for interpreting the model output. These are predictions of primary major element composition of the melt, rare-earth element composition of the melt, predictions of the crystallised mid-oceanic ridge basalt composition and the seismic velocity of the lower crust.

The thickness of the lithosphere has a very large impact on the subsequent rifting style. Extension of a $125\,km$ thick thermally and rheologically defined lithosphere that has no prior thinning produces little melt during breakup. The Southeast Greenland margin rifted above a pre-thinned lithosphere and at initial fast half spreading rates. Furthermore, to generate the thickness, chemistry and seismic velocities observed off this margin, rifting was coincident with the arrival of a $50\,km$ thick, $200\,°C$ thermal anomaly. This thermal anomaly is not a plume, rather an exhaustible thermal layer that has drained along the sub-lithospheric topography from a distal plume. The melts generated are high in MgO, and depleted in TiO. They are depleted in rare-earth elements. This would lead to high seismic velocities within the underplate being, as observed off Southeast Greenland.

Contents

List of Figures

List of Tables

Declaration

I, John Armitage, declare that this thesis is the result of work done wholly or mainly by myself while in canditure for a research degree at the University of Southampton.

Acknowledgements

I would like to thank firstly my supervisors, Tim Henstock, Tim Minshull and John Hopper. Also, without the support of Lidia and my family I would never have completed this work. I would also like to thank Caroline Scott, Donna Shillington and Simon Dean for helping with various requests for advice and help. Finally I thank Caroline, Klaus and Julia for numerous coffee breaks, without which no work would ever be done.

Nomenclature

A	stiffness matrix	
B	discrete gradient operator	
c_p	specific heat capacity, $\mathrm{J\,kg^{-1}\,K^{-1}}$	1200
$C(F)$	weight percent primary melt composition, %	
C_l	weight percent melt/liquid composition, %	
Cr	finite element Courant number for model stability	
C_s	weight percent solid residue composition, %	
$\mathscr{C}$	point average primary melt composition, %	
d	depth of model space, km	700
D	composition partition coefficient	
E	activation energy, $\mathrm{J\,mol^{-1}}$	530×10^3
F	melt fraction	
f	vector of body and boundary forces	
g	acceleration of gravity, $\mathrm{m\,s^{-2}}$	9.8
h	finite element spacing	
h_c	thickness of igneous crust, km	
k	diffusivity	
k_ϕ	permeability coefficient	
$K_{\overline{D}}$	partition coefficient of olivine/liquid	
K	bulk moduli	
L	latent heat of melting	
$\dot{m}$	dimensionless melt production rate	
n	stress exponent	3
p	pressure, Pa	
R	gas constant, $\mathrm{J\,K^{-1}\,mol^{-1}}$	8.314
Ra	thermal Rayleigh number	
ΔS	Change in entropy upon melting, $\mathrm{J\,K^{-1}\,kg^{-1}}$	250
T	mantle temperature, K	
T_m	mantle reference temperature, K	1598

T_s	dry solidus temperature, K	
T_{s0}	dry solidus surface temperature, K	1373
T_{wet}	wet solidus temperature, K	
ΔT	super adiabatic temperature drop, K	1325
$\frac{\partial T_s}{\partial z}$	depth derivative of the solidus, $K \, m^3$	3.4×10^{-3}
$\frac{\partial T_s}{\partial X}$	depletion derivative of the solidus, K	440
$\mathbf{u}$	mantle creep, $m \, s^{-1}$	
u_i	mantle creep (tensor notation), $m \, s^{-1}$	
v_i	melt flow velocity, $m \, s^{-1}$	
V	activation volume, $m^3 \, mol^{-1}$	5×10^{-6}
V_p	seismic compressional wave velocity	
X	concentration of perfectly compatible trace element	
X_r	reference concentration of a perfectly compatible trace element	1.3
α	coefficient of thermal expansion, K^{-1}	3.3×10^{-1}
α_p	finite element Peclet number	
β	coefficient of depletion density reduction	0.04
β_e	stretching factor	
$\dot{\epsilon}$	strain rate, s^{-1}	
γ	coefficient of melt density reduction	0.16
κ	thermal diffusivity, $m^2 \, s^{-1}$	10^{-6}
λ_i	unit vector in the vertical direction	
μ	shear moduli	
η	viscosity, $Pa \, s$	
η_0	reference viscosity at base of model, $Pa \, s$	
ϕ	retained melt (porosity)	
ρ	density, $kg \, m^{-3}$	
ρ_m	mantle reference density, $kg \, m^{-3}$	3340
ρ_l	melt density, $kg \, m^{-3}$	2800
ρ_r	density of mantle at reference residue X_r, $kg \, m^{-3}$	3295
$\Delta\rho$	change in mantle density	
τ	deviatoric stress, Pa	
χ_{H_2O}	viscosity increase factor due to dehydration	$0 - 100$
χ_m	viscosity reduction factor due to interstitial melt	
N97	abbreviation for Niu (1997)	
WM91	abbreviation for Watson and McKenzie (1991)	

To Lidia

Chapter 1

Introduction

During the early sixties there emerged a new theory on the evolution of the oceans and ocean basins. In two papers, Dietz (1961) and Hess (1962) proposed that the continents drift above the mantle as a surface expression of large convection cells within the mantle. Mid-ocean ridges are at the point at which mantle wells upwards and down welling gives subduction zones. Continental drift is a passive process driven by convection within the mantle. The similarity between the Cabot Fault in North America and the Great Glen in Scotland (Wilson, 1962), the increasing age of ocean islands with distance from the mid-ocean ridge (Wilson, 1963) and the post World War II mapping of marine magnetic anomalies (Vine and Mathews, 1963; Vine, 1966), increased the evidence of continental drift. By linking the sea-floor topography and thermal history with solutions to steady state stretching of the lithosphere (McKenzie, 1967), there became little doubt that the ocean basins were expanding. These ideas were brought together first in Morgan (1968) and consolidated in Isacks et al. (1968), forming the new theory of plate tectonics.

Once the concept of sea floor spreading was accepted, the mechanisms of the rifting of a continent to form an ocean basin were elusive and remain so to this day. Early models of rifting looked at simple stretching and thinning of the lithosphere (e.g. McKenzie, 1978; England, 1983). Boundary conditions can be prescribed to stretch the lithosphere. By doing so, the formation of sedimentary basins such as the North Sea can be mathematically described. However, the processes that lead to the formation of oceans are far more complex. The continents need to be put under such stress that they fail, faulting and stretching until the continental lithosphere fails completely. At this point new lithosphere and an ocean is formed.

Continental lithosphere is immensely strong. Continents are formed of mainly silicate rocks and unless there is some weakness within it, by thermal cracking, magma emplacement or something else, then there would be no tectonic plates but a solid lid around the Earth (Kendall et al., 2005; Korenaga, 2007; Solomatov, 1995). Rock can fail in a brittle or ductile manner. As the Earths surface is put under stress it will first deform elastically, but once a critical stress is reached the material will yield and fail. This failure can take two paths: the material fractures along a defined surface (brittle failure) or the material fails by irrecoverable continuous deformation (ductile failure). The upper lithosphere at the surface of the Earth is brittle, asthenospheric mantle however flows over long time scales.

1.1 Deformation and Flow of Solid Material

When a body is put under stress, τ_{ij} in tensor notation, it will deform. The basis for any study of the deformation of the mantle and a geodynamic model of rifting are the equations of equilibrium of mass, momentum and energy. When a small body of rock is in equilibrium, the forces on all sides must be equal and there is no displacement of material. The small body of rock deforms continuously when under a constant stress, it flows, and in this case the kinematic state of the material is described by the rate of change in strain. Strain describes the infinitesimal changes in displacement of material that is subject to stresses. For a medium that is flowing these small displacements occur continuously, therefore the basic kinematic quantity is the velocity, u, of the movement of material. The strain rate tensor, the change in strain with time, relates the small changes in velocity of moving material,

$$\epsilon_{ij} = \frac{1}{2} \left(\frac{\partial u_i}{\partial x_j} + \frac{\partial u_j}{\partial x_i} \right) \tag{1.1}$$

Where i and j are matrix indices: for example $i = 1$ is the x-direction, $i = 2$ is the z direction for a two dimensional system.

A solid is a medium that will not yield until the stress reaches a critical limit, where then it will fail. This describes the Earth's surface. A fluid is a medium that exhibits steady state flow when under constant stress. In the mantle this process is referred to as creep, to help distinguish it from flow of fluids at a lattice level. Such notation has the advantage that it helps descriptively. The Earth's mantle behaves as a fluid only on geological time scales, the flow is extremely slow: the mantle creeps.
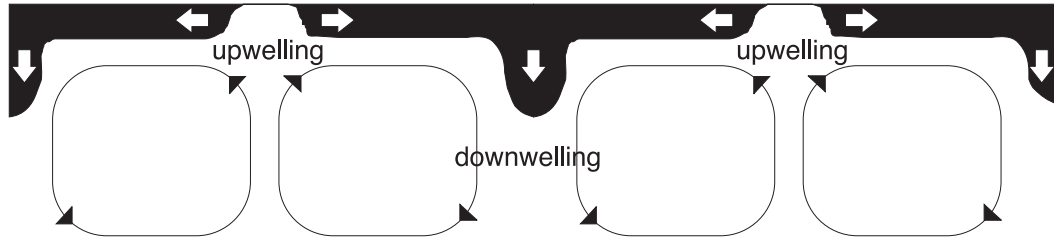
FIGURE 1.1: Plate scale convection

The simplest deformation is of pure shear. Pure shear is defined as having no solid body rotation, that is if a block of material is stretched in one plane it would respond by shortening in the other plane. This can be expressed as a stretching factor,

$$\beta_e = \frac{L}{L_0} \tag{1.2}$$

where L is the present (new) length and L_0 is the initial length of the lithosphere. By defining the stretching factor in this way, the upwelling velocity becomes proportional to spreading rate: Strain rate is is homogeneous throughout the whole plate (England, 1983) and given by,

$$\dot{\epsilon}(t) = \frac{1}{L}\frac{dL}{dt} = \frac{\dot{\epsilon}_0}{\beta_e} \tag{1.3}$$

where $\dot{\epsilon}_0$ is the initial strain rate. The strain rate is then related to the vertical velocity, u_z,

$$u_z(t) = \frac{\dot{\epsilon}_0}{\beta_e}(a - z) \tag{1.4}$$

where a is the thickness of the plate (England, 1983). And so,

$$u_z(t) \propto \frac{dL}{dt} \tag{1.5}$$

By making the two assumptions, that extension is symmetric and and that there is no rotation due to stresses, the vertical velocity of the lithosphere and asthenosphere becomes directly proportional to the spreading rate. There are many processes that will alter this relationship when considering the dynamics of rifting. The most fundamental of these is melting.

1.2 Steady State Extension of the Lithosphere

The Earth is continually losing heat through its surface. The flux of heat, or heat flow, is strongest at the mid-ocean ridges and least in the middle of large continents. The straightforward explanation is that the continents are older, and therefore have lost

more of their heat than the young oceans. That is fine, yet the heat flow peaks along the mid-ocean ridges. Turcotte and Oxburgh (1967) suggested that the measured heat flux was a surface expression of the convecting mantle beneath the lithosphere, see Figure 1.1. The scale of mantle movement was of upwelling at ridge crest to down-welling at subduction zones. The large scale convection model with constant viscosity and a temperature dependent density could produce a steady state heat flux along the ridge axis that was in reasonable agreement with observations (Turcotte and Oxburgh, 1967).

Magnetic anomalies frozen into the rock on the ocean floor suggest that hot basalt (iron- and magnesium-rich igneous rock) crystallises as dykes along the ridge axis. Dykes are small igneous bodies that are intruded into cracks within the crust. The emplacement of these dykes causes increased heat flow and as the sea floor spreads the rocks cool, locking in the magnetic field. In McKenzie (1967) it is suggested that if this were correct, the high heat flow would be as a result of tension in the lithosphere, not a surface expression of the movement of the upper mantle. To test this hypothesis, the lithosphere is represented by a plate of constant thickness (50 km) with constant thermal boundary conditions of 550 °C at the base and the ridge axis. Turcotte and Oxburgh (1967) and McKenzie (1967) both calculate analytical solutions of the steady state heat transport equation,

$$- \mathbf{u} \cdot \nabla T + \kappa \nabla^2 T = 0 \qquad (1.6)$$

in two dimensions, where $\mathbf{u}$ is the velocity of the movement of material and κ is thermal diffusivity. The only difference in the two solutions is the choice of boundary conditions (Parsons and Sclater, 1977). McKenzie (1967) requires a thermal boundary at the base of the stretching plate whilst Turcotte and Oxburgh (1967) has none. Parsons and Sclater (1977) re-assessed these two solutions and found that the plate model more accurately reproduces sea floor topography and heat flux with a plate thickness of 125 ± 10 km and base temperature of 1350 ± 275 °C. These calculations were again revisited by Stein and Stein (1992) where the lithosphere was calculated to be thinner, 95 ± 15 km and the mantle at the base of the lithosphere hotter, 1450 ± 250 °C. The essential feature of these plate models is that the temperature remains constant at the bottom boundary. The difficulty arises in explaining what mechanism maintains the boundary temperature against the cooling of the lithosphere.

A steady state solution to the extension of the lithosphere at mid-ocean ridges will presume infinite stretching, or in other words no change in strain with time. McKenzie (1978) focuses on modelling the evolution of sedimentary basins by using a finite instantaneous stretching factor. This causes thinning of the lithosphere and upwelling of hot

asthenosphere. By solving the heat conduction equation,

$$\dot{T} = \kappa \frac{\partial^2 T}{\partial z^2} \qquad (1.7)$$

and the strain rate (Equation 1.3) for various stretching factors, β_e, it was found that the subsidence is sensitive to the amount of extension only (McKenzie, 1978).

The model of McKenzie (1978) is applied by Le Pichon and Sibuet (1981) to the formation of the Northern Bay of Biscay and Galicia continental margins. Problems arise within such a simple model when parameterising the amount of extension required to stretch the lithosphere. England (1983) attempted to reconcile this by including a temperature dependent ductile strain rate, to characterise the elastic strength of the lithosphere. The heat flow equation becomes,

$$\dot{T} = -u_z \frac{\partial T}{\partial z} + \kappa \frac{\partial^2 T}{\partial z^2} \qquad (1.8)$$

where u_z is the velocity the movement of mantle material in the vertical direction. By including brittle failure within such a model, Sawyer (1985) finds that for all extension rates, lithospheric strength is not a barrier to large amounts of extension and evolution towards sea floor spreading.

1.3 Mantle Dynamics During the Rifting of Continents

In early studies of spreading and crustal thickness (such as Reid and Jackson, 1981), an isoviscous mantle is forced to convect by applying boundary conditions of a fixed velocity. Such kinematic models give rise to passive upwelling, or what is called corner flow. Buoyancy forces may act to perturb the passive corner flow driven by the plates (Mutter et al., 1988; Scott, 1992), and as such create a dynamic model driven by kinematic boundary conditions. Thermal buoyancy arises due to the temperature gradients that exist within the mantle. Therefore the lithosphere can become unstable leading to small-scale convection (Parsons and McKenzie, 1978). It is generally hypothesised that small-scale convection heats the base of the oceanic lithosphere maintaining the thermal boundary (for example Parsons and Sclater, 1977; Fleitout and Yuen, 1984; Buck and Parmentier, 1986; Scott, 1992; Solomatov and Moresi, 2000; Huang and Zhong, 2005). Small-scale convection is used to explain the decrease in subsidence of the ocean floor from that predicted by thermal cooling by heat conduction alone (Parsons and McKenzie, 1978; Buck and Parmentier, 1986). The interaction of these instabilities may maintain the thermal boundary at the base of the lithosphere as suggested by Parsons and Sclater
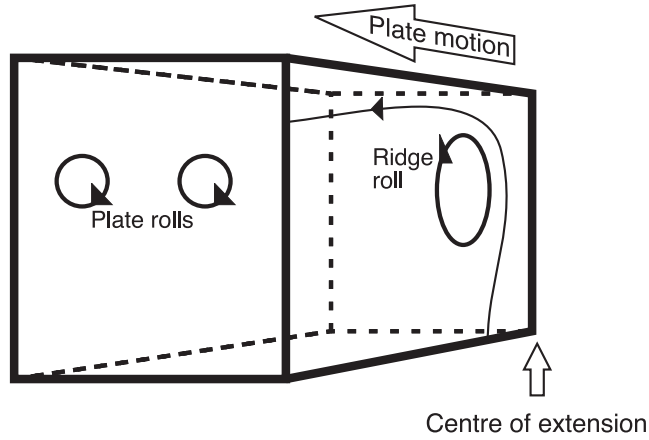
FIGURE 1.2: Diagram showing small-scale convection in the form of 'plate rolls' perpendicular to the plate motion and 'ridge rolls' parallel tot he direction of plate motion.

(1977). It can therefore affect the the global thermal evolution of the Earth (Solomatov and Moresi, 2000).

Small-scale convection is modelled as 'rolls' perpendicular to plate motion (known as 'plate rolls') or parallel to plate motion (known as 'ridge rolls'; see Figure 1.2). Stokes equations of flow governs the circulation of the lithosphere everywhere, which we will present here in tensor notation. Here I also use the summation convention that repeated indices are summed (see Chapter 2 for a full explanation),

$$-\frac{\partial \tau_{ij}}{\partial x_j} + \frac{\partial p}{\partial x_i} = \Delta\rho\lambda_i \tag{1.9}$$

where $\Delta\rho$ is the change in mantle density due to temperature and melting. In the simple case of the change in density during rifting being purely thermal then the combined Stokes equations of flow and the conservation of energy (advection and diffusion equation) can be written as, (Fleitout and Yuen, 1984; Scott, 1992):

$$\frac{\partial u_i}{\partial x_i} = 0 \tag{1.10}$$

$$-\frac{\partial \tau_{ij}}{\partial x_j} + \frac{\partial p}{\partial x_i} = g\rho_m\alpha\left(T - T_m\right)\lambda_i \tag{1.11}$$

$$\frac{\partial T}{\partial t} = -u_i\frac{\partial T}{\partial x_i} + \kappa\frac{\partial^2 T}{\partial x_j^2} \tag{1.12}$$

Where the deviatoric stress tensor τ_{ij} is defined as,

$$\tau_{ij} = 2\eta\dot{\epsilon}_{ij} \tag{1.13}$$

g is the acceleration due to gravity, ρ_m is the mantle density, α is the thermal expansivity, T_m is the potential temperature of the mantle, κ is the thermal diffusivity, η is the mantle viscosity and $\dot{\epsilon}_{ij}$ is the strain rate tensor as defined in Equation 1.1.

Small scale instabilities are expected to line up parallel to plate motion, plate rolls, as a result of the large scale passive flow (Richter and Parsons, 1975; Figure 1.2). The fluid mechanical equations described above were used in dynamic models to model small-scale convection under the oceanic lithosphere (Fleitout and Yuen, 1984; Buck and Parmentier, 1986). Such small-scale convection could explain observed gravity anomalies parallel to plate motion, perpendicular to the mid-ocean ridge (Buck and Parmentier, 1986). Although from three-dimensional modelling of rift evolution, it is found that small-scale convection in the form of plate rolls probably does not give enough melt to match the gravitational anomalies observed at the East Pacific Rise (Haxby and Weissel, 1986; Sparks and Parmentier, 1993).

Scott and Stevenson (1989) and Scott (1992) use equations similar to Equations 1.10, 1.11 and 1.12 to model motions on a plane parallel to extension. In their model, flow is driven by both plate movement (the boundary conditions) and thermal buoyancy. Typical evolution involves development of small-scale convective flow in the low viscosity zone beneath the plate, which is set up within the initial conditions, and the slight cooling of the convection region (Scott, 1992). The convection set up can be described as a ridge roll (see Figure 1.2). These instabilities have a length of 200 km (Scott, 1992). Furthermore, Sparks and Parmentier (1993) find that such ridge rolls, that likely exist within the region of the ridge axis, join up with the perpendicular plate rolls. Again such instabilities can be linked to ridge parallel gravity anomalies, but care has to be taken, as parallel gravity anomalies may also represent variations in magma supply to the mid-ocean ridge (Peirce et al., 2005). Otherwise parallel gravity anomalies can be due to ridge jumps, where the rifting margin shifts laterally (Shah and Buck, 2006).

More recent modelling of small-scale convection suggests the instabilities occur at depths of 85 to 100 km (Solomatov and Moresi, 2000). Observational evidence of small-scale convection is controversial. The interpretation of the gravity anomalies measured over the East Pacific Rise is still debated, and there is no concrete proof for the existence of small-scale convection (Winterer and Sandwell, 1987; Gans et al., 2003).

1.4 Melting

In early studies of sea floor spreading (such as Reid and Jackson, 1981), an isoviscous mantle subject to purely kinematic boundaries is allowed to convect. When mantle rises,
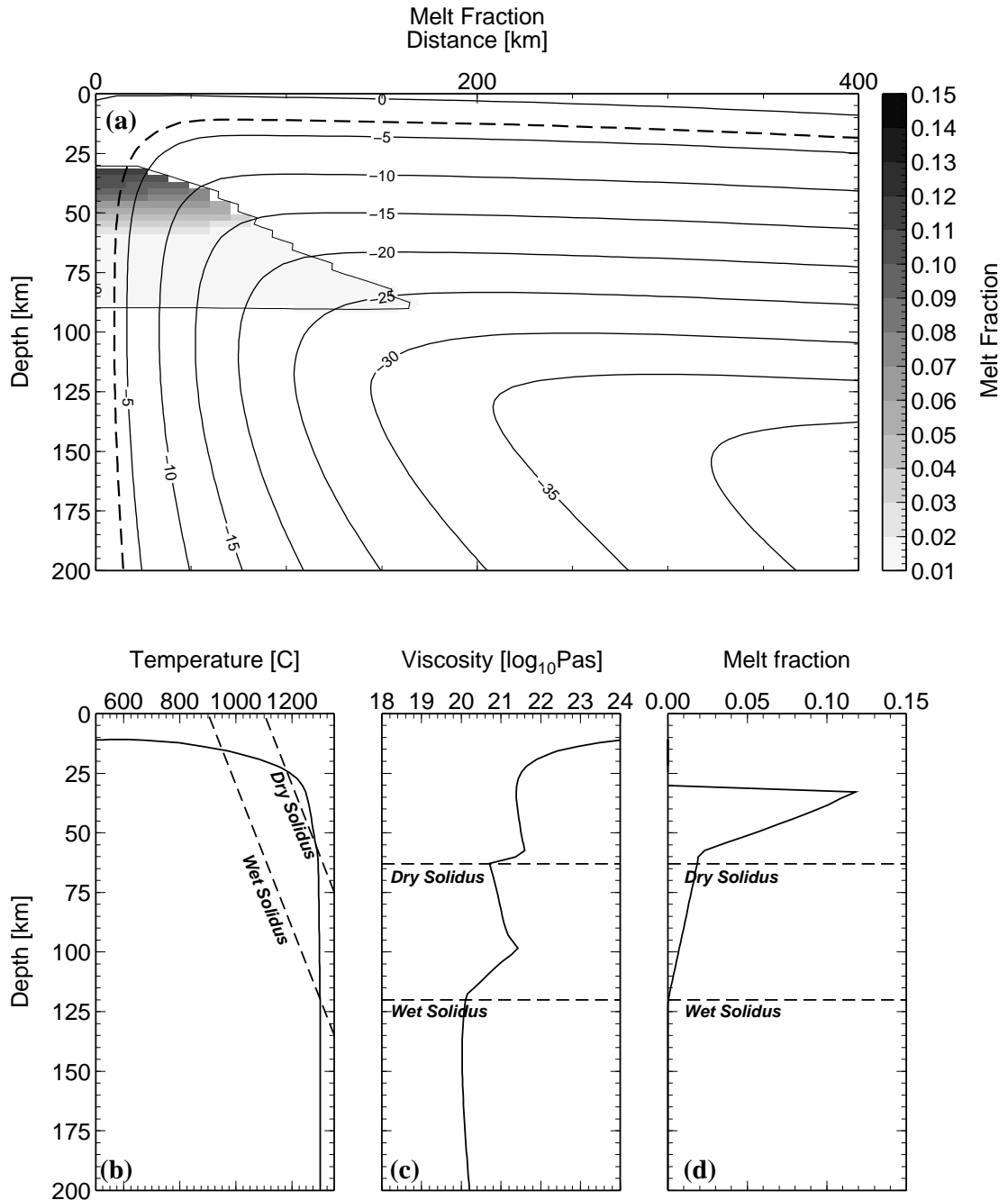
FIGURE 1.3: (a) Corner flow model that includes buoyancy due to retained melt, melt depletion and temperature. Plotted are melt fraction and contours of the value of the streamline function (mantle flow). (b) The temperature of the dashed streamline plotted in (a) is shown along with the solidus for wet and dry mantle, (c) displays viscosity and (d) melt depletion. These plots show the competing effects of pressure, temperature, dehydration and melt upon the dynamics and rheology of a model.

it melts as it decompresses, forming a region of melt beneath the centre of extension (see Figure 1.3). Melting occurs on the smallest scales in two steps (see McKenzie, 1984): The rock partially melts by the change in pressure and temperature. Once melt has formed it separates from the remaining solid matrix and percolates through the solid matrix. Darcy's law governs percolation, the flow of melt through the solid matrix,

$$\phi v_i = -\frac{k_\phi}{\eta} \frac{\partial}{\partial x_i} \left(p + \rho_l g \lambda_i \right) \tag{1.14}$$

where ϕ is melt porosity, v_i is melt velocity in tensor notation, k_ϕ is permeability, p is pressure, ρ_l is melt density. Finally g is acceleration due to gravity and λ_i is a unit vector in the vertical. In order to include melting within a model of mantle flow, the solidus and energy balance need to be defined in order to determine the melt behaviour and rates of melting.

The mantle is a multiphase multicomponent solid, and so there is no simple equation of state that describes the position of the solidus and liquidus for pressure and temperature. Melting during rifting of the lithosphere is due to decompression, which can be influenced by the presence of thermal anomalies. Early studies use an empirically derived solidus curve in order to calculate the fraction or degree of melt, F, generated during decompression (for example McKenzie and Bickle, 1988). Little has in fact changed within models of melting. This is despite the recent advances in thermodynamic modelling of the melting of rock. There exist a few numerical algorithms that can compute the phases for multicomponent minerals such as *perple_X*, Connolly (2005) or *Melts* Ghiorso and Sack (1995). Yet, relating the position of the mineral on the phase diagram to the degree of melting undergone is not a straight forward process. A simple relationship to gain the fraction of melt generated from the solidus is (from Sparks and Parmentier, 1993),

$$F = \frac{T - T_{solidus}}{L/c_p} \tag{1.15}$$

where L is the latent heat of melting and c_p is the specific heat at constant pressure. The solidus, $T_{solidus}$ is given in this case by a simple linear relationship with depth,

$$T_{solidus} = 1100(^{\circ}\text{C}) + 3.25z(\text{km}) \tag{1.16}$$

Melt production is then the material derivative of the melt fraction,

$$\dot{m} = \frac{DF}{Dx_i} \tag{1.17}$$

In Figure 1.3 there is not only one solidus, a wet and dry solidus are defined, as the

mantle dehydrates as it melts (Hirth and Kohlstedt, 1996). In back arc basins it has been widely recognised that water that gets trapped within the subducted slabs can alter the melting characteristics greatly (e.g. Grove et al., 2006). Normal mantle is very slightly damp. The partitioning of water between mantle peridotite (MORB source) and melt is estimated to be (Hirschmann, 2006; Hirth and Kohlstedt, 1996),

$$D_{H_2O}^{peridotite/melt} \sim 0.01 \tag{1.18}$$

from melting experiments and H_2O/Ce ratios. This relates to there being between 50 and 300 ppm water in the mantle peridotite, depending on the choice of melting model (e.g. Hirth and Kohlstedt, 1996; Robinson et al., 2001; Dixon et al., 2002). The amount of water dissolved in the mantle is however dependant on the source, with MORB derived from a plume-associated source having H_2O concentrations of between 300 and 1000 ppm (Dixon et al., 2002).

Damp melting is far less productive, about 1 % per 20 km based on mass balance calculations of the dehydration of olivine, when compared to dry melting (Hirth and Kohlstedt, 1996, Figure 1.3d). The wet solidus is between 5 and 55 km beneath the dry solidus (Hirth and Kohlstedt, 1996; Aubaud et al., 2004; Asimow and Longhi, 2004). In Figure 1.3 (c) and (d) I have taken the deepest estimate of Asimow and Longhi (2004). Following Braun et al. (2000), the wet solidus is approximately 200 °C cooler than the dry solidus. Despite the difficulties with estimating the exact changes to melt productivity and the solidus, it is becoming increasingly clear that wet melting occurs given the effects of the dehydration of the mantle on the rheology of the mantle (for example Ito et al., 1999).

For calculating the quantities of melt due to isentropic melting of a complex multicomponent rock, a quantity used is the 'productivity' of melting: the amount of melt production per decrease in pressure (Asimow et al., 1997; Hirschmann et al., 1994). A common approach to estimating melt production is to assume that melt fraction increases linearly as pressure decreases (such as Equation 1.15). This is what is assumed within many physical models of melt production, such as Reid and Jackson (1981); Scott and Stevenson (1989) and Sparks and Parmentier (1993). The melt production rate is then just the material derivative of the degree of melting.

There is evidence however, that melt generation is more complex. Asimow et al. (1997) explains that there is no thermodynamic basis for assuming a constant rate of melt production. Peterological models of melting such as McKenzie and Bickle (1988) or Langmuir et al. (1992) suggest rather that melt productivity is more complex. Melt

production might be enhanced close to the solidus of peridotite, based on melting experiments (McKenzie and Bickle, 1988). Melt production may also be enhanced at high pressures, as the solidus is closer to the liquidus (Langmuir et al., 1992). Asimow et al. (1997) however suggest increasing melt production as melting proceeds. This is from thermodynamic calculations of the melting of one- and two-component systems.

Given the complexities and debate over melt productivity, as mentioned, in this thesis the solidus relationship is as Scott (1992), where productivity increases linearly with decreasing pressure and also increases as melting progresses (see Section 2.2.2). The melt production calculations are similar to that of Phipps Morgan (2001), and have been previously applied to melt production at rifted margins in Ito et al. (1996) and Nielsen and Hopper (2004).

1.4.1 Melt Buoyancy

Decompression melting of rock within the mantle as it rises due to upwelling has two effects on the density of the whole rock. First, if some or all of the material remains within the source rock, the density difference between the solid and liquid creates a buoyancy force (Scott, 1992). Second, the density of the solid residue from which the melt is extracted changes with progressive melting (Scott, 1992). These two processes are commonly referred to as 'melt retention' and 'melt depletion' (Ito et al., 1996). Melting in slow upwelling mantle, in the absence of melt or fluid flow can be approximated as a reversible adiabatic process, and hence as isentropic (McKenzie, 1984). If melt/fluid migration or viscous deformation occur the process is no longer locally adiabatic or isentropic, however it can be idealised into incremental isentropic steps (Asimow et al., 1997).

Melting within dynamic models has been treated with many differing views as to the relative importance of melt retention and depletion. Convection models, such as Parmentier and Phipps Morgan (1990), play down the importance of melt retention given the evidence from uranium isotope disequilibria that melt is rapidly extracted from the partially molten rock (McKenzie, 1985; Kelemen et al., 1997a). This allows melt porosity to reduce without significantly affecting the melt fraction. However Scott (1992) suggests that this is in error as the nature of the sources of the two buoyancy are quite different. The suggestion is that lateral gradients drive flow within a gravitational field. Melt production by adiabatic upwelling causes little horizontal change in the extent of melting, reducing the impact of melt depletion buoyancy (Scott, 1992). However, the presence of small amounts of melt within the mantle gives rise to a buoyancy that drives more rapid upwelling, which in turn generates more buoyancy (Scott, 1992).

Therefore Scott (1992) suggests that an active flow of any vigour associated with melting must be driven by melt retention buoyancy and modified by melt depletion buoyancy. Due to these remarks, subsequent models of mantle convection such as Ito et al. (1999), Ito et al. (1999), Boutilier and Keen (1999) and Nielsen and Hopper (2004) use very similar approaches to calculating melt buoyancy as Scott (1992).

To implement the buoyancy forces due to melting, $\Delta\rho$ within Equation 1.9 becomes a function of melt fraction and porosity as well as temperature (see Chapter 2, Section 2.1.2). The advection-diffusion term (Equation 1.12) is modified to take account of the advection of melt (from Scott, 1992),

$$\frac{\partial T}{\partial t} = -u_i\frac{\partial T}{\partial x_i} + \kappa\frac{\partial^2 T}{\partial x_j^2} - \frac{T_m\Delta S}{c_p}\dot{m} \qquad (1.19)$$

where ΔS is the change in entropy, T_m is a mantle reference temperature, c_p is the heat capacity at constant pressure and $\dot{m}$ is the melt production rate (see Chapter 2, Section 2.2). Melt migration and depletion are treated with similar advection-compaction and advection equations (Scott, 1992; Ito et al., 1996; see Chapter 2, Section 2.2.1).

The addition of a melt buoyancy term within the equations of flow modifies the convection set up within the geodynamic models of extension and rifting of the continental lithosphere. When included into models of small-scale convection it suppresses the formation of ridge rolls and can lead to unstable time-dependent (or episodic) behaviour (Scott, 1992; Sparks and Parmentier, 1993).

1.5 Rheology

1.5.1 Newtonian or Non-Newtonian

The equation describing the relationship between stresses and strain rates is known as the rheological law for the fluid (Turcotte and Schubert, 2002). The simplest relationship is of a 'Newtonian' or linear fluid, in which the rate of strain $\dot{\epsilon}$ is directly proportional to the applied stress τ (Fleitout and Yuen, 1984):

$$\tau = 2\eta\dot{\epsilon} \qquad (1.20)$$

The constant of proportionality, η, is the viscosity. Early models of mantle convection such as Reid and Jackson (1981) use simple isoviscous mantle viscosity. This is an over-simplification as the fluid behaviour of the earths mantle is governed by, at the least, changes in temperature and pressure. A common choice for the relationship between

temperature, T, pressure, p, and viscosity, η, comes from Weertman and Weertman (1975),

$$\eta = A\,exp\left(\frac{E + pV}{RT}\right) \tag{1.21}$$

where E is the activation energy and V the activation volume for a particular mechanism of deformation, A is a constant varied to adjust the average viscosity and R is the universal gas constant. The activation energy and volume are determined experimentally.

The Earth's mantle is however made up of polycrystalline materials that do not behave in a simple linear fashion under deformation. At low stress levels and/or small grain sizes deformation is by diffusive mass transport between the grain boundaries (diffusion creep) and the strain rate increases linearly with stress (Karato and Wu, 1993). At high stresses and/or large grain sizes deformation occurs by movement of dislocations within the lattice or grains (dislocation creep; Karato and Wu, 1993). Such fluid motion is referred to as 'non-Newtonian' as the relationship between stress and strain becomes non-linear (Turcotte and Schubert, 2002). As temperature and pressure change the mechanism that gives the higher strain rate becomes the dominant creep, and so the type of deformation may also change with depth (Karato and Wu, 1993). Seismic anisotropy suggests that the upper mantle flows by dislocation creep (Karato and Jung, 1998; Karato and Wu, 1993), and recent convection models tend to use a non-Newtonian rheology (for example, Boutilier and Keen, 1999; Solomatov and Moresi, 2000; Nielsen and Hopper, 2004). This rheology is parameterised by Boutilier and Keen (1999) as follows,

$$\eta = A\dot{\epsilon}^{\left(\frac{1-n}{n}\right)}exp\left(\frac{E + PV}{RT}\right) \tag{1.22}$$

where $n = 1$ for the Newtonian case and $n \approx 3$ for typical upper mantle rocks (Solomatov and Moresi, 1996; Boutilier and Keen, 1999; Solomatov and Moresi, 2000).

1.5.2 Dehydration Strengthening

Early studies into the deformation of wet and dry rocks such as Chopra and Paterson (1984) found that their strength is significantly reduced by water. Yet the influence of water on mantle dynamics is not well known. As discussed within Section 1.4, evidence from seismic anisotropy and dynamics suggest that the mantle is wet (Hirth and Kohlstedt, 1996; Karato and Jung, 1998; Solomatov and Moresi, 2000). As the source rock rises it undergoes decompression melting and crosses from the wet to dry solidus, as shown in Figure 1.3a. From the initiation of melting at a depth of $\sim 115\,\text{km}$ until dehydration, Hirth and Kohlstedt (1996) calculate that only 1-2 % of melt is produced.

That transition from wet to dry mantle has large implications for the viscosity of the rock as mantle volatiles such as water partition into the early melt.

Dehydration causes the activation energy and volume to increase (see Equation 1.22; Solomatov and Moresi, 2000; Mei and Kohlstedt, 2000). Such a change is manifest as a sharp increase in viscosity by a factor of at least 100 at a depth of around 70 km as shown in Figure 1.3b (Hirth and Kohlstedt, 1996; Solomatov and Moresi, 2000). This corresponds with dehydration occurring at around 60-80 km, the 'Gutenberg discontinuity' (Karato and Jung, 1998; Solomatov and Moresi, 2000; Rychert et al., 2005).

This rapid increase in viscosity with depth when dehydration occurs has been recently added to convection models such as those of Ito et al. (1999) and Nielsen and Hopper (2004). There is also a small decrease in mantle viscosity due to the presence of melt; this decrease is an order of magnitude smaller than the strengthening due to dehydration (Kelemen et al., 1997a) and so has been ignored within most dynamic models. However for completeness it has been included within this model of continental breakup. Within Chapter 2, Section 2.1.3, I will outline how dehydration strengthening and melt weakening are included within the geodynamic model.

1.6   Composition of the Mantle and Melt

Up until now the mantle composition has not been treated, other than recognising that it becomes depleted as melting continues and this effects the mantle rheology and buoyancy. A major part of this thesis is concerned with modelling the chemical composition of melt generated during rifting. This melt can have a different composition depending on the initial composition of material entering the melting region, and the conditions under which melting occurs. There are various models that try to quantify the composition from polybaric melting (melting at various pressures) of the mantle, such as Klein and Langmuir (1987); McKenzie and Bickle (1988); McKenzie and O'Nions (1991); Niu and Batiza (1991); Watson and McKenzie (1991); Langmuir et al. (1992); Niu (1997). These use varying degrees of thermodynamic arguments and reliance on statistical correlation techniques, and there is a degree of correlation between all models (McKenzie and O'Nions, 1991; Langmuir et al., 1992).

This thesis will focus on two approaches taken to estimate the melt composition. Firstly, the inverse methods to estimate the major primary melt composition of McKenzie and Bickle (1988); Watson and McKenzie (1991) and McKenzie and O'Nions (1991). These methods are empirical, and rely on performing a statistical fit to a wide data set from melting experiments. The second method is that of Niu and Batiza (1991) and Niu

(1997), where the partitioning of the chemistry between the solid and melt is calculated starting from the initial source mantle composition. These methods lead to three parameterisation that I have applied within a geodynamic model of the extension and rifting of continents. Two are for calculating the major element composition of the primary melts: Watson and McKenzie (1991) – WM91, and Niu (1997) – N97. The methods and implementation of these parameterisations are dealt with in full within Chapter 2, Sections 2.3.1.1, 2.3.1.2.

Modelling of the composition of the melt generated during rifting is one of the last remaining puzzles of rifted margins. For example while measurements of igneous crustal thickness suggest that the Southeast Greenland margin rifted above a hot thermal anomaly (Nielsen and Hopper, 2002). Geochemical evidence suggests a much reduced thermal anomaly and increased active upwelling (for example Fram and Lesher, 1993). By forming a geodynamic model of rifting that can predict the composition of the melt, such arguments of the importance of passive extension above a thermal anomaly versus some how enhanced active upwelling can be explored. The model presented in the following chapters will hopefully begin to resolve the importance of mantle rheology and temperature on the style of rifting.

1.7 Rift Asymmetry and Rift Migration

The lithosphere and crust can be asymmetrically thick on either side of volcanic, non-volcanic, fast or slow rifted margins (for example, Hopper et al., 2003; Katz et al., 2004; Searle and Bralee, 2007; Shillington et al., 2006). Asymmetry of the oceanic crust is dependant on the characteristics of the axial magma chambers, whilst lithosphere asymmetry is more likely due to the shape and focussing of the melt region. Asymmetric melt chambers have been imaged under the Valu Fa Ridge back arc extensional basin, however at the East Pacific Rise and Reykjanes Ridge, symmetric melt chambers appear to exist (Dunn and Forsyth, 2003; Sinha et al., 1998; Sinha and Evans, 2004). However both these ridges have asymmetric lithospheric thickness (Hopper et al., 2003; Toomey et al., 2002). This asymmetry is possibly from asymmetry of the mantle-crust boundary, the Moho, due to asymmetry in the melt region (Corti and Manetti, 2006; Dunn and Forsyth, 2003). Such asymmetry is likely driven or partly driven by asymmetric spreading at the rifted margin or ridge as shown in Figure 1.4, (Toomey et al., 2002; Hopper et al., 2003).

Asymmetric melt regions have been generated to match the current melt generation and ridge segmentation at the East Pacific Rise (for example see Figure 1.4; Conder
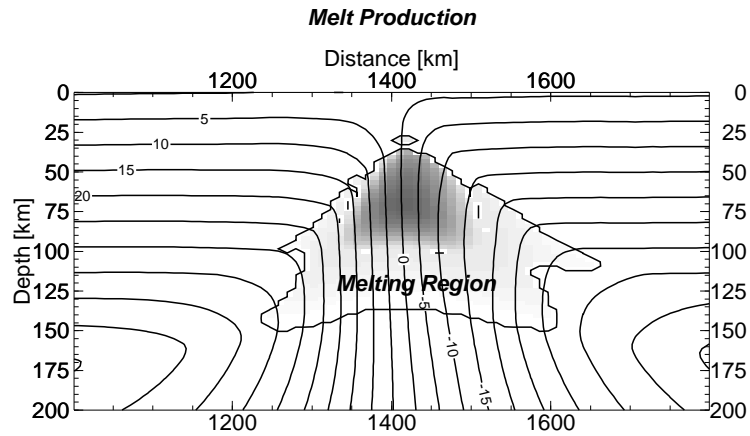
FIGURE 1.4: Diagram of the melt region beneath the mid ocean ridge system. Included are contours of the streamline function (flow of the solid mantle) that drives the upwelling of material beneath the divergent plates.

et al., 2002; Toomey et al., 2002; Carbotte et al., 2004; Katz et al., 2004). These models generate asymmetry within the melting region by assuming that the rifting margin is migrating above the mantle. To include this within a geodynamic model three boundary conditions are applied: spreading is driven along the top boundary by divergent velocity conditions, and rift migration is driven by a third boundary condition on the base of the model at 670 km depth. Rift migration is suggested as a possible reason for the asymmetric volumes of melt emplaced at the Southeast Greenland margin relative to the conjugate Hatton Bank (Hopper et al., 2003).

However to match the observed asymmetry of the observed melt region at the East Pacific Rise from shear wave velocity inversions requires more than just ridge migration. Models of the East Pacific Rise require an inflow of warm mantle from the Pacific superswell region (Conder et al., 2002; Conder, 2007; Toomey et al., 2002). This suggests that when considering rifted margins, the regional and local setting must be considered. In the North Atlantic it is likely that the ocean basin formed above an exhaustible thermal anomaly (Holbrook et al., 2001; Tegner et al., 1998). This warm material drained along the sublithospheric topography. There is also evidence of extension off both sides of the North Atlantic prior to the opening of the main rift. There was extension off Southeast Greenland prior to breakup (Larsen et al., 1998) and off the west coast of the UK, there are a series of extensional basins that end with the Hatton-Rockall Basin that formed

at about 20 Myr prior to breakup (Edwards, 2002). In Chapter 5 I will explore the consequences of such extension on rifting on the symmetry of melt production.

Density changes due to a asymmetric melt region have been matched to the subsidence at the East Pacific Rise, which gives weight to asymmetric lithospheres being the consequence of an asymmetric melt region. Modelling of melt migration at the East Pacific Rise suggests a convergent flow of melt towards the ridge axis (Spiegelman et al., 2001). Conversely Dunn and Forsyth (2003) require melt to percolate upwards from the asymmetric melting region to give the asymmetric lithosphere. Evidence from dunite channels in ophiolites suggest that the most likely mechanism of melt transport is of a network of high permeability channels (Braun and Kelemen, 2002). Mid-ocean ridge crust is formed within 10 km of the ridge axis, and melt regions can extend for hundreds of kilometres from the ridge axis (Forsyth et al., 1998). Therefore it is reasonable to suggest that melt is focused in some way towards the ridge axis rather than percolating upwards from the melt region. In remains an open question to what extent asymmetric lithospheric thickness can be a consequence of asymmetric melting regions.

1.8 Melt Emplacement

Once the melt has travelled from the melt region to the magma chambers it then will crystallise to form the crust and lithosphere (see Figure 1.5). Oceanic crust is typically divided into three layers: The top seismic layer 1 is formed mainly of sediments that lie on-top of the igneous derived crust. Beneath the sediments is layer 2, which is formed extrusive pillow basalts and intrusive dykes. Layer 3 is associated with continuous gabbro. It is within layers 2 and 3 that the oceanic crust is formed. At fast spreading ridges, such as the East Pacific Rise, a clear axial melt lens is imaged beneath the seismic layer 2 (Detrick et al., 1987). At slower spreading centres axial melt chambers are not imaged, and are therefore thought to be episodic in nature. As with melt migration within the mantle, questions still remain as to how the lower crust forms.

There exist two models for the formation of the lower crust: Melt might accumulate beneath the axial melt lens, and only crystallise near the top of the magma chamber. From here the resulting gabbros will spread outwards and downwards with the continuing rift. Such a model is referred to as 'gabbro glacier' (for example Henstock et al., 1993). The other possibility is that melt exists within the lower crust as thin sills (for example Kelemen et al., 1997b), and melt crystallises out at depth. These two models differ in the arguments of at what depth the melt crystallises. It looks likely that in fact the lower structure of the mid-ocean ridge is a combination of both models, where the crust forms

Gabbro Glacier Model

Pillow basalts

Sheeted dikes

Axial melt lens

Gabbros and Cumulates

Melt lense at the
base of the crust

Peridotites upper mantle

Hybrid Model

Pooled Melt
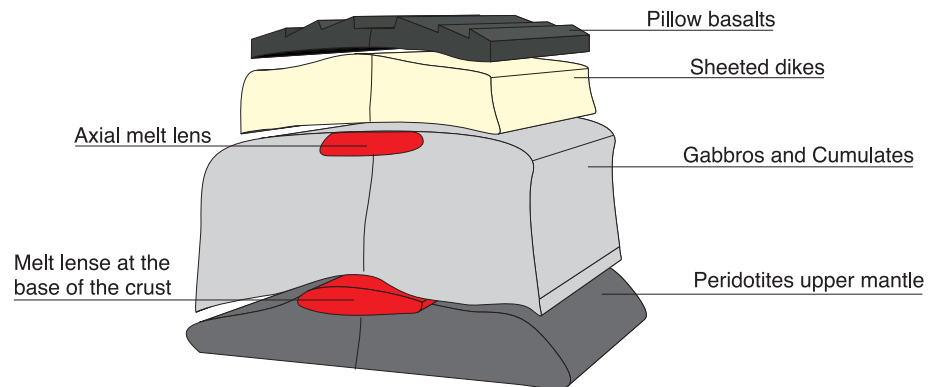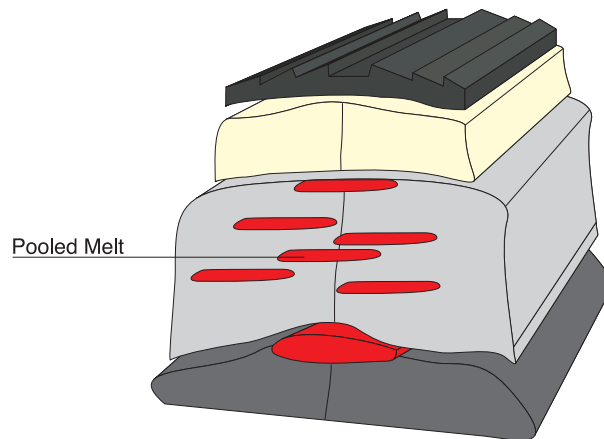
FIGURE 1.5: Diagram of the magma chambers at the mid-ocean ridge, after Sinha and Evans (2004) and (Maclennan et al., 2005). The top diagram shows the *gabbro glacier model*, where melt pools at the base of the crust and then is fed directly a shallow axial melt lens. The crust below this lens is formed by downward advection of cumulates formed in the axial melt lens (Henstock et al., 1993). Below is the *hybrid model*, where the lower crust is formed in part by downward advection from the axial melt lens. The rest is from other small pools of melt within the lower crsut (Maclennan et al., 2005).

FIGURE 1.6: Seismic velocity profile of the Southeast Greenland margin, from Hopper et al. (2003). The region of high seismic velocities, between 6.9 and 7.4 km s^{-1} are interpreted as being igneous rock emplaced during breakup of the North Atlantic (Hopper et al., 2003).

both gabbro glaciers and from sills within the lower crust (Maclennan et al., 2004, 2005). Unfortunately these models all refer to the centre of extension of sea-floor spreading, rather than the processes during rifting.

Recent investigations of the breakup of the East Africa Rift valley have imaged melt beneath the rift valley, and point to the importance of melt induced weaknesses that aid the breakup of continents (Kendall et al., 2005). There is evidence of cooled mafic intrusions and partial melt beneath the centre of extension (Daly et al., 2008). There is also evidence for the magmatic addition to the lower crust, or 'underplate' (Mackenzie et al., 2005). Underplate is a feature that is commonly linked to volcanic active rifted margins (Kelemen and Holbrook, 1995), and is thought to be emplaced during and soon after breakup (White et al., 1987). Typical seismic velocities of underplate are between 7 and 7.6 km s^{-1} (see Figure 1.6; Kelemen and Holbrook, 1995; Holbrook et al., 2001; White et al., 1992). Such high velocities are likely due to the high concentration of magnesium oxides within the primary melt (Kelemen and Holbrook, 1995; Behn and Kelemen, 2003; Sobolev and Babeyko, 1994).

1.9   Convection Models

It can be seen from Section 1.4.1 and 1.5 that there are a range of parameters to be taken into consideration when studying upper mantle convection. Many numerical models have been written to study mantle convection. Before describing my model in detail in the following chapter, I will cover the basic considerations taken by four models of rifted margin evolution. The models are: Scott (1992); Boutilier and Keen (1999); Ito et al. (1999); and Nielsen and Hopper (2004). The dynamic model of rift evolution introduced in the following chapter uses certain aspects of each of these models. The models of Scott (1992), Boutilier and Keen (1999) and Nielsen and Hopper (2004) are concerned with modelling small-scale convection beneath mid ocean ridges and assessing the importance of small-scale convection over buoyant driven upwelling. Ito et al. (1999) look at dehydration, melting and dynamics at a ridge centred hot spot, where there is plume driven upwelling.

1.9.1   Scott, 1992

This model uses similar fluid mechanical equations, as outlined in Equations 1.10, 1.11 and 1.19, to model a temperature- and pressure-dependent rheology (see Equation 1.20) that is subject to buoyancy from temperature and compositional changes. The forms of mantle flow found beneath the ridges is summarised as follows (Scott, 1992): (1) Large-scale passive flow, which is driven by the separation of the plates by an imposed velocity boundary condition at the surface. This flow is a corner flow modified by the temperature- and pressure-dependent viscosity. (2) Small-scale thermal convection at the base of the young lithosphere. The length scale of such flow is around 200 km. (3) Melt-driven circulation in the region of melting beneath the ridge axis. The length scale of this flow is the depth to the onset of melting, 50 km, which is at odds with more recent estimates (see Section 1.5.2). The steady state mid-ocean ridge crustal thickness predicted by this model are in reasonable agreement with the data in White et al. (1992) and Reid and Jackson (1981), however there are no predictions of the volume of melt generated as rifting progresses.

1.9.2   Boutilier and Keen, 1999

Here mantle convection is studied with non-Newtonian viscosity (Equation 1.22). Initial studies are carried out where there is no dehydration strengthening. With initial conditions of some pre-thinning of the lithosphere at the planned ridge axis, it is found that

under the right density and viscosity conditions, significant small-scale convection can be generated, and the models can provide thick crust at initiation of sea floor spreading as expected at volcanic margins. They suggest that small-scale convection, rather than temperature anomalies, may be able to explain the formation of volcanic margins (Mutter et al., 1988). Boutilier and Keen (1999) find that whilst they can generate high amounts of volcanism, there are excessive variations in thickness of oceanic crust that are unacceptable. To dampen these variations in crustal thickness, dehydration strengthening is introduced by setting the model space such that for depths shallower than 80 km the viscosity is increased by 140. This allows for volcanic margins to be simulated, however dealing with dehydration strengthening in this way is inconsistant and is does not allow for the feedback of melting on the dynamics to be included (Nielsen and Hopper, 2002).

1.9.3 Ito, 1999

Ito et al. (1999) models dehydration in a self consistant manner by adding the dehydration pre-exponent into the rheology law,

$$\eta = \chi_{H_2O} A \, exp \left(\frac{E + PV}{RT} \right) \tag{1.23}$$

where χ_{H_2O} takes the form of a linear increase from 1 to 10 as melting progresses until 2 % melt is generated. Then χ_{H_2O} is equal to 100 to simulate the minimum step increase observed when mantle rocks dehydrate (Hirth and Kohlstedt, 1996). A is set from a reference mantle temperature state.

By applying this rheology to a model of plume dynamics at the Iceland centred hotspot, the dehydration prevents buoyancy from contributing to plume upwelling (Ito et al., 1999). The result is that upwelling in the primary melting zone is driven only by the spreading plates. The along-axis crustal thickness, bathymetric variations and gravity variations predicted by the model are shown to be consistant with observations (Ito et al., 1999). Ito builds on this model further successfully predicting the V-shaped ridges of the Reykjanes Ridge, by varying the volume flux of upwelling plume material (Ito, 2001). The essential feature of these two models (Ito et al., 1999 and Ito, 2001) is the viscosity increase by around two orders of magnitude due to water extraction (Ito, 2001).

1.9.4   Nielsen and Hopper, 2004

The model of Nielsen and Hopper (2004) attempts to utilise the successful implementation of dehydration strengthening by Ito et al. (1999), with the inclusion of melt weakening to, improve on the model of small-scale convection by Boutilier and Keen (1999). The rheological law becomes,

$$\eta = \chi_{H_2O}\chi_m A\dot{\epsilon}^{\left(\frac{1-n}{n}\right)} exp\left(\frac{E + PV}{RT}\right) \tag{1.24}$$

where χ_{H_2O} is the dehydration strengthening factor as in Ito et al. (1999), $\chi_m = e^{-45\phi}$ is the melt weakening term (see Section 2.1.3) and $n = 3$. It is found that melt weakening has a negligible effect when compared to dehydration strengthening as the melt porosity is ~ 0.01, giving a melt retention reduction of a factor of 2, while dehydration strengthening is an increase of 100. It was found that dehydration strengthening acts to dampen upwelling to such an extent that any excess magnetism is immediately subdued (Nielsen and Hopper, 2004). However by adding a sub-lithospheric hot layer, the model does predict the temporal evolution of igneous crustal thickness observed in the Southeast Greenland volcanic rifted margin (Nielsen and Hopper, 2004). Nielsen and Hopper (2004) concludes that small-scale convection is unlikely to lead to excessive breakup magnetism. It is more likely that an anomalous layer assists upwelling during the formation of some rifted margins (Nielsen and Hopper, 2002). Such a layer must be 100 to 200 °C hotter or more fertile, yet sufficiently thin that it is quickly exhausted (Nielsen and Hopper, 2004, 2002). The effect is to deepen the mantle solidus and enhance short-lived small-scale convection (Nielsen and Hopper, 2004, 2002).

1.10   Summary

Modelling of rifting has come along way from the initial models of Turcotte and Oxburgh (1967) and McKenzie (1967). Both were looking at explaining the same anomaly from what appeared to be two different methods. Yet, both were solving the same physical equations of heat advection and diffusion. The significant difference between the two models were the boundary conditions that defined the flow. For McKenzie (1967) there was a thermal boundary that marked the base of the lithosphere, and he only concerned himself with solutions to heat advection and diffusion above that layer. Turcotte and Oxburgh (1967) however declared no thermal boundary and allowed large scale convection to interact right up to the sea-floor. In the end it was found that defining a

lithosphere made more physical and mechanical sense, and it was shown that such a lithosphere could have the strength to stretch and thin (Sawyer, 1985).

Kinematic models found that by instantaneously stretching the lithosphere by a factor greater than 2, the asthenosphere would up-well and the lithosphere would thin (White and McKenzie, 1989). By slowing the rate of spreading kinematic models could predict the crustal thickness of non-volcanic margins (White et al., 2001). Furthermore, by using the decompression melting predicted in McKenzie and Bickle (1988), the simple extension model could show that there is no magmatism for slow spreading rates. Extension models are all based on one founding assumption, that there is a thermal boundary at the base of the lithosphere.

Modern day models of convection within the lithosphere still agree on the basic equations of fluid flow. They differ once more in the choice of boundary conditions, and further more in choice of rheology. As our understanding of how the mantle deforms under pressure, the choice of rheology becomes increasingly important to model convection consistantly. A great problem is that making measurements beneath the Earth is very hard. Models are used to test hypothesis of what mantle and lithosphere factors are important. By the inclusion of dehydration pre-multipliers Ito et al. (1999) managed to predict crustal thickness and bathymetry at the Iceland centred hot-spot.

In the following Chapters I will build upon these models taking the application of geodynamic models of rifting a step further. The crust is clearly formed of crystallised rocks. Yet these rocks began as a primary melt contained within the melting region. The chemical composition of the melt is effected by the pressure and temperature during rifting. Like the igneous crustal thickness, the composition of the melt generated at rifted margins varies for different rifting styles. By combining calculations of the composition and volumes of melt generated, I hope to gain a greater insight into what fundamentally controls the production of melt during and after the extension of continents.

Chapter 2

Methods

2.1 Stokes Equations of Creeping Flow

2.1.1 Conservation of Mass

In this thesis, I model the creep of the mantle in response to a surface boundary condition that simulates the rifting of a continent to form new oceanic lithosphere. Stokes equations of flow and the conservation of energy were introduced earlier. A generic velocity u was used to denote the creeping flow of mantle material. That material however melts as it decompresses. Therefore there is the creep or flow of two phases: solid, $\mathbf{u}$ and melt, $\mathbf{v}$. One of the fundamental approximations that this modelling study relies upon is the Boussinesq approximation: that density variations are sufficiently small that they only affect the gravitational force term. Secondly, for the conservation of mass, we can neglect the effects of density changes from mass transfer due to melting as these are small (Cordery and Phipps Morgan, 1993).

Conservation of mass and the other differential equations within this chapter will be expressed in tensor notation using the following summation convention: therefore the divergence of the mantle flow (conservation of mass) is expanded as,

$$\nabla \cdot \mathbf{u} = \frac{\partial u_1}{\partial x_1} + \frac{\partial u_2}{\partial x_2} \tag{2.1}$$

where $\mathbf{u}$ is the mantle flow vector, u_1 and x_1 are the mantle flow and displacement in the horizontal x-direction and u_2 and x_2 are the flow and displacement in the vertical

z-direction. Equation 2.1 can be rewritten as,

$$\nabla \cdot \mathbf{u} = \sum_{i=1}^{2} \frac{\partial u_i}{\partial x_i} \tag{2.2}$$

and then by leaving out the summation sign, $\sum$, with the understanding that repeated indices are summed, the conservation of mass, momentum and energy can be written as,

$$\frac{\partial u_i}{\partial x_i} = 0 \tag{2.3}$$

2.1.2 Conservation of Momentum

The momentum balance for an incompressible fluid which undergoes melting when crossing the solidus is given by,

$$-\frac{\partial \tau_{ij}}{\partial x_j} + \frac{\partial p}{\partial x_i} = \Delta\rho\lambda_i \tag{2.4}$$

where τ_{ij} is the deviatoric stress tensor (Equation, 1.13), p is the pressure perturbation, $\Delta\rho$ is the change in mantle density due to temperature and melting and λ_i is a unit vector in the vertical direction. What remains is to solve for $\Delta\rho$ that gives the changes in the gravitational body force due to changes in density due to melting and temperature, often referred to as buoyant creep or active flow.

Buoyant creep within the mantle is due to density changes caused by temperature perturbations, the presence of partially molten rock and depletion of the mantle matrix. This modifies $\Delta\rho$ in the momentum balance (Equation 2.4):

$$\Delta\rho(T, \phi, F) = -\rho_0 \left(\alpha T + \gamma\phi + \beta F\right) \tag{2.5}$$

Buoyancy due to temperature perturbations is parameterised by the thermal coefficient of expansion, α. Buoyancy due to melt retained within the mantle is given by the dependance on melt fraction by volume, ϕ, the amount of melt within the mantle mix and parameterised by the coefficient γ.

$$\gamma = \frac{\rho_m - \rho_l}{\rho_m} \tag{2.6}$$

Dependance on the depletion of the mantle matrix, F, the fraction by weight of melt removed from the rock, is parameterised by the coefficient β:

$$\beta = \frac{\rho_m - \rho_r}{\rho_m(X_r - 1)} \tag{2.7}$$

where ρ_l is the melt density, ρ_m is the reference density of the mantle, ρ_r is the density of the residual depleted mantle at $X_r = 1.3$ (see Section 2.2.1).

2.1.3 Viscosity: Rheology of the Mantle

The deviatoric stress tensor is given by (from Moresi and Solomatov, 1995),

$$\tau_{ij} = 2\eta\dot{\epsilon_{ij}} \qquad (2.8)$$

where viscosity, η is calculated from the following rheological definition for a non-Newtonian fluid that is also dependant on the presence of melt within the mantle matrix and dehydration f the mantle due to melting. The rheology follows that parameterised by Karato and Wu (1993) for a mantle tat is dominated by polycrystalline olivine,

$$\eta = A\chi_{H_2O}\chi_m exp\left(\frac{E + pV}{nRT}\right)\dot{\epsilon}^{\frac{1-n}{n}} \qquad (2.9)$$

where E and V are the activation energy and volume, R is the gas constant, T is the absolute real temperature, $\dot{\epsilon}$ is the strain rate and n is the stress exponent. A is calculated from a reference state that is set at the start of each model run. χ_{H_2O} and χ_m parameterise the effect of dehydration and melt respectively.

As discussed within Chapter 1 the mantle is slightly wet. It is estimated from the abundance of incompatible elements (those that remain preferentially within the melt) that there is 125 ± 75 ppm water within mid-ocean ridge basalt (Michael, 1995; Dixon et al., 1988; Michael, 1988). By estimating partition coefficients for water in olivine minerals, the dissolved water content within olivine is estimated to be within the range 810 ± 490 ppm (Hirth and Kohlstedt, 1996).

Modelling work by Robinson et al. (2001) using the partition coefficients of Hirth and Kohlstedt (1996) find that mantle water contents of between 150 and 300 ppm. Such a water content can explain observed water contents within mid-Atlantic Ridge, Southwest Indian Ridge and Juan de Fuca basalt (Robinson et al., 2001). Mantle melting for olivine containing 320 ppm water begins at ~ 90 km and for 810 ppm at ~ 115 km for a mantle potential temperature $1300\,^{\circ}$C (Hirth and Kohlstedt, 1996).

Because the effective viscosity of mantle materials is strongly dependant on volatile content, dehydration during melting causes a strengthening of the mantle. This increase in viscosity when dehydration occurs is included into the rheology by introducing a dehydration factor, χ_{H_2O}, as outlined in Nielsen and Hopper (2004). The dehydration factor increases linearly from 1 to 10 whilst wet melting progresses. After the generation

of 2 % melt the mantle strengthens, and so the viscosity is multiplied by 100 to simulate this strengthening (Braun et al., 2000). This pre-multiplier curve is based on the work of Hirth and Kohlstedt (1996), where it was found that for olivine aggregates the viscosity is reduced by a factor of 140 by the presence of water at a confining pressure of 300 MPa.

The presence of melt counteracts the strengthening effect of dehydration by reducing the viscosity and enhancing creep (Nielsen and Hopper, 2004). If more than 4 % melt is present the creep can be enhanced by more than one order of magnitude (Hirth and Kohlstedt, 1995). By fitting experimental data from Hirth and Kohlstedt (1995), Kelemen et al. (1997a) find the following relationship for the viscosity change due to melt,

$$\chi_m = e^{-45\phi} \tag{2.10}$$

where ϕ is the melt fraction by volume. It is likely that less than 3 % (per weight) of melt is retained (Hirth and Kohlstedt, 1995; Ito et al., 1999), so assuming 2 % melt is retained (as in Nielsen and Hopper, 2004) then the viscosity decrease due to retained melt is a factor of two.

2.1.4 Matrix Formation: Citcom

We us the finite element code, Citcom, that was developed at the California Institute of Technology (Moresi and Solomatov, 1995) to calculate problems concerning convection in the mantle. It solves the equations of flow, Equation 2.3 and 2.4 by first reforming them into the matrix equations,

$$\mathbf{A}\mathbf{u} + \mathbf{B}\mathbf{p} = \mathbf{f} \tag{2.11}$$

$$\mathbf{B}^T\mathbf{u} = 0 \tag{2.12}$$

where $\mathbf{A}$ is the stiffness matrix, $\mathbf{B}$ is the discrete gradient operator and $\mathbf{f}$ is a vector composed of the body and boundary forces acting on the fluid (Moresi and Solomatov, 1995). $\mathbf{u}$ and $\mathbf{p}$ are the linear velocity and constant pressure shape functions. Citcom solves these matrix equations using an iterative multigrid approach forming the coefficients $\mathbf{A}$, $\mathbf{B}$ and $\mathbf{f}$ using the standard finite element method, as outlined in Hughes (2000). To optimise performance a Gauss-Seidel relaxation method is used to increase the resolution of the model. A coarse grid is first formed and then this grid is bisected through each element iteratively to find the finest grid. The viscosity is then calculated from the interpolation of the temperature field within each element at the finest level. We made no alterations to these solver routines, and they are documented within Moresi and Solomatov (1995) and Nielsen and Hopper (2004).

2.2   Conservation of Energy

Once the flow has been calculated the energy balance must be solved. The energy balance is given by (from Scott, 1992),

$$\frac{\partial T}{\partial t} = -u_i \frac{\partial T}{\partial x_i} + \kappa \frac{\partial^2 T}{\partial x_j^2} - \frac{L\dot{m}}{c_p} \tag{2.13}$$

which relates the change in temperature with thermal advection and diffusion and the release of latent heat. κ is the coefficient of thermal diffusion. The latent heat of melting, $L = T_m \Delta S$, where T_m is a mantle reference temperature, ΔS is the entropy change due to melting and c_p is the specific heat. The last term is $\dot{m}$, the melt production rate.

2.2.1   Melting

The equation of conservation of momentum contains the term, $\Delta \rho$, to account for thermal and compositional buoyancy. Buoyancy due to melt within the melting region is given by the term $\gamma\phi$ in Equation 2.5. ϕ, the melt fraction by volume or porosity varies by advection, compaction and melting (see Scott, 1992).

$$\frac{\partial \phi}{\partial t} = -u_i \frac{\partial \phi}{\partial x_i} - (1-\phi)\frac{\partial u_j}{\partial x_j} + \dot{m} \tag{2.14}$$

Where the last term is once again $\dot{m}$, the melt production rate.

The amount of melting is modelled using a completely compatible element, *i.e.* one that has a partition coefficient $D \to \infty$. This completely compatible element remains always within the solid as melting progresses. From McKenzie (1984), the mass balance for liquid, density ρ_l, and solid, ρ_s, are governed by,

$$\frac{\partial}{\partial t}(\rho_l \phi) + \nabla \cdot (\rho_l \phi \mathbf{v}) = \frac{DM}{Dt} \tag{2.15}$$

$$\frac{\partial}{\partial t}(\rho_s(1-\phi)) + \nabla \cdot (\rho_s(1-\phi)\mathbf{u}) = -\frac{DM}{Dt} \tag{2.16}$$

DM/Dt is the rate at which mass is transferred from the matrix to the melt, $\mathbf{v}$ and $\mathbf{u}$ are the liquid and solid velocities and ϕ is the porosity. From Equation 2.16, the solid composition C_s is given by the following conservation (Spiegelman, 1996),

$$\frac{\partial}{\partial t}(\rho_s(1-\phi)C_s) + \nabla \cdot (\rho_s(1-\phi)\mathbf{u}C_s) = -\frac{DM}{Dt} \tag{2.17}$$

and by substitution of Equation 2.16 into an expanded Equation 2.17 we get,

$$\frac{\partial C_s}{\partial t} + \mathbf{u} \cdot \nabla C_S = \left(1 - \frac{1}{D}\right) \frac{C_s}{\rho_s(1-\phi)} \frac{DM}{Dt} \qquad (2.18)$$

Note the right hand side of this equation differs from Equation (14) of Spiegelman (1996) by a factor of -1. Our Equation 2.18 matches with the completely compatible trace element concentration, X of Scott (1992), where the rate of mass transfer $DM/Dt = \rho_s \dot{m}$,

$$\frac{\partial X}{\partial t} + \mathbf{u} \cdot \nabla X = \frac{X}{1-\phi} \dot{m} \qquad (2.19)$$

and $\dot{m}$ is the dimensionless melt production rate. In tensor notation this becomes,

$$\frac{\partial X}{\partial t} = -u_i \frac{\partial X}{\partial x_i} + \frac{X}{1-\phi} \dot{m} \qquad (2.20)$$

The concentration, X, of a perfectly compatible trace element is always positive, and equal to one when no melting has occurred. Values of X greater than one indicate material from which melt has been extracted, values less than one indicate material which has had melt added by *in situ* freezing (Scott, 1992). Assuming batch melting, where the melt remains in equilibrium within the melting column and is only removed at the upper boundary (Plank et al., 1995), the quantity X can be related to a degree of depletion due to melting F, as defined in Scott and Stevenson (1989), by:

$$X(1 - F) = 1 \qquad (2.21)$$

As such for small melt fractions $\Delta X \approx \Delta F$. This assumption has been made within the momentum balance, Equation 2.4.

2.2.2 Melt Production Rate

The melt production rate, $\dot{m}$, couples the energy balance (Equation 2.13) and equations of continuity of porosity and composition (Equations 2.14 and 2.20). To calculate $\dot{m}$, a solidus, T_s is defined. Normally the solidus is defined as a function of depth. However here following Scott (1992) and Phipps Morgan (2001) it is a function of depth and depletion X,

$$T_s^{real} = T_{s0} + z \left(\frac{\partial T_s}{\partial z}\right)_X + \left(\frac{\partial T_s}{\partial X}\right)_z (X - 1) \qquad (2.22)$$

where T_s^{real} is the temperature of the solidus. Assuming the changes in X due to malting are small, then expanding Equation 2.21 as a Taylor series and taking a first
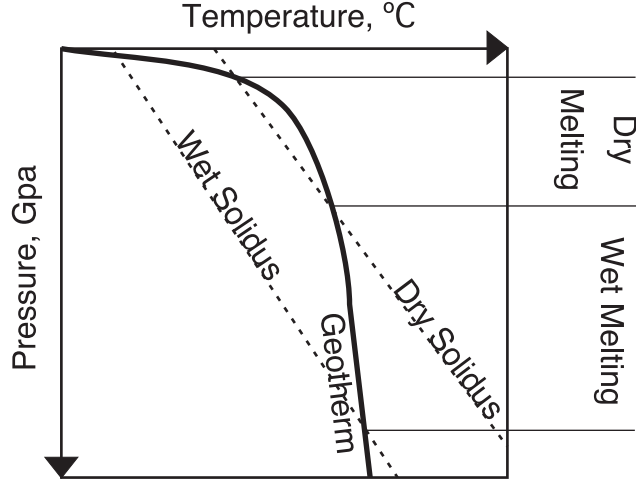
FIGURE 2.1: Diagram of the 'wet' and 'dry' solidus curves in pressure and temperature space. A example geotherm is plotted showing where wet and dry melting occur.

order approximation, $X = 1 + F$ and $dX = dF$ then the change in temperature due to melting is as in Phipps Morgan (2001),

$$dT = dT_s = \left(\frac{\partial T_s}{\partial z}\right)_F dz + \left(\frac{\partial T_s}{\partial F}\right)_z dF \qquad (2.23)$$

Equation 2.22 is converted to the potential temperature by correcting for the adiabatic temperature change,

$$\left(\frac{\partial T}{\partial z}\right)_S = \frac{g\alpha T}{c_p} \qquad (2.24)$$

leading to,

$$T_s = T_{s0} + z\left(\left(\frac{\partial T_s}{\partial z}\right)_X - \left(\frac{\partial T}{\partial z}\right)_S\right) + \left(\frac{\partial T_s}{\partial X}\right)_z (X - 1) \qquad (2.25)$$

The dependence on depletion adjusts the solidus as melting continues. The depth derivative of the solidus at constant depletion $(\partial T_s/\partial z)_X$ is equal to $3.4 \times 10^{-3}\,\mathrm{K\,m^{-1}}$ and the depletion derivative of the solidus at constant depth $(\partial T_s/\partial X)_z$ is equal to $440\,\mathrm{K}$ (Nielsen and Hopper, 2004). As the source rock rises and melts by decompression, mantle volatiles preferentially partition into the melt. Once 1-2 % of melt is produced the volatiles are thought to have left the depleted residue and are completely within the melt (Hirth and Kohlstedt, 1996). Melting beyond 2 % is then dry, as all the volatiles have left the solid. Thus within the model a distinction is made between the wet solidus, where mantle that contains water melts, and the dry solidus (see Figure 2.1). Wet melting occurs until 2 % of melting has occurred, *i.e.* while $\Delta X = X - 1 < 1.02$. The wet solidus, T_{wet}, is defined as being an amount below the dry solidus, T_s, following Braun

et al. (2000):

$$T_{wet} = T_s - 200 \left(\frac{1.02 - X}{\Delta X} \right) \tag{2.26}$$

Melting occurs if the potential temperature exceeds this solidus. The amount of melting at each time step is then given by (Scott, 1992),

$$\delta m = \frac{\delta T}{\frac{L}{c_p} + \frac{\partial T_s}{\partial \phi}} \tag{2.27}$$

where $\delta T = T - T_s$ or $\delta T = T - T_{wet}$ depending on how much melt was generated previously, L is the latent heat, and c_p is the specific heat capacity. The differential, $\partial T_s / \partial \phi$ is given by; in the wet melting regime (from Nielsen and Hopper, 2004),

$$\frac{\partial T_s}{\partial \phi} = 1440 \frac{X}{1 - \phi} \tag{2.28}$$

and when in the dry melting regime,

$$\frac{\partial T_s}{\partial \phi} = 440 \frac{X}{1 - \phi} \tag{2.29}$$

The melt production rate is then simply,

$$\dot{m} = \frac{\delta m}{\delta t} \tag{2.30}$$

where δt is the advection time step.

2.2.3 Igneous Crustal Thickness

One tool used repeatedly within this thesis is a measure of the igneous crustal thickness. This measure is calculated following Ito et al. (1996): the average extent of melting is first calculated by weighting the degree of melting, F, by the melt production rate, $\dot{m}$. The igneous crustal thickness, h_c, is then estimated by assuming all the melt is focused to the ridge or rift axis and accretes there,

$$h_c = \frac{2}{u_z} \left(\frac{\rho_0}{\rho_m} \right) \int \dot{m} dx_i \tag{2.31}$$

2.2.4 Petrov-Galerkin Solver

We apply the streamline upwind/Petrov Galerkin formulation to solve the equations for the conservation of energy and continuity of porosity and composition (Equations 2.13,

2.14 and 2.20). We use the routines unaltered from those applied used within Moresi and Solomatov (1995) and Nielsen and Hopper (2004), which are outlined in Brooks and Hughes (1982). The stability criterea for the streamline upwind/Petrov Galerkin routine is that the Courant number ($Cr = \delta t\, u/h$), where δt is the advection time step, u is the flow field and h is the element spacing, is given by,

$$Cr \leqslant 0.8 \tag{2.32}$$

if the element Peclet number ($\alpha_p = uh/2k$), where k is the diffusivity, is greater or equal to 100. Otherwise,

$$Cr \leqslant min(1, \alpha) \tag{2.33}$$

These stability criteria have proven to hold for the combined Navier-Stokes equation of flow past a cylinder (Brooks and Hughes, 1982), and for modelling mantle convection under high viscosity contrasts (Moresi et al., 1996). In this case, the advection time step solved using equations 2.11 and 2.12, must equally meet these stability conditions.

2.3 Melt Composition

2.3.1 Major Elements

The major element oxides are, aluminium, calcium, iron, magnesium, potassium, silicon, sodium and titanium. Here we shall outline the methods for calculating the primary melt composition. The code used within the model is a modified version of the melt composition calculations by Dean et al. (Submitted). I consider two methods:

1. The major element composition of accumulated melt is linked to the fraction of melt generated and pressure by fitting polynomial functions to large data sets from batch melting experiments (McKenzie and Bickle, 1988). This is an inverse method, *i.e.*the melt composition is calculated backwards from the the bulk silicate Earth ($C(1)$ within Table 2.1). Additional corrections to the iron and magnesium oxides to maintain consistency with the olivine/liquid partition coefficient were made to this parameterisation by Watson and McKenzie (1991), which is referred to as WM91.

2. An alternative approach to quantifying the composition of the melt is to use the partition coefficient, D, that determines the ratio of a particular oxide within the solid and liquid parts.

$$D = \frac{C_s}{C_l} \tag{2.34}$$

C_s is the weight percent solid composition and C_l is the liquid composition. By using the melting experiments of Jaques and Green (1980); Falloon et al. (1988); Hirose and Kushiro (1993) and Baker and Stopler (1994), Niu (1997) calculates the apparent partition coefficients for the major elements as a function of temperature and degree of melting by constructing a mass balance, which shall be refered to as N97 Niu and Batiza (1991); Niu (1997). Due to the lack of available data, N97 compositions at melt fractions less than 1% and at pressures greater than $2.5\,\mathrm{GPa}$ are poorly constrained Niu (1997). For fractions of melting less than 1% we calculate the partition coefficient assuming 1% melt and for pressures greater than $2.5\,\mathrm{GPa}$ we similarly calculate the partition coefficients at $2.5\,\mathrm{GPa}$.

2.3.1.1 Watson and McKenzie Parameterisation

WM91 relates the instantaneous melt composition of the major elements oxides: titanium, aluminium, iron, magnesium, calcium, sodium, potassium and 'the rest' to the degree of depletion F following,

$$C(F) = a + b(1 - F)^{\frac{1-D}{D}} \tag{2.35}$$

where D is the partition coefficient (Equation 2.34). 'The rest' are all other oxides except silicon, and are lumped together as one term. Silicon is then calculated as 100% minus all the other oxides. The melt region from $0 < F < 1$ is split into three regions, $0 \rightarrow F_1$, $F_1 \rightarrow F_2$ and $F_2 \rightarrow 1$, to allow adjustment of the parameters, a and b to fit the data. We are interested in the point average composition, $\mathscr{C}$, which is related to C following McKenzie and Bickle (1988),

$$C = \frac{d}{dF}(F\mathscr{C}) \tag{2.36}$$

and by integrating Equation 2.36, we get the relationship,

$$\mathscr{C}(F) = a + \frac{bD}{F}\left(1 - (1 - F)^{\frac{1}{D}}\right) + \frac{}{F} \tag{2.37}$$

where a, b and d are determined from the available data from each element to provide the best fit, D is the partition coefficient for each major oxides. The point average composition is required to be continuous across F_1 and F_2. $C(0)$ is finite and so d is zero within the first interval $F < F_1$,

$$\mathscr{C}(0) = a + b \tag{2.38}$$

TABLE 2.1: Parameters used in the Watson and McKenzie (WM91) parameterisation. These are the preferred parameter values taken from Table C3, Watson and McKenzie (1991).

	SiO$_2$	TiO$_2$	AL$_2$O$_3$	FeO	MgO	CaO	Na$_2$O	K$_2$O	'the rest'
$\mathscr{C}(0)_{P=0}$	52.20	2.06	12.65	6.235	7.56	11.68	2.90	0.32	0.39
D		0.086	0.5	0.5		0.8	0.2	0.5	
$(d\mathscr{C}/dP)_{F=0}$				1.67					
$\mathscr{C}(0)_{P=0}$				7.21					
$(d\mathscr{C}/dP)_{F=F_1}$				1.57					
$D_{F>F_2}$				0.623					
$(F_1)_{P=0}$		0.247	0.224	0.226	0.226	0.247	0.224	0.247	
F_2				0.247	0.247				
dF_1/dP		0.045	0.058			0.045	0.068	0.045	
$K_{\overline{D}}$				0.263	0.263				
$\mathscr{C}(1)$	45.16	0.171	3.31	8.5	39.2	2.78	0.42	0.070	0.39
misfit %	0.81	0.24	0.93	0.97	1.00	1.07	0.29		

also,

$$\mathscr{C}(1) = a + \frac{b}{(1/n) + 1} + d \tag{2.39}$$

where d for $F > F_1$ is a constant determined by the following minimisation (Watson, 1991). The parameters a, b and d are calculated by minimising the misfit: the difference between the observed and calculated composition (Watson, 1991; Watson and McKenzie, 1991). The following constraints applied: F_1 and F_2 are held constant, except for aluminium and sodium oxides, when if the pressure is less than $1.5\,\text{GPa}$ the value of F_1 is altered to allow a better fit. The second constraint is on iron and magnesium oxides: to maintain consistency with the partition coefficient of olivine/liquid, requiring the following,

$$K_{\overline{D}} = \frac{(\text{MgO/FeO})_{\text{l}}}{(\text{MgO/FeO})_{\text{s}}} \tag{2.40}$$

to be constant and independent of pressure between 0 and F_2. This leads to a series of equations that are solved to find a, b and d from the list of parameters in Table 2.1.

To incorporate this parameterisation within the model, we need to extract information of the pressure and degree of depletion at every element. To find the pressure involves simply calculating the pressure from the known depth and density of material above. The degree of depletion, F is related to X, the concentration of a perfectly compatible trace element, by Equation 2.21, and so is also known at every node point. Therefore, if
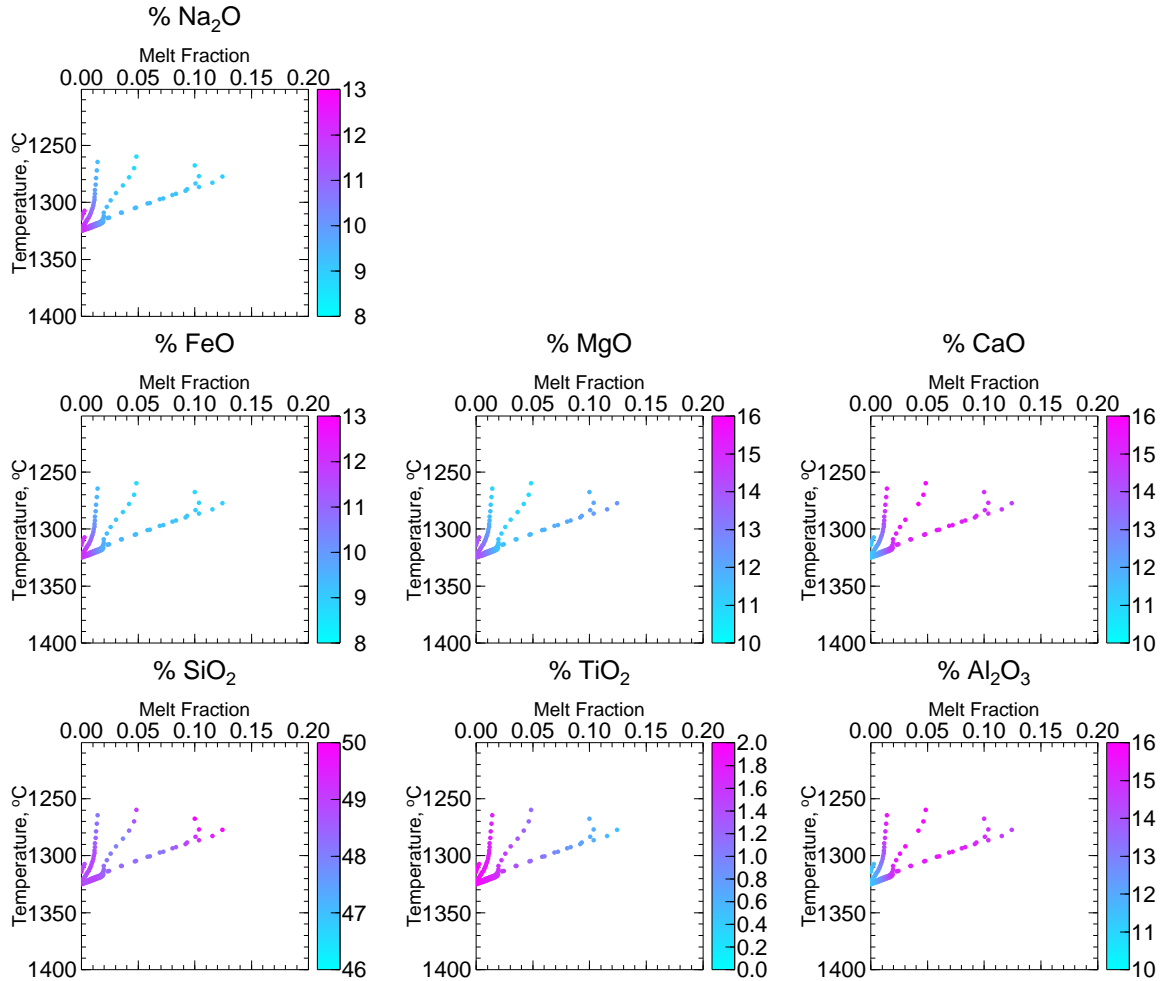
FIGURE 2.2: Major element composition at 6 Myrs plotted against mantle temperature and melt fraction. The Watson and McKenzie (1991) major element composition parameterisation has been used. Rifting and extension is driven by a upper surface boundary condition of a half spreading rate of $10 \, \text{mm} \, \text{yr}^{-1}$ and the mantle potential temperature in this case is $1325 \, ^\circ \text{C}$. The curves are from various melt generation paths that pass through the melt region due to the flow of the mantle beneath the lithosphere.

there is melt present, then the composition can be calculated by employing a reasonably simple look up table.

The statistical empirical approach of WM91 to generate a function for the composition of melt overestimates calcium oxide concentrations at low fractions of melting (Langmuir et al., 1992). The bulk partition coefficient for sodium oxide is also grossly over estimated, leading Langmuir et al. (1992) to suggest that the WM91 parameterisation is not much of an improvement upon more simplistic smoothed isobaric melting paths (e.g. Klein and Langmuir, 1987). However WM91 is a robust quantitative parameterisation
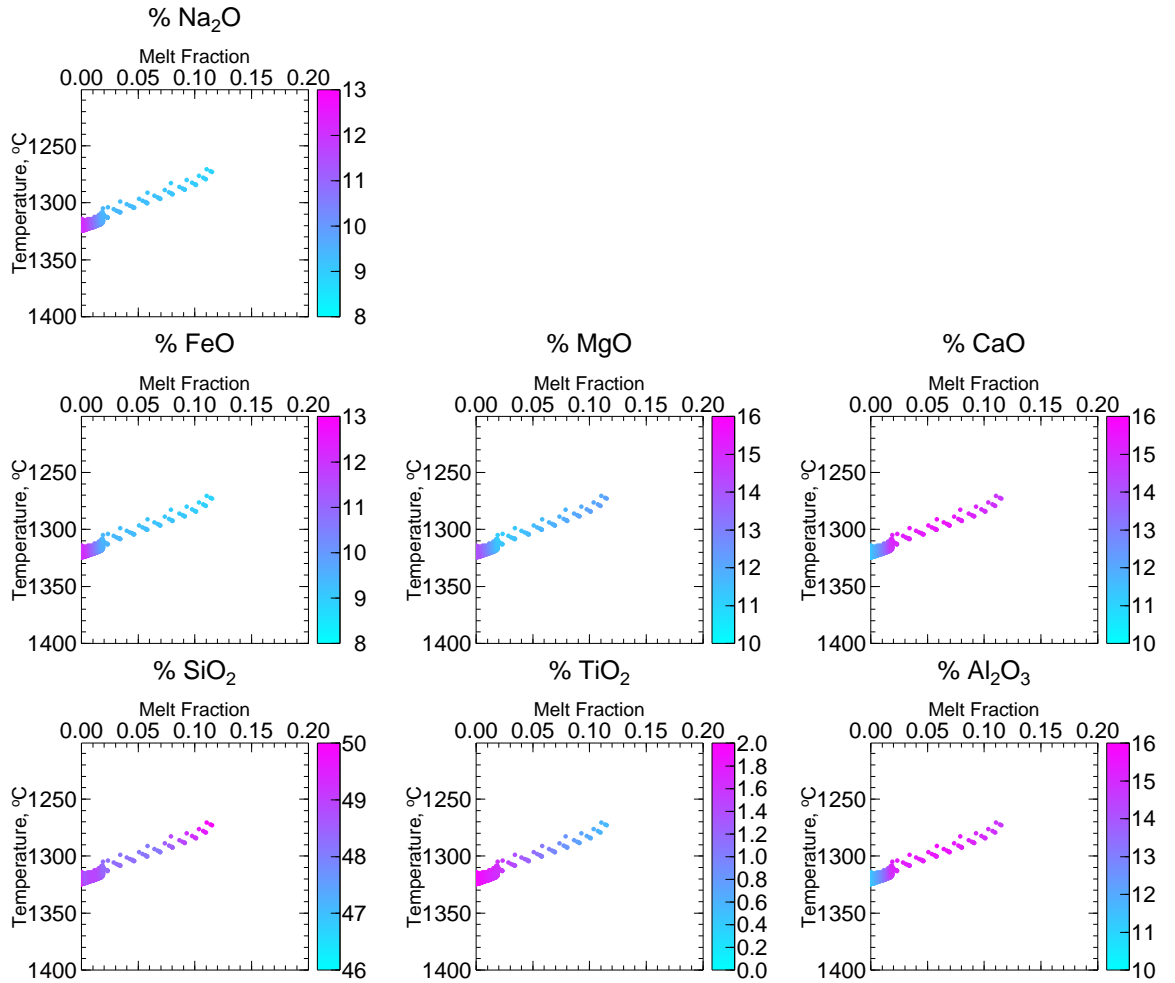
FIGURE 2.3: Major element composition at 80 Myrs plotted against mantle temperature and melt fraction. The Watson and McKenzie (1991) major element composition parameterisation has been used. Rifting and extension is driven by a upper surface boundary condition of a half spreading rate of $10\,\mathrm{mm\,yr^{-1}}$ and the mantle potential temperature in this case is $1325\,^{\circ}\mathrm{C}$. The curves are from various melt generation paths that pass through the melt region due to the flow of the mantle beneath the lithosphere. In this case steady state see floor spreading has been set up.

and can be used within melting models with relative ease due to the simple polynomial relationships that relate instantaneous melt composition to the fraction and pressure of melting. The predicted melt compositions at during rifting and at sea floor spreading are displayed in Figures 2.2 and 2.3.

2.3.1.2 Niu Parameterisation

The Niu parameterisation uses a range of experimental data to determine the partition coefficients for each major element. For silicon, aluminium and calcium oxides:

$$D_i = e_i + f_i \% F + \frac{g_i}{\% F} + h_i P \tag{2.41}$$

where $\% F$ is the percent melt depletion and P is pressure in kBar. For titanium and sodium oxides:

$$D_i = e_i + f_i F + g_i F^2 + h_i F^3 \tag{2.42}$$

where F is the melt depletion. For magnesium and potassium oxides:

$$D_i = e_i + f_i F + h_i P \tag{2.43}$$

Finally for iron oxides:

$$D_i = e_i + f_i F + h_i P + k_i D_{MgO} \tag{2.44}$$

where e_i, f_i, g_i, h_i and k_i are given in Table 2.2. Once the partition coefficients for each major element have been calculated for the particular time step, then the streamline upwind/Petrov Glerkin solver is used to solve Equation 2.18 for each major element. The predicted melt compositions at during rifting and at sea floor spreading are displayed in Figures 2.4 and 2.5. A visual comparison with Figures 2.4 and 2.5 suggests that these two parameterisations are within general agreement.

2.3.1.3 Mean Melt Composition

I calculate the mean melt composition following McKenzie and Bickle (1988),

$$\overline{C}_i = \frac{\int \int_{melt} FC dx dz}{\int \int_{melt} F dx dz} \tag{2.45}$$

where the integrals are over the melt region and the mean composition is for each element oxide i.
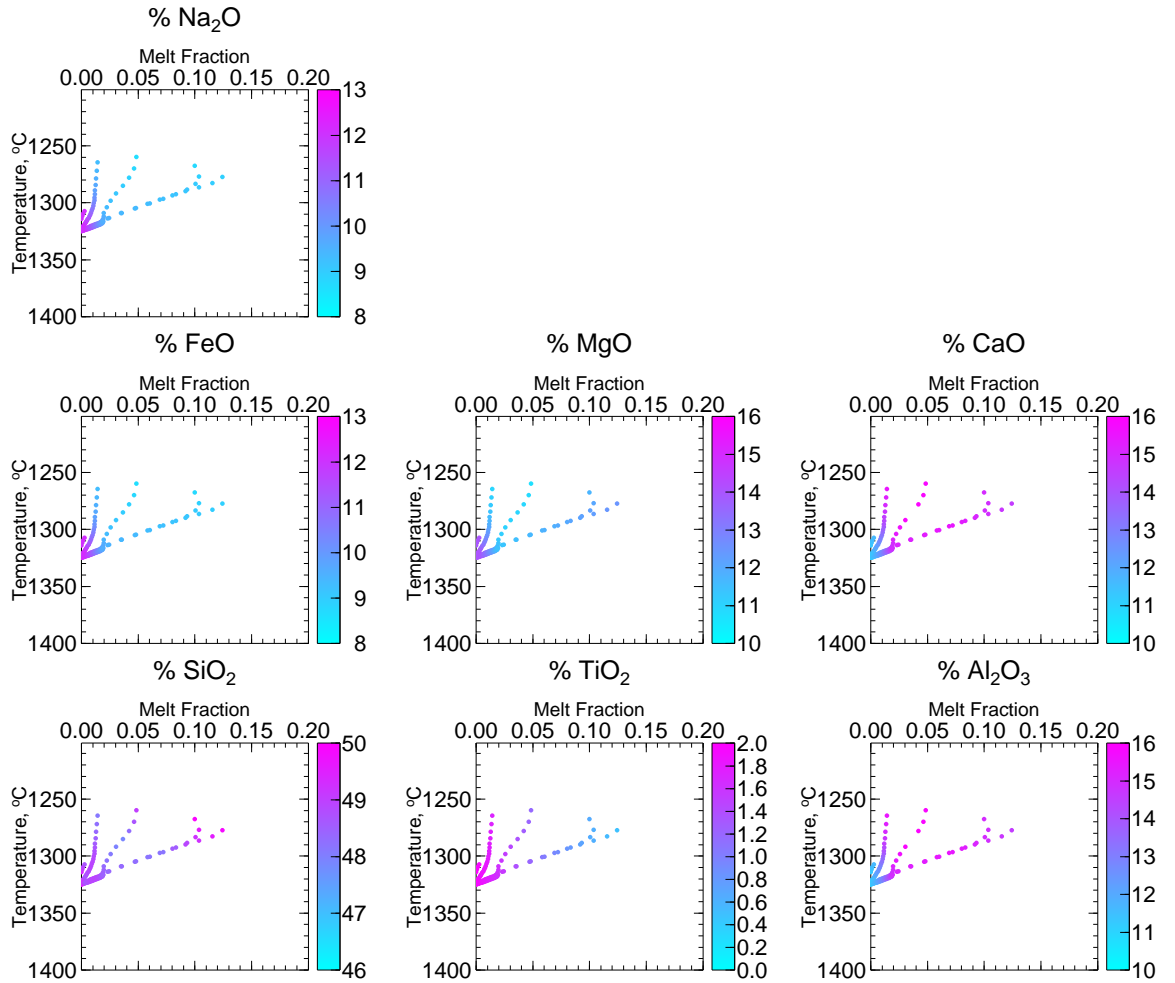
FIGURE 2.4: Major element composition at 6 Myrs plotted against mantle temperature and melt fraction. The Niu (1997) major element composition parameterisation has been used. Rifting and extension is driven by a upper surface boundary condition of a half spreading rate of $10\,\mathrm{mm\,yr^{-1}}$ and the mantle potential temperature in this case is $1325\,^{\circ}\mathrm{C}$. The curves are from various melt generation paths that pass through the melt region due to the flow of the mantle beneath the lithosphere.
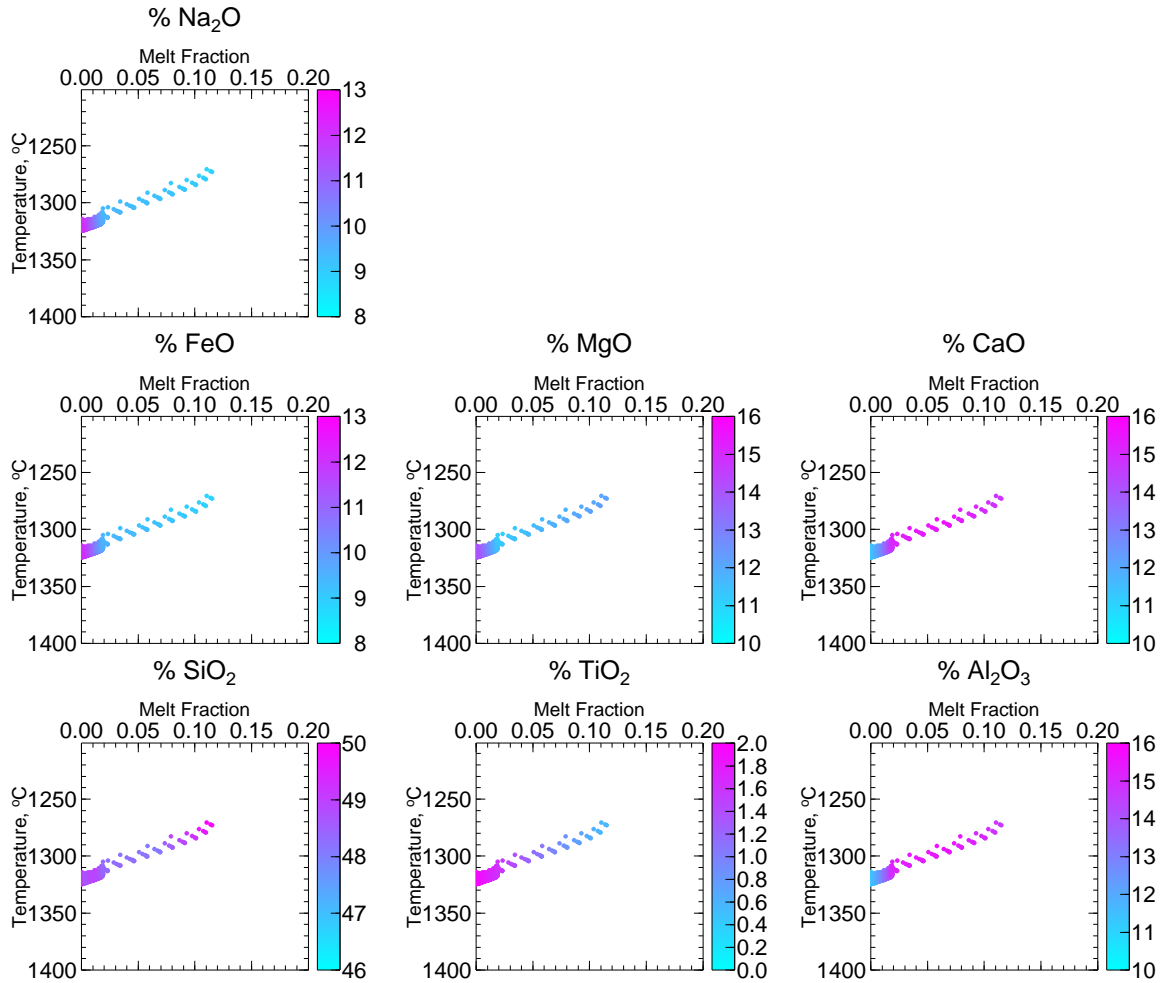
FIGURE 2.5: Major element composition at 80 Myrs plotted against mantle temperature and melt fraction. The Niu (1997) major element composition parameterisation has been used. Rifting and extension is driven by a upper surface boundary condition of a half spreading rate of $10 \, \text{mm} \, \text{yr}^{-1}$ and the mantle potential temperature in this case is $1325 \, °\text{C}$. The curves are from various melt generation paths that pass through the melt region due to the flow of the mantle beneath the lithosphere. In this case steady state see floor spreading has been set up.

TABLE 2.2: Coefficients used in the Niu parameterisation for major element composition calculations.

D	i	e	f	g	h	k
Si	1	0.8480	-0.0022		0.0055	
Ti	2	0.1064	-0.7502	1.3236		
Al	3	0.1890	-0.0051	-0.0250	0.0010	
Fe	4	0.3169	0.3695		-0.0034	0.2130
Mg	5	5.2000	-4.5664		-0.0594	
Ca	6	0.3180	-0.0122	0.2720	0.0005	
Na	7	0.0639	-0.5787	2.4763	-3.6717	
K	8	0.0690	-0.00002			

2.4 Extension and Subsidence

Extension and subsidence is estimated from the calculated density structure, extension and loading. An isostatic balance is constructed from the density structure (Equation 2.5) of the mantle at incremental positions on the extending crust,

$$\rho_m(z,t) = \rho_0 \left(1 - \alpha T(z,t) + \gamma \phi(z,t) + \beta_F F(z,t)\right) \tag{2.46}$$

from the temperature, T, porosity, ϕ and melt depletion, F. The density ρ_i and thickness h_i of the load of igneous material emplaced during rifting is known from estimates of the volume of melt and the crystallisation of that melt. Finally by the addition of tracers, a stretching factor, $\beta_e(t)$, can be estimated and so the thickness of the stretched continent is calculated. The balance is as follows,

$$\rho_c h_c + \int_{h_c}^{h_\infty} \rho_m(z,t_0)dz = \rho_w h_w + \rho_i h_i + \rho_c \frac{h_c}{\beta_e(t)} + \int_{h_i + \frac{h_c}{\beta_e(t)}}^{h_\infty} \rho_m(z,t)dz \tag{2.47}$$

Where t_0 is time $= 0$ *i.e.* at the initial condition. h_c is the continental thickness of 30 km, h_w is the subsidence, and h_∞ is the base of the model region, so in the far field . By making the definition,

$$I_0 = \int_{h_c}^{h_\infty} \rho_m(z,t_0)dz \tag{2.48}$$

and re-arranging, and solving for the subsidence h_w:

$$h_w = \frac{1}{\rho_w} \left(I_0 + \rho_c h_c(1 - \frac{1}{\beta_e(t)}) - \rho_i h_i - \int_{h_i + \frac{h_c}{\beta_e(t)}}^{h_\infty} \rho_m(z,t)dz \right) \tag{2.49}$$

The predicted subsidence can then be used to estimate the period of extension required to match observed subsidence curves within extensional basins (see Chapter 5).

2.5 Model Setup

2.5.1 Dimensionless Treatment of Model Equations

The equations of conservation of mass, momentum and energy (Equations 2.3, 2.4 and 2.13) are made dimensionless using the following relationships,

$$x = dx' \tag{2.50}$$

$$t = \frac{d^2}{\kappa}t' \tag{2.51}$$

$$T = T_d T' \tag{2.52}$$

$$\eta = \eta_0 \eta' \tag{2.53}$$

where d is the depth to the base of the model (700 km); κ is the thermal diffusivity $(10^{-6}\,\mathrm{m^2\,s^{-1}})$; T_d is the super-adiabatic temperature drop to the base of the model and is set to different values to represent different mantle conditions; and finally η_0 is the scaling viscosity set from the thermal Rayleigh number,

$$Ra = \frac{\alpha g \rho T_d d^3}{\kappa \eta_0} \tag{2.54}$$

where α is the coefficient of thermal expansion $(3.3 \times 10^{-5}\,\mathrm{K^{-1}})$; and g is the acceleration due to gravity $(9.8\,\mathrm{m\,s^{-1}})$.

The viscosity is then constrained to be within six orders of magnitude of the reference viscosity. Viscosity is then given by Equation 2.9,

$$\eta = A\chi_{H_2O}\chi_m exp\left(\frac{E + PV}{nRT_A}\right)\dot{\epsilon}^{\frac{1-n}{n}}$$

where χ_{H_2O} and χ_m are as described in Section 2.1.3; E, the activation energy is $530 \times 10^3\,\mathrm{J\,mol^{-1}}$; V, the activation volume is $5 \times 10^{-6}\,\mathrm{m^3\,mol^{-1}}$; R, the gas constant is $8.314\,\mathrm{J\,K^{-1}\,mol^{-1}}$; and T_A is the absolute real temperature in Kelvin; and n is the stress exponent and is set to 3. Finally, the parameter A is defined by a reference state at a temperature of 1598 K and a strain rate, $\dot{\epsilon} = 1 \times 10^{-15}\,\mathrm{s^{-1}}$.
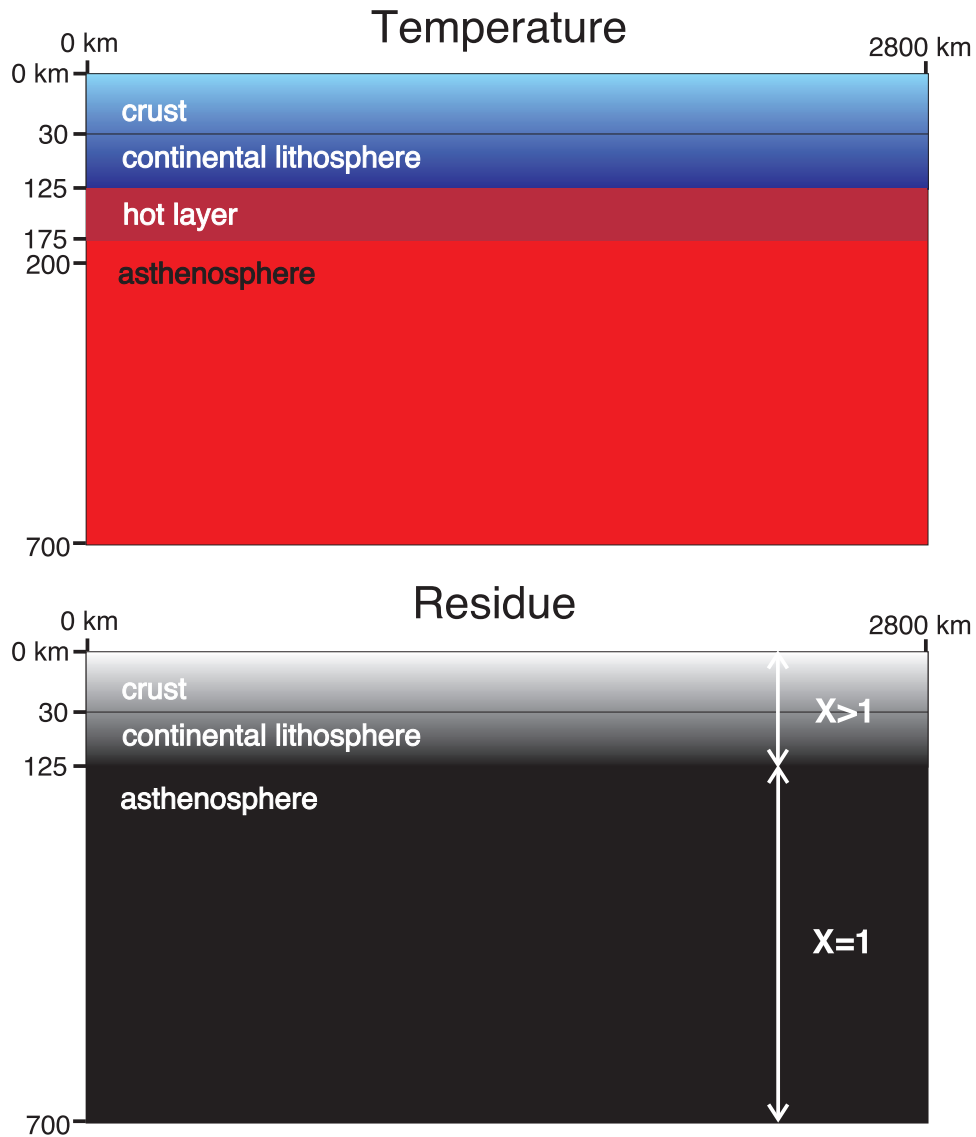
FIGURE 2.6: Model space for models of rifting and the extension of the lithosphere.

2.5.2 Initial Conditions

Initial conditions are formed by defining temperature and the melting residue, X, at every node of the finite element mesh (as shown in Figure 2.6). If major element composition is being calculated using the Niu (1997) parameterisation (Section 2.3.1.2), then a primitive mantle composition must be defined at every node. The number of elements can be set to be coarse, for example 32 by 32 elements, or fine, such as 257 by 257 elements. The resolution of the grid is limited by processor memory. For most models a grid size of 257 by 257 is chosen as it makes an appropriate balance between accuracy and computation time.

CitCom is compiled in 32 bit, and computations were performed on various platforms. Most of the results presented were generated using the cluster of IBM Intellistation-Z workstations with 2 GHz AMD Opteron 246 processors, with 2 GB RAM, running various releases of Red Hat Linux and an Apple Mac 1.83 CHz Intel Core Duo with 1 GB of RAM running OS X version 10 at the National Oceanography Centre, Southampton. Compilation of *CitCom* on the Apple Mac required minor modification of gcc version 3.0 to allow operation in 32 bit.

2.5.3   Boundary Conditions

Boundary conditions are of free slip along all boundaries unless a velocity has been defined. No material can flow across the boundaries, and so they are chosen to be far away from the region of interest to limit the effect of these boundary conditions. Extension and rifting of the lithosphere is driven by constant velocity conditions on the upper surface. The velocity can be ramped along the surface from zero to the chosen value.

2.5.4   Model Stability

There are two constraints that must be met to maintain stability within the model. The first is that the advection time step used to solve Stokes equations (Equations 2.11 and 2.12) must meet the stability conditions for the Petrov-Galerkin solver (Equations 2.32 and 2.33). The second is that discontinuities in viscosity must not be too large within elements (Moresi et al., 1996). For all reasonable earth system models, both these conditions are met (Moresi et al., 1996; Moresi and Solomatov, 1995; Brooks and Hughes, 1982).

2.6   Summary

1. The major and rare-earth primary melt composition parameterisations have been successfully integrated within *CitCom*, the modular finite element solver for the combined Stokes and energy equations developed by Moresi et al. (1996) and Nielsen and Hopper (2004).

2. The code runs to stable solutions when following the criteria outlined within Moresi et al. (1996). The penalty parameter for the multigrid solver should be 1×10^5 to produce converging solutions.

Chapter 3

Steady State Igneous Crustal Thickness

3.1 Introduction

Before modelling the complexities of the rifting of continents, the geodynamic model of the extension of the continental lithosphere developed in the previous Chapter is verified at steady state. I will take the steady state solution to be when the total melt production has become constant with time. Such a state should match that of sea floor spreading in terms of igneous crustal thickness predicted, such as at the Mid-Atlantic Ridge or East Pacific Rise. To verify the model basic parameterisation, the primary aim here is to compare steady state igneous crustal thickness predicted by the model with observed mid-ocean crustal thickness. The effect of dehydration within the mantle due to melt production will then be explored, in relation to melt production a slow spreading margins.

3.1.1 Steady State Sea-floor Spreading

Mid-ocean ridge basalts (MORB) with 10-13 % MgO are estimated to be formed from mantle potential temperature range between 1280 and 1400 °C (Herzberg et al., 2007). McKenzie et al. (2005) recently estimated the mantle potential temperature at 1315 °C. Previous models of rifting have used various mantle temperatures that generally fall within this range. The choice of potential temperature, however, is quite important. McKenzie et al. (2005) show that a 12.5 °C increase in mantle temperature increases crustal thickness by 1 km.

Within models of margin formation the mantle potential temperature is normally set to match the global mid-ocean igneous crustal thickness, which is estimated to be around 7 km away from hotspots, fracture zones and magma-poor margins (White et al., 1992). The choice potential temperature within the model is dependant on the change in entropy, ΔS. Estimates of ΔS vary between 200 and 500 $\mathrm{J\,K^{-1}\,kg^{-1}}$ (McKenzie and Bickle, 1988; McKenzie and O'Nions, 1991; Kojitani and Akaogi, 1997; Ito and Mahoney, 2005; McKenzie et al., 2005). Hirschmann et al. (1998) calculate the change in entropy of the melting reaction for peridiotite and find that it can vary between 250 to 500 $\mathrm{J\,K^{-1}\,kg^{-1}}$. It was also found that melt production was not greatly effected by this variation in the change in entropy. They suggest that a suitable value for melting up to a depth of 3 GPa would be 300 $\mathrm{J\,K^{-1}\,kg^{-1}}$.

At the Rekyjanes Ridge south of Iceland in the mid-Atlantic, the crust is slightly thicker at 8 to 11 km (Smallwood and White, 1998; Weir et al., 2001; Jacoby et al., 2007). Given the wide range in values for the change in entropy of melting suggested in the literature, and as the melting equations within my model of rifting and extension are based on Scott (1992), I have chosen to use their value of $\Delta S = 250\,\mathrm{J\,K^{-1}\,kg^{-1}}$. Following this choice of the change in entropy, here mantle potential temperatures of between 1275 and 1325 °C have been chosen to examine the complete range of behaviours that might be expected.

3.1.2 Effects of Dehydration Strengthening

At slow spreading ridges, the predicted igneous melt thickness from geodynamic models of the rifting of continents often underestimates the volume of melt measured from rare-earth inversion and seismic refraction surveys, once sea floor spreading has been achieved (Bown and White, 1994; White et al., 2001). The kinematic model developed by Bown and White (1994) can recreate the observed crustal thickness at slow spreading rates. However this model requires a wedge of thinned crust that focuses flow (creep) of the mantle to the ridge axis. The wedge geometry is designed to approximate the thickening of the lithosphere due to cooling (Spiegelman and McKenzie, 1987). But, such models do not explain the origin of such focussing of the mantle flow.

A possible mechanism that may produce the focussing of mantle flow is rheological changes due to the dehydration of the mantle as it melts. The increased viscosity in the melt region may help to confine flow into a narrow region of upwelling material (Minshull et al., 2001). Some initial melting at slow rates of extension is required to dehydrate the mantle. The dehydrated mantle will then confine a narrow region of low un-dehydrated mantle, where upwelling would become vigourous enough to generate subsequent melt

(Minshull et al., 2001). This hypothesis is reliant on the dehydration creating a narrow region of lower viscosity, rather than just dampening all upwelling.

The dehydration strengthening parameter is applied to the rheology of the geodynamic model as outlined in Chapter 2. Following Nielsen and Hopper (2004), the simplistic definition that once 2 % of melt has been generated the viscosity of the mantle increases. This gives the rheological equation (see Section 2.1.3):

$$\eta = A\chi_m\chi_{H_2O}exp\left(\frac{E + pV}{nRT}\right)\dot{\epsilon}^{\frac{n-1}{n}} \tag{3.1}$$

χ_{H_2O} is the dehydration strengthening pre-multiplier, χ_m is the reduction in viscosity due to melt retention in mantle, the fourth term is the Arrhenius style relationship for temperature and pressure, and the last term is the strain rate dependance. Calculation of viscosity is in four steps: first the Rayleigh number for the complete model domain is defined (see Section 2.5.1) and from this the Stokes equations are solved giving the temperature and flow. The viscosity can then be calculated from the resulting temperature and pressure fields with the addition of the pre-multipliers and stress dependance. The rheology then feeds back into Stokes equations and the process is repeated. χ_{H_2O} is chosen to represent an increase by 100 in the viscosity of the mantle upon dehydration (Nielsen and Hopper, 2004) based mainly on the work of Hirth and Kohlstedt (1996), see Section 1.5.2.

In this chapter the melt composition parameterisation of Watson and McKenzie (1991) has been applied to understand the variation in major element compositions with spreading rate. Observations show that FeO and the CaO/Al_2O_3 ratio decrease and that Na_2O increase with decreasing spreading rate (Bown and White, 1994). The question examined here is the extent to which strengthening of the mantle due to dehydration acts to constrict flow into a narrow upwelling region. This enhanced focussing effect has been proposed as one way to reconcile model predictions of crustal thickness with observed global trends in crustal thickness, whilst reproducing a reasonable trend in major element composition of melt.

3.2   Model Boundary Conditions

The combined Stokes equations of flow and conservation of energy are made dimensionless (see Section 2.5.1) and solved using the multigrid finite element solver *CitCom* (Moresi et al., 1996). For speed of model runs and accuracy we chose to run at a grid dimension of 257×257. Model space is a region 700 km deep by 2800 km long (see Figure
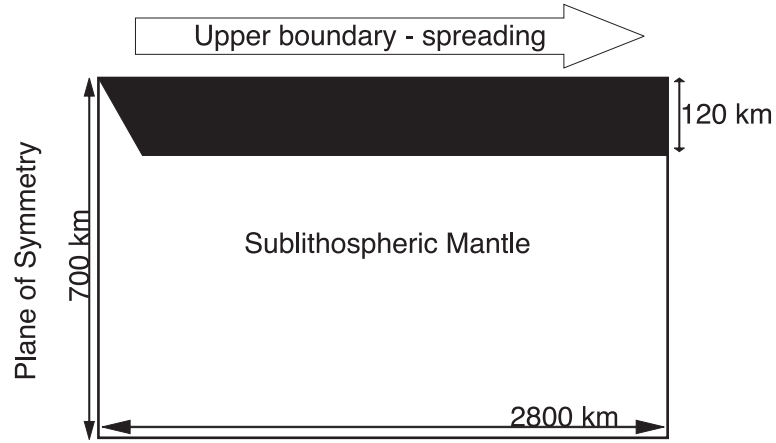
FIGURE 3.1: Diagram of model region. It can be seen that the bottom and right boundaries are far from this region of interest.

3.1). On the top boundary the temperature is held at $0\,^{\circ}$C and the base temperature is set to reflect the mantle potential temperature of between 1275 and $1325\,^{\circ}$C. As with all models presented within this thesis, right and left boundaries are reflecting, $\partial T/\partial x = 0$; there is no lateral heat or material flow across these boundaries. To the right and base, the boundaries are held far from the region of interest, so the boundary conditions do not interfere with the model evolution.

3.3 Results and Discussion

Solutions to the equations of flow were sought for a scaling mantle viscosity, $\eta_0 = 4.5 \times 10^{20}\,$Pa s (see Equation 2.54). A lower viscosity results in excessive time dependance in the melt production and steady state crustal melt production is never achieved (Nielsen and Hopper, 2004). A viscosity of $4.5 \times 10^{20}\,$Pa s is likely representative of normal rift evolution (Nielsen and Hopper, 2004). To look at the effects of mantle temperature on igneous crustal thickness at different spreading rates, first no dehydration strengthening is included. Dehydration strengthening is then included and the effect of this explored. The resulting igneous crustal thickness is compared with observations.

FIGURE 3.2: (a) Plots showing temperature with streamlines of flow and viscosity with contours of the melt region, 2 and 10 % melt production within the melt region. Plots are for the models where the mantle potential temperature was 1275 and 1325 °C and the half spreading rate is $10 \, \text{mm yr}^{-1}$. Plots are of 200 by 200 km region in the top left of the model, see Figure 3.1. (b) Plot of igneous crustal thickness, (c) ratio of average velocity of material upwelling in the melt region versus the spreading rate, (d) mean temperature in the melting region and (e) % MgO composition of the melt region.

3.3.1 Model Evolution Without Strengthening and Weakening Effects of Volatiles and Melt

3.3.1.1 Variation in Mantle Temperature

Upwelling and melting within the model at the corner occurs in response to the imposed spreading. Mantle melts due to decompression as the material up-wells at the centre of extension. The melt region expands with time as the drifting continent is no longer a confining influence. The melt region however does not interact with the imposed continental lithosphere, see Figure 3.2(a). Melt depletion remains very small until the

'dry' solidus is reached at a depth of ~ 60 km, at which point melting increases rapidly and reaches a melt fraction of $> 10\,\%$. Such values are in agreement with predictions suggested in Klein et al. (1991) or Forsyth (1993). For the warmer mantle potential temperature of $1325\,^{\circ}$C a small-scale convection cell is set up, which corresponds with the slight peak in crustal thickness (Figure 3.2a and b).

As the mantle potential temperature is increased the crustal thickness produced increases (Figure 3.2b). An increase in melt production is a result of two factors. First, higher temperatures results in a much deeper on-set of melting. Second, the higher temperatures increase the thermal buoyancy, resulting in a component of active upwelling and small-scale convection that enhances melt production. The effect of the melt upon the buoyancy of the mantle is reflected in the ratio of upwelling at the ridge axis to the half spreading rate (see Figure 3.2c). Initial high upwelling is due to the slope of the pre-thinned initial condition (Figure 3.1; the validity of the pre-thinned initial condition is explored in Chapter 5). A reduction in the ratio reflects a decrease in the amount of upwelling material and ratio becomes unstable due to small-scale convection. The hotter mantle can then be seen to generate a component of small-scale convection that enhances melt production (Figures 3.2b and 3.2c).

The evolution of the rifted margin gives a depletion in FeO and TiO_2 (Figure 3.3). CaO, Al_2O_2 and SiO_2 become enriched as melting progresses, and Na_2O varies less significantly. The variations in the major elements reflect the gradual increase in melt production as rifting progresses.

3.3.1.2 Variation in Half Spreading Rate

When the spreading rate is decreased the crustal thickness is reduced. From Figure 3.4(b) the crustal thickness increases more rapidly and to greater amounts at faster spreading rates, and then settles to a steady state that is greater than that for low spreading rates. The delayed increase in crustal thickness for slower spreading rates is explained by the reduced upwelling ratio at low spreading rates.

When the convection is rapid (i.e. increased spreading rate) there is a greater solid flux through the melt region, generating more melt. This gives melt buoyancy that drives further upwelling and gives the peak in production, as is seen for half spreading rates of $50\,\mathrm{mm\,yr^{-1}}$. When the extension is slower the solid flux is less and the melt buoyancy effect is subdued and delayed as shown in the upwelling ratio in Figure 3.2(c). The impact of this reduction in upwelling can be seen in the difference in crustal thickness of around 2 km at 10 Myrs and at steady state after ~ 25 Myrs (Figure 3.5).
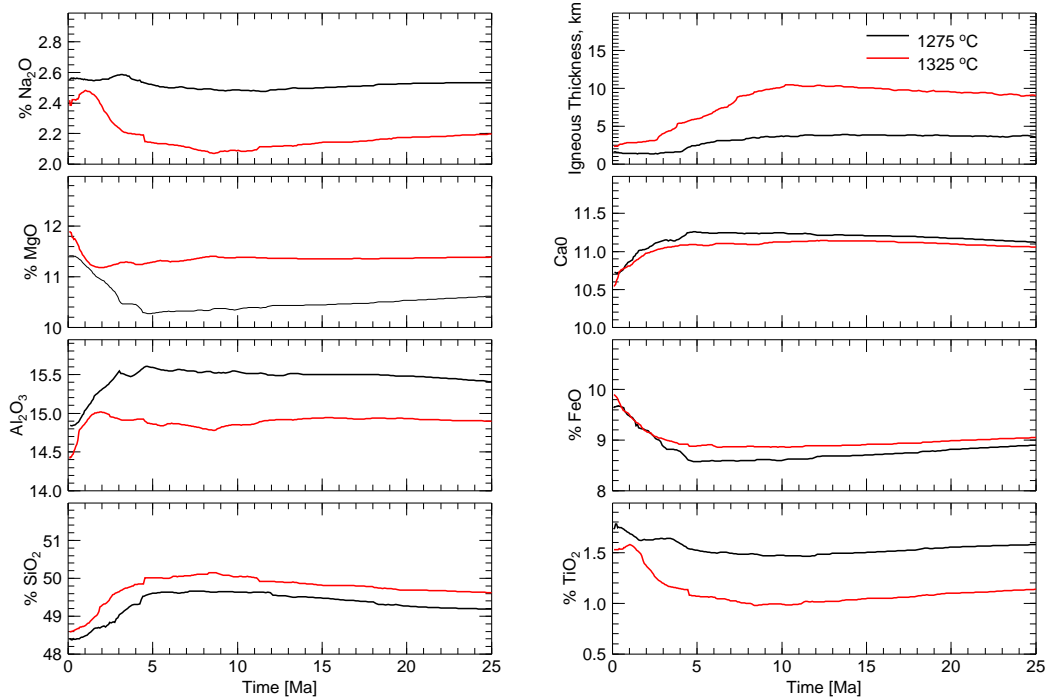
FIGURE 3.3: Primary major element composition of melt, and the igneous crustal thickness for models of rifting at a half spreading rate of $10\,\mathrm{mm\,yr^{-1}}$ and mantle temperatures of 1275 and $1325\,^{\circ}\mathrm{C}$.

Increased spreading rates have the affect of depleting the more incompatible elements such as TiO_2 and Na_2O more rapidly. Likewise SiO_2 and Al_2O_3 are more enriched during early extension for faster spreading rates (Figure 3.5). The effect of spreading rates of the composition of the melt during rifting will be explored further in Chapter 4.

3.3.2   Steady State Mid-Ocean Ridge Predictions

The major element composition and volume of melt is plotted at steady state for different spreading rates and mantle temperatures in Figure 3.6, and compared to observed crustal thickness at spreading centres. SiO_2 and FeO are insensitive to spreading rate. MgO is sensitive only to mantle temperature. This model is in general agreement with the kinematic model of sea floor spreading of Bown and White (1994) and Dean et al. (Submitted).
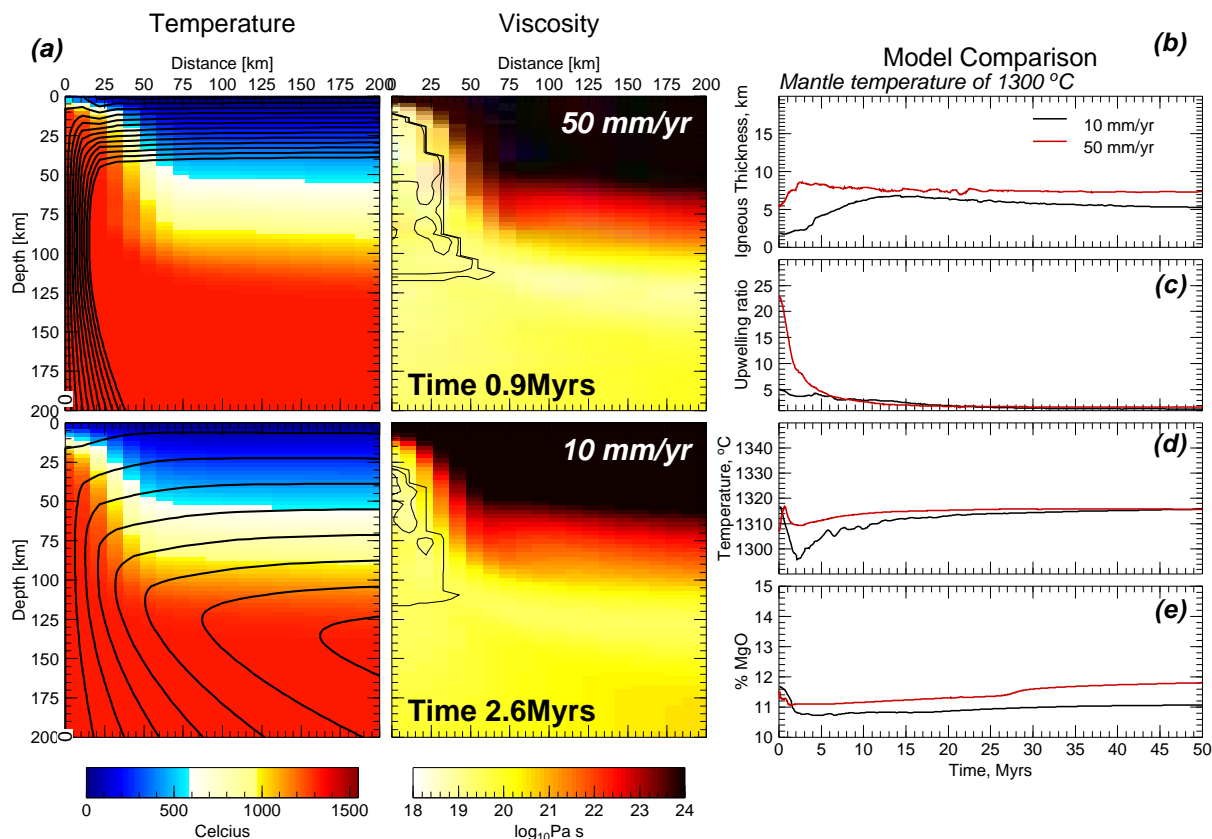
FIGURE 3.4: (a) Plots showing temperature with streamlines of flow and viscosity with contours of the melt region, 2 and 10 % melt production within the melt region. Plots are for models where the mantle potential temperature is 1325 °C and the half spreading rate is 10 and 50 mm yr^{-1}. Plots are of a 200 by 200 km region in the top left of the model, see Figure 3.1. (b) Plot of igneous thickness, (c) ratio of the average velocity of material upwelling in the melt region versus the spreading rate, (d)mean temperature in the melting region and (e) % MgO composition of the melt region.

Predictions of steady state Na$_2$O and CaO/Al$_2$O$_3$ are in range of the measured compositions from spreading centres (Klein and Langmuir, 1987). Furthermore, at fast spreading rates the iron oxide prediction is closer to measured values than the kinematic model of Bown and White (1994).

As in the models of Bown and White (1994), an increase in FeO as spreading rates are reduced is predicted. Such an increase is not observed within the observations of FeO at spreading centres (Bown and White, 1994). There are three possible reasons: first the fractionation of the FeO during the crystallisation of the melt to olivine may give measured compositions that differ from the actual melt composition. Secondly, there are real variations in the melt composition due to episodic melt generation or

Mantle temperature of 1325 ºC
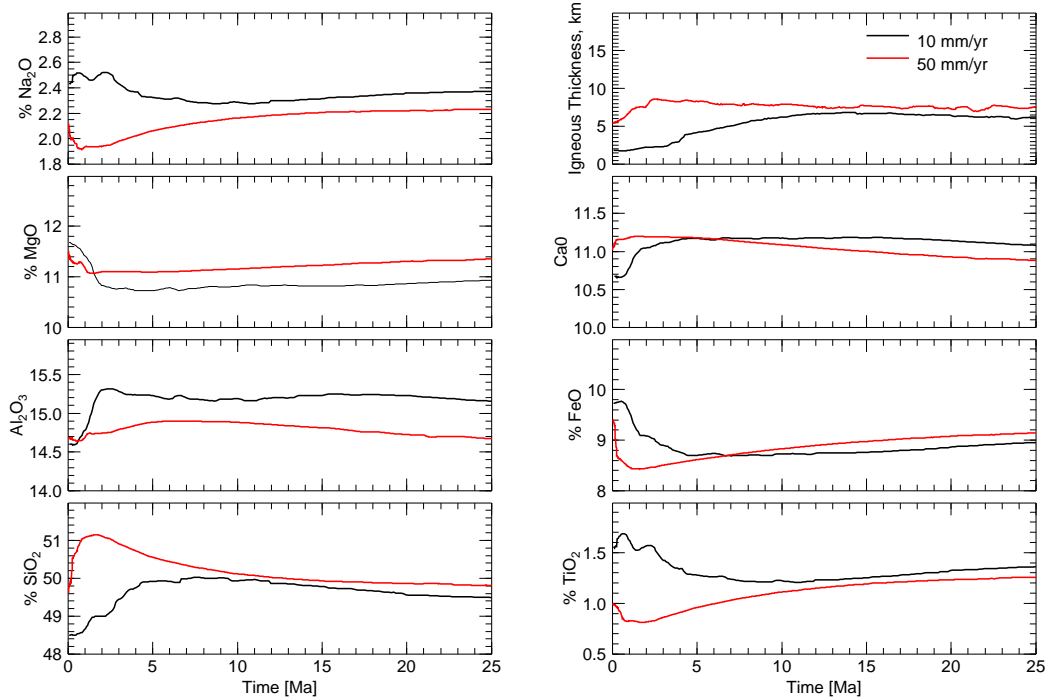
FIGURE 3.5: Primary major element composition of melt during rifting and extension when the mantle temperature is $1300\,°C$ and half spreading rates of 10 and $50\,mm\,yr^{-1}$.

melt re-equilibrium with the mantle, which are not modelled here (Bown and White, 1994). Finally, and a likely source of the discrepancy, are possible inaccuracies in the parameterisation of melt composition. Both this model and the kinematic model of Bown and White (1994) predict similar variations iron oxide composition, despite the calculation of the melt depletion being from different approaches. The only similarity is the use of the composition parameterisation of Watson and McKenzie (1991).

At very low spreading rates and elevated mantle temperatures ($\sim 1325\,°C$) the steady state crustal thickness diverges. It has been suggested that at low spreading rates, a dynamic model where melting is driven by buoyant upwelling would show proportionally more melting at shallow depths (White et al., 2001). This effect appears to require a relatively high mantle potential temperature. At high mantle temperatures convection and upwelling is more vigourous and melting initiates at greater depths. The presence of this melt gives increased mantle buoyancy, further increasing the upwelling relative to the spreading. The upwelling increases the solid flux through the melt region generating further melt and decreasing the buoyancy further providing a positive feedback to the velocity. This feedback system sets up a small-scale convection cell, which maintains the
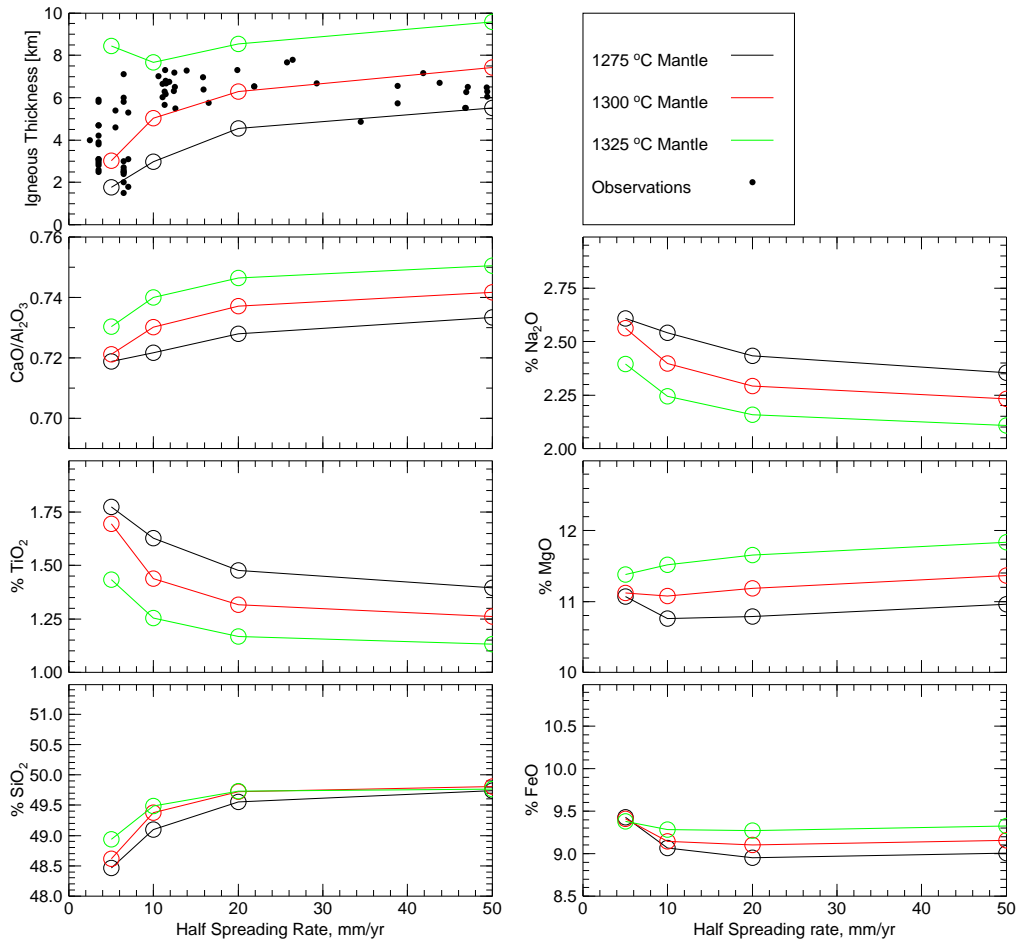
FIGURE 3.6: Plot of steady state predictions for major element melt composition and crustal thickness for increasing half spreading rates. Models are run at increasing mantle temperatures from 1275 to 1325 °C. Igneous crustal thickness predictions are compared to the data set of Bown and White (1994).

overturning of mantle material at the ridge axis (as seen in Figure 3.2). Small-scale convection such as this has been modelled previously in Scott and Stevenson (1989). Scott and Stevenson (1989) suggest that this feedback can be controlled. When the depleted material is delivered to the upper boundary and drawn laterally away by the extension, the upwelling is reduced providing negative feedback. At higher spreading rates material is pulled away from the melt region more rapidly giving stable states, however at low spreading rates and high mantle temperatures this material is not removed quickly enough and the small-scale convection cell is set up. Small-scale convection is therefore, to an extent, a factor of the assumed geometry of the lithosphere.

3.3.3 Inclusion of Dehydration Strengthening and Melt Weakening

The effect of dehydration of the mantle is included as a factor of 100 increase in the viscosity once 2 % melt has been produced. As outlined within Section 2.1.3, the strengthening multiplier χ_{H_2O} increases linearly from 1 to 10 whilst melt production is wet. Once 2 % melt is produced then the multiplier steps to 100. This is based on the observation that the viscosity of olivine aggregates reduces by a factor of 140 in the presence of water (Hirth and Kohlstedt, 1996). In this section the strengthening multiplier is applied to the models of rifting and extension of the continental lithosphere.

When the strengthening of the mantle upon dehydration is included, the flow of mantle material at shallow depths is reduced. This can be seen within Figure 3.7 as the region of increased viscosity above the 2 % melt contour at a depth of 65 km. The dehydration reduces the upwelling of material during the early evolution of the rift, reducing the concentration of MgO in the melt. The damping effect of the loss of volatiles causes the peak in crustal thickness due to small-scale convection at mantle temperature of 1325 °C, (Figure 3.2), to be eliminated (Figure 3.7).

The major element composition trends are not greatly effected by the damping (comparing Figures 3.3 and 3.8 or Figures 3.5 and 3.9). There is a slight reduction in the peak SiO_2. The sensitivity of magmatism to mantle temperature remains the same, as does the sensitivity of SiO_2 and FeO to spreading rate.

3.3.3.1 Steady State Mid-Ocean Ridge Predictions

At very slow spreading rates the igneous crustal thickness at mid-ocean ridges varies over a large range, from less than 2 km to more than 7 km (Bown and White, 1994). Geophysical models of rifting have so far been unable to reproduce this range of crustal thickness, nor the sharp transition from thin crust at ultra slow spreading centres, to normal thicknesses at slow, intermediate and fast spreading centres (White et al., 2001). That is except for the non-dynamic model of (Bown and White, 1994), where the appropriate thinning of the lithosphere was chosen to fit this transition following Spiegelman and McKenzie (1987). One hypothesis to reconcile the models with observations is that dehydration strengthening due to melting may help focus upwelling at slow rates of extension.

The addition of a strengthening factor of 100 reduces the steady state igneous thickness at slow spreading rates, especially for warmer mantle temperatures (Figure 3.10). The general agreement between model predictions and the observations is good, especially
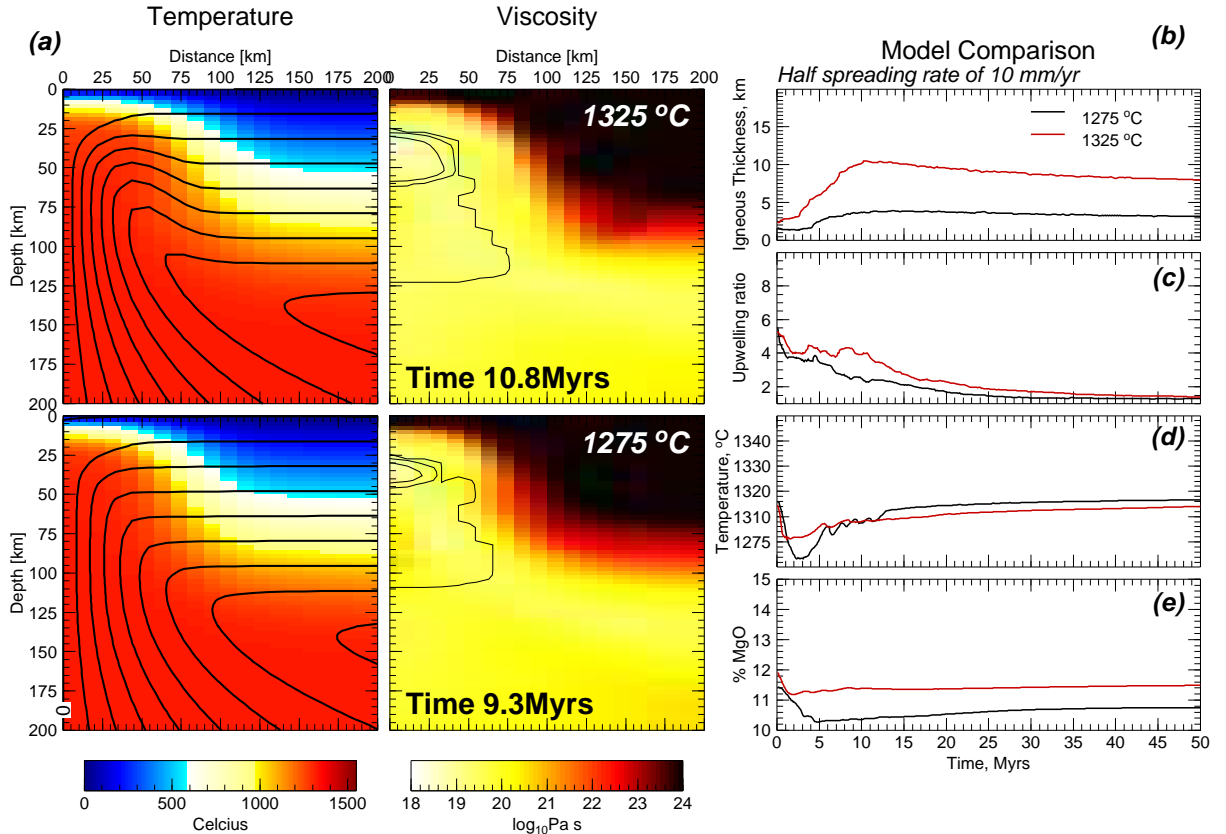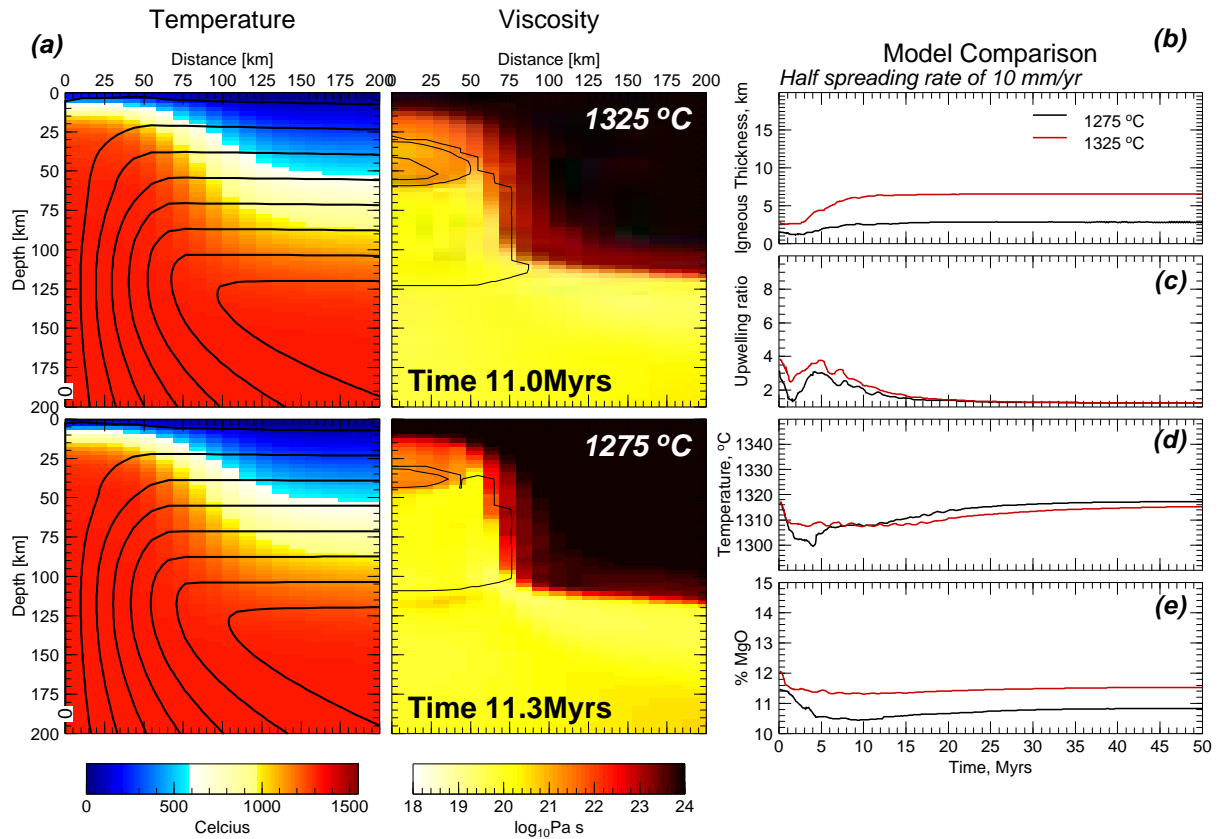
FIGURE 3.7: (a) Plots showing temperature with streamlines of flow and viscosity with contours of the melt region, 2 and 10 % melt production within the melt region. Plots are for models where the mantle potential temperature is in the top panel 1325 °C, and below mantle potential temperature is 1275 °C. The half spreading rate is 10 mm yr^{-1}. The effects of dehydration strengthening and mantle weakening included, leading to the horizontal stratification, orange colours from between 20 and 65 km depth, where 'dry' melting occurs. Plots are of a 200 by 200 km region in the top left of the model, see Figure 3.1. (b) Plot of igneous thickness, (c) ratio of the average velocity of material upwelling in the melt region versus the spreading rate, (d)mean temperature in the melting region and (e) % MgO composition of the melt region.

Half spreading rate of 10 mm/yr
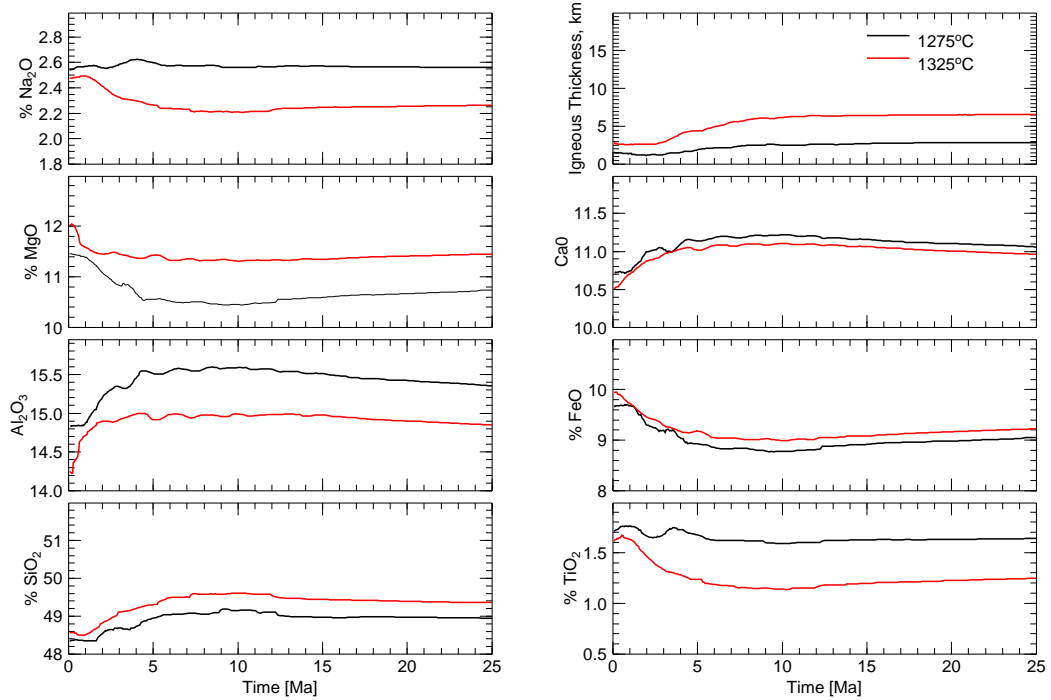
FIGURE 3.8: Primary major element composition of melt, and the igneous crustal thickness for models of rifting at a half spreading rate of $10 \, \text{mm} \, \text{yr}^{-1}$ and mantle temperatures of 1275 and 1325 °C. Dehydration strengthening is included as 2 order of magnitude increase in viscosity once 2 % melt is generated.

for a mantle temperature of between 1300 and 1325 °C. The trend of crustal thickness with spreading rate still however does not match observations at very slow spreading rates. It was hoped that a strengthening of the mantle would lead to a narrowing of the flow. The narrowing of flow has to compete with a reduction in the over all size of the melt region due to the stronger mantle. Increased viscosity due to strengthening is a double edged sword, as while the flow is stronger due to the confining effects of the more viscous mantle, the more viscous mantle also confines the melt region into a smaller area reducing the over all volume of melt that can be tapped.

3.4   Conclusions

1. The geodynamic model of the evolution of rifted margins predicts steady state crustal thickness that is close to observations, especially at half spreading rates greater than $10 \, \text{mm} \, \text{yr}^{-1}$. Using the parameterisation of Watson and McKenzie (1991), the major
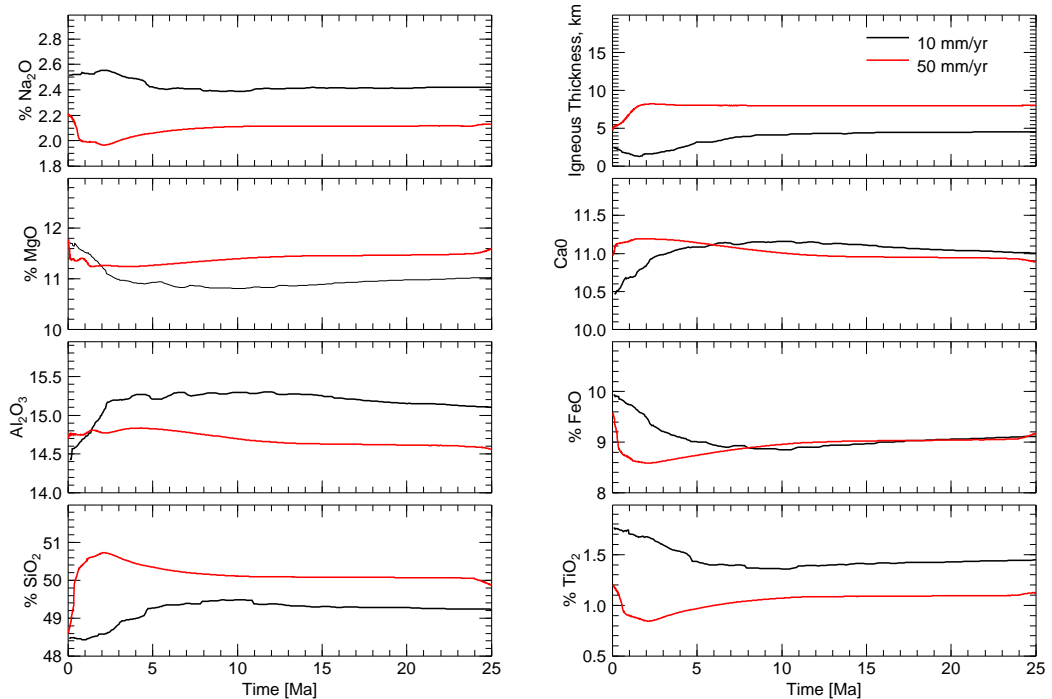
FIGURE 3.9: Primary major element composition of melt during rifting and extension when the mantle temperature is 1300 °C and half spreading rates of 10 and 50 mm yr^{-1}. Dehydration strengthening is included as 2 order of magnitude increase in viscosity once 2 % melt is generated.

element composition has been successfully calculated. The predicted composition trends of the model are in good agreement with published observations (Bown and White, 1994; White et al., 2001).

2. Predictions of steady state crustal thickness agree very well with compiled data sets of the variation of thickness with spreading rate (such as White et al., 2001). A steady state thickness of 3 km is found for crust at a mantle potential temperature of 1275 °C, 5 km for 1300 °C, and 7 km for 1325 °C at a half spreading rate of 10 mm yr^{-1} when the strengthening effect of the loss of volatiles is taken into account.

3. Dehydration strengthening of the mantle has the effect of damping small-scale convection, and reducing the predicted crustal thickness at slow spreading rates. A strengthening factor of 100 does not however cause enhanced melt production at slow spreading rates due to this damping effect.
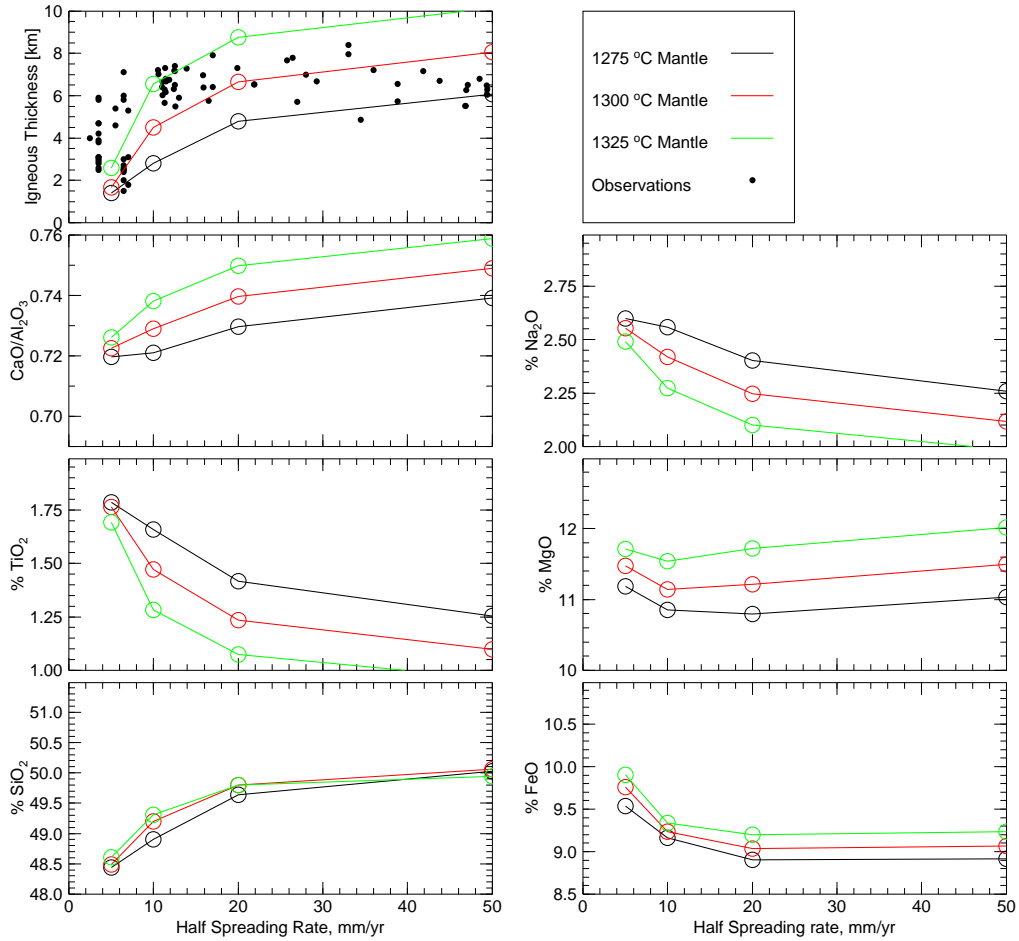
FIGURE 3.10: Plot of steady state crustal thickness and major element melt composition for model runs with a mantle temperature of 1275 to 1325 °C. The viscosity of the mantle increases by a factor of 100 due to dehydration. Models are compared to the mid-ocean ridge thickness data set of Bown and White (1994).

4. A mantle temperature of 1275 °C underestimates the igneous crustal thickness once sea-floor spreading has been set up for all but the very slow spreading rates. A mantle temperature of 1325 °C overestimates the igneous thickness at fast spreading rates. I suggest that, for an change in entropy due to melting of 250 J K^{-1} kg^{-1}, the mean mantle potential temperature beneath the oceans is between 1300 and 1325 °C.

Chapter 4

Modelling the Composition of Melts Formed During Continental Breakup of the Southeast Greenland Margin

The following Chapter is modified from Armitage et al. (2008).

Abstract

The geodynamic model of rifting is used to explore the extension and breakup of the Southeast Greenland margin. Using a crystallisation algorithm, the predicted primary melt composition is compared with mean North Atlantic mid-ocean ridge basalt (MORB). At steady state, using half spreading rates from 10 to $20 \, \text{mm} \, \text{yr}^{-1}$ and mantle potential temperatures of 1300 to $1325 \, ^\circ\text{C}$ a major element composition is predicted that is within the variation in the mean of North Atlantic MORB.

This model is applied to the Southeast Greenland margin, which has extensive coverage of seismic and ODP core data. These data have been interpreted to indicate an initial pulse of magmatism on rifting that rapidly decayed to leave oceanic crustal thickness of 8 to $11 \, \text{km}$. This pattern of melt production can be recreated by introducing an initial hot layer of asthenosphere beneath the continental lithosphere and by having a period of fast spreading during early opening. The hot layer was convected through the melt region giving a pulse of high magnesian and low silica melt during the early

rifting process. The predicted major element composition of primary melts generated are in close agreement with primary melts from the Southeast Greenland margin. The observed variations in major element composition are reproduced without a mantle source composition anomaly.

4.1 Introduction

The volume and composition of melt generated by adiabatic decompression is influenced by the potential temperature and upwelling rate of the lithosphere (McKenzie and Bickle, 1988). The breakup of continents can lead to large amounts of magmatism giving large igneous provinces such as that formed around the North Atlantic in the early Tertiary (Fowler et al., 1989; Barton and White, 1997; Hopper et al., 2003). Various models for extension and rifting have been put forward: models in which stretching and buoyancy are imposed but the velocity field is not perturbed by buoyancy, e.g. Bown and White (1994, 1995); Williamson et al. (1995); and more dynamic models, in which the flow of material is subject to internal forces due to density gradients within mantle, e.g. Scott (1992); Ito et al. (1996); Boutilier and Keen (1999); Nielsen and Hopper (2004). Here we develop a two dimensional dynamic model of rifting that includes melt composition calculations. This model will be used to explore the evolution of volcanic margins and the thermal and chemical nature of the mantle beneath such margins. We shall examine the effect of the initial temperature structure, and early spreading rates upon the evolution of the Southeast Greenland margin, which is in the distal region of the possible Iceland plume track (Holbrook et al., 2001).

4.1.1 Breakup of the North Atlantic

The breakup of the North Atlantic is thought to have been influenced by the Iceland hotspot (White and McKenzie, 1989; Holbrook et al., 2001). In this Chapter I am concerned with understanding the breakup of Southeast Greenland from the Hatton Bank off the west coast of Ireland and UK. The breakup of the North Atlantic took the following scenario: at 61 Ma a thermal plume impacted the margin and delivered warm mantle material to distal portions of the margin away from the plume impact area (Holbrook et al., 2001; Storey et al., 1998, 2007a). Warm mantle material drained along the sublithospheric topography spreading into the distal regions of the margin (Holbrook et al., 2001; Nielsen and Hopper, 2002). At breakup, between 56 and 53 Ma (Storey et al., 2007a; Cande and Kent, 1995; Berggren et al., 1995), the plume continued to feed excess melt generation and active upwelling in the proximal portion of the margin (Holbrook
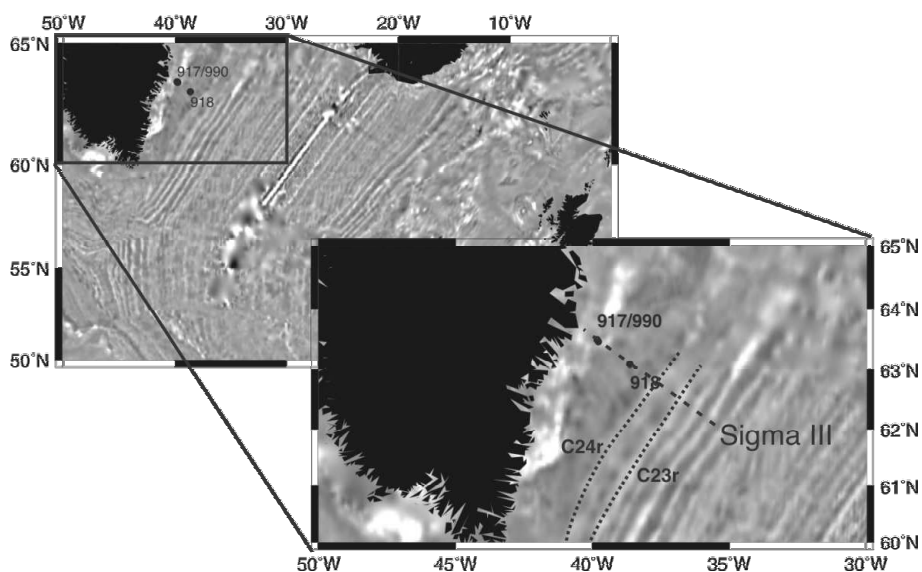
FIGURE 4.1: The North Atlantic, ODP sites 917,918 and 990 are marked off Southeast Greenland. Inset shows approximate locations of magnetic chrons C24r and C23r and the Sigma III survey line. Shading shows magnetic anomalies (Verhoef et al., 1996).

et al., 2001). In the distal regions, warm material was exhausted during breakup and the margin then evolved towards a steady state crustal thickness of between 8 and 11 km (Holbrook et al., 2001). By 45 Ma excess magmatism was confined to regions around Iceland. Therefore the anomalously thick crust observed off Southeast Greenland (Hopper et al., 2003) is possibly explained by the presence of such a hot layer beneath the lithosphere.

Studies of global mid-ocean ridge basalt (MORB) find that mean primary magma has between 10 and 15 % MgO, and that the primary magma compositions correlate with the axial depth of the ocean ridge (Klein and Langmuir, 1987). However, primary magmas from Southeast Greenland have MgO contents of up to 18 % and high FeO contents of up to 14 % (Larsen et al., 1998). Such melt compositions may be attributed to source heterogeneity associated with the ancestral Iceland plume, increased melt fraction due to the presence of a thermal anomaly, or both (Fram et al., 1998; Fitton et al., 2000).

4.1.2 Drilling off Southeast Greenland

The Ocean Drilling Program (ODP) cored the Southeast Greenland margin during legs 152 and 163 (see Figure 4.1). The transition within site 917 from thick silicic flows through a sandstone layer to units of olivine basalt and picrite marks the final stage of breakup (Larsen et al., 1994; Fitton et al., 1995). Basalts from the upper series at site 917 have not been dated although the setting of this series suggests an age of 56 Ma or

older (Larsen and Saunders, 1998; Sinton and Duncan, 1998). Basalts recovered from the upper series have high concentrations of magnesium oxide (see Table 4.1; Larsen et al., 1998) and have been inferred to be close to primary (Thy et al., 1998). It is believed that these units were rapidly erupted through a system of fissures rather than stored within magma chambers (Fitton et al., 2000). Furthermore it is suggested that such aphyric picrite with 18 % MgO would have had an eruption temperature of 1380 °C, which implies a mantle potential temperature 1500 to 1600 °C (Nisbet et al., 1993; Fitton et al., 1995).

Site 990 lies fractionally further off-shore and was also emplaced at roughly 56 Ma (Tegner and Duncan, 1999). The composition of the primary magma from unit 990-7 has been calculated (Larsen et al., 1999) by back calculating along the crystallisation liquid lines of descent and is summarised in Table 4.1. From the crystallisation calculations used to generate the primary melt it was predicted that melting began at high temperatures (1580 to 1460 °C) and there were high degrees of melting (15-21 %) (Larsen et al., 1999). The basalts sampled at site 918 were erupted when the rift had developed towards more steady rifting with more established magma reservoirs (Tegner and Duncan, 1999; Fitton et al., 2000).

4.2 Methods

4.2.1 Melt depletion and Composition

I have developed a model that first calculates the amount of melt generated during the rifting of continents and then predicts the primary composition of that melt (see Chapter 2, Sections 2.1 to 2.3.1). The modelling procedure can be broken down into two steps: First the mantle flow is calculated using a modified version of *CitCom* (Moresi and Solomatov, 1995; Nielsen and Hopper, 2004), which predicts the amount of melt generated during rifting. The amount of melt generated is sensitive primarily to the spreading rate and mantle temperature. The second step uses the fraction of melt generated, the temperature and pressure within the melt region to calculate the melt major element composition. These calculations are based on the two empirical parameterisations of Watson and McKenzie (1991), and Niu (1997), outlined below. Therefore there are three variables within this model: the initial mantle temperature structure, the spreading rate and the choice of composition parameterisation.

The two major element composition parameterisations are focused:

1. The major element composition of accumulated melt was linked to fraction of melt generated and pressure by fitting polynomial functions to large data sets from batch melting experiments (McKenzie and Bickle, 1988). Additional corrections to the iron and magnesium oxides to maintain consistency with the olivine/liquid partition coefficient were made to this parameterisation by Watson and McKenzie (1991), which I will refer to as WM91. The instantaneous melt composition, C_l, is found by the following empirical formula,

$$C_l = a = b(1 - F)^{\frac{1-D}{D}} \tag{4.1}$$

where F is the fraction of melt generated and a, b and D are estimated from a range of experimental data (see Section 2.3.1.1).

The statistical empirical approach of WM91 to generate a function for the composition of melt overestimates calcium oxide concentrations at low fractions of melting when the data is looked at qualitatively (Langmuir et al., 1992). The bulk partition coefficient for sodium oxide is also grossly over estimated, leading Langmuir et al. (1992) to suggest that the WM91 parameterisation is not much of an improvement upon more simplistic smoothed isobaric melting paths (Klein and Langmuir, 1987). However WM91 is a robust quantitative parameterisation and can be used within melting models with relative ease due to the simple polynomial relationships that relate instantaneous melt composition to the fraction and pressure of melting.

2. An alternative approach to quantifying the composition of the melt is to use the partition coefficient, D, that determines the ratio of a particular oxide within the solid and liquid parts.

$$D = \frac{C_s}{C_l} \tag{4.2}$$

C_s is the weight percent solid composition and C_l is the liquid composition. By using the melting experiments of Jaques and Green (1980); Falloon et al. (1988); Hirose and Kushiro (1993) and Baker and Stopler (1994), Niu (1997) calculates the apparent partition coefficients for the major elements as a function of temperature and degree of melting by constructing a mass balance, which is referred to as N97. Due to the lack of available data, N97 compositions at melt fractions less than 1 % and at pressures greater than 2.5 GPa are poorly constrained (Niu, 1997). For fractions of melting less than 1 % I calculate the partition coefficient assuming 1 % melt and for pressures greater than 2.5 GPa I similarly calculate the partition coefficients at 2.5 GPa.

For the N97 parameterisation the mantle source composition used is the MORB pyrolite of Falloon and Green (1987). WM91 uses empirical fits from laboratory melting experiments to derive a partitioning relation between melt composition and solid residue. Therefore both parameterisations assume a homogeneous source mantle composition.

As such any variation of composition in the primary melts generated are only a result of spreading rate and temperature.

As outlined within Section 2.3.1, these two major element composition parameterisations are incorporated within the fully dynamic rifting model *CitCom* (Moresi and Solomatov, 1995). The melting calculations follow Nielsen and Hopper (2004) using the parameterisation of Scott (1992). Melt fraction is predicted by tracing the concentration of a completely compatible element, X, through the melt region (see Appendix A). This conceptional quantity X is always positive and equals one for fertile unmelted mantle and increases as melting progresses (Scott, 1992). The composition of the solid, C_s is given by (following from Spiegelman, 1996),

$$\frac{\partial C_s}{\partial t} + \mathbf{u} \cdot \nabla C_S = \left(1 - \frac{1}{D}\right) \frac{C_s}{1 - \phi} \dot{m} \tag{4.3}$$

where $\mathbf{u}$ is the mantle flow, ϕ is the porosity and $\dot{m}$ is the melt production rate. For a completely compatible trace element, $D \to \infty$:

$$\frac{\partial X}{\partial t} + \mathbf{u} \cdot \nabla X = \frac{X}{1 - \phi} \dot{m} \tag{4.4}$$

We solve Equations 4.3 and 4.4 using a Petrov-Galerkin method for the advection (Brooks and Hughes, 1982) and then make a small perturbation to account for melting. During batch melting, $X(1 - F) = 1$ (Scott, 1992). Given that melting and advection of X is accounted for by Equation 4.4, WM91 and N97 can be implemented, as both relate the major element composition of the melt to the fraction of melt generated. The notable difference between the two is that WM91 calculates melt composition solely from the total melting, where as N97 determines melt composition from the residue and a set of partition coefficients.

This difference in methods makes WM91 simpler to implement within the dynamic model as only Equation 4.4 must be solved. However N97 requires that at each time step Equation 4.3 and 4.4 are solved. This gives the solid residue composition, and from the partition coefficient the instantaneous melt composition can be calculated. Thus the composition of the residue is tracked as melting continues. Furthermore, as this method is based on partition coefficients it should be easily adaptable for other elements, such as rare earth elements that undergo very little fractionation during crystallisation.

Following Watson and McKenzie (1991), the average composition of all the melt generated is given by the weighted average of the C_l over the melting region:

$$\overline{C} = \frac{\int \int_{melt} F C_l dx dz}{\int \int_{melt} F dx dz} \tag{4.5}$$
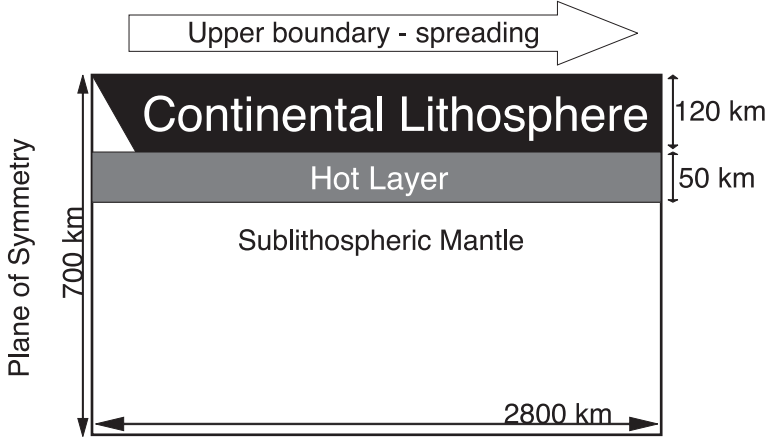
FIGURE 4.2: Initial geometry of the solution space with the sub-lithospheric hot layer. The Continental lithosphere is pre-thinned by a factor of 2 over 3 horizontal elements to ensure localisation of the initial rift.

Thus assuming all melt is instantaneously removed at some depth from the centre of extension, the composition of the melt can be calculated for the evolution of the margin at different spreading rates and mantle potential temperatures. Likewise the bulk melt fraction, F_{bulk}, is calculated as the integral,

$$F_{bulk} = \int \int_{melt} F dx dz \qquad (4.6)$$

over the melt region. The igneous crustal thickness, h_c is calculated assuming that all the melt is focused and accretes at the ridge axis following Ito et al. (1996); Nielsen and Hopper (2004),

$$h_c = \frac{2}{u_z} \frac{\rho_m}{\rho_l} \int \int_{melt} \dot{m} dx dz \qquad (4.7)$$

where ρ_m is the mantle reference density and ρ_l is the melt density.

4.2.2   Model boundary and initial conditions

The top of the 2800 km wide by 700 km deep box (shown in Figure 4.2) is driven to the right at the chosen spreading velocity. Symmetry is assumed along the edge where the ridge develops and that there is no flow of heat or material across the boundary.

Nielsen and Hopper (2004) modelled Atlantic opening with a constant spreading rate of 10 mm yr^{-1}. In this chapter, I will initially make the same assumptions as Nielsen and Hopper (2004). Then I will introduced a new two velocity conditions on the top boundary: initially fast, half spreading of 40 mm yr^{-1} for 4 Ma, followed by spreading at 10 mm yr^{-1}. This set of condition is chose as initial spreading rates were 3 to 4 times

greater than the eventual slow spreading along the Reykjanes Ridge (Hopper et al., 2003; Larsen et al., 1998). The purpose of the second set of boundary conditions is to assess if this change in spreading rate during early breakup effects melt production and chemistry.

The initial condition is as shown in Figure 4.2. Following Nielsen and Hopper (2004) the continental lithosphere is pre-thinned with a half width of ~ 25 km to control the onset of stretching. The insertion of a hot layer 50 km thick with temperature increases of 100 and 200 °C is tested. Models are set to hold a mantle potential temperature drop from the surface to the base of the model at 700 km depth. This value is set to between 1300 and 1325 °C within the following sections. The effects of dehydration strengthening and melt weakening on the viscosity of the model are included (see Nielsen and Hopper (2004) for details). Neither melt composition parameterisation accounts for the effects of wet melting on composition, so these are not included in our model. However since water is assumed to be removed by the time the melt fraction reaches 2 % any errors will be small in predicted compositions. The Rayleigh number for the initial system is set to 1.091×10^5, to give a reference mantle viscosity of 4.5×10^{20} Pa s (Nielsen and Hopper, 2002).

4.3   Results and Discussion

4.3.1   Validation of Predicted Steady State Mid-Ocean Ridge Basalt

The first step is to benchmark the model at steady state. To do so model runs are generated from mantle potential temperatures of 1300 °C to 1325 °C, and half spreading rates from $10\,\mathrm{mm\,yr^{-1}}$ to $20\,\mathrm{mm\,yr^{-1}}$ with no thermal anomaly beneath the lithosphere. This small range of spreading rates and mantle temperatures are tested as the steady state crustal thickness for such conditions is between 5 and 9 km which is representative of global mid-ocean ridge thickness.

Melt generated at a steady state mid-ocean ridge is assumed to accumulate at the ridge axis where it begins to crystallise. The crystallisation depth depends on the thermal structure, and hence the spreading rate, of the ridge. Data from the mid Atlantic indicate crystallisation pressures of ~ 200 MPa (Herzberg, 2004). To test the chemical predictions of the model, the melt chemistry produced at steady state is calculated and from this *Melts* is used to predict the MORB compositions that would be produced assuming a crystallisation pressure of 200 MPa (Ghiorso and Sack, 1995; Asimow and Ghiorso, 1998). Furthermore, a melt water composition of 0.2 % and the fayalite-magnetite-quartz redox
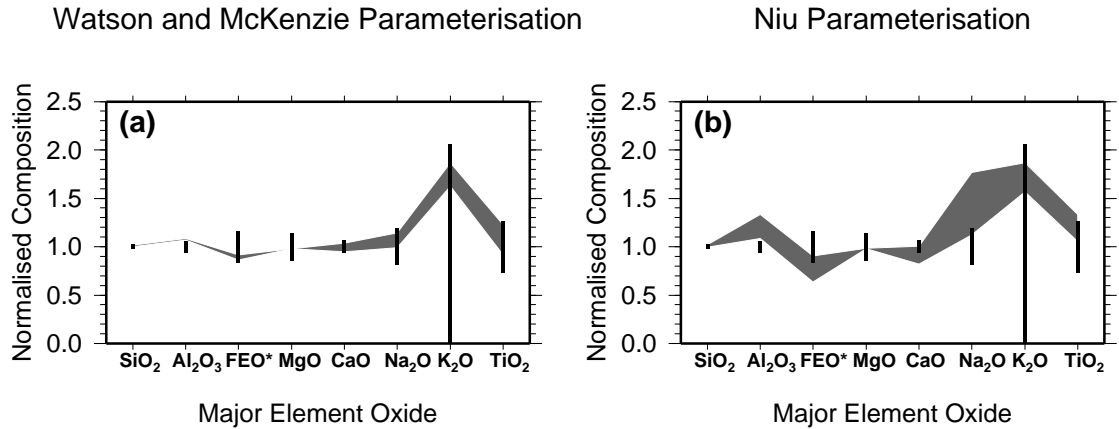
FIGURE 4.3: Full range of steady state MORB predictions for (a) WM91 and (b) N97 models run at mantle temperatures of 1300 °C and 1325 °C, and half spreading rates of 10 mm yr^{-1} and 20 mm yr^{-1}. Elements are normalised to North Atlantic MORB taken from GERM (http://earthref.org/). Bars show the variation in the north Atlantic data set.

reaction to calculate the ratio of FeO to Fe_3O_2 are assumed. Liquid lines of descent are tracked until there is 8 % MgO to match the mean for North Atlantic MORB.

The WM91 parameterisation gives predicted MORB that lies within the range of observed North Atlantic MORB for all model runs (Figure 4.3a). The N97 parameterisation does not perform so well at steady state: aluminium and sodium oxide compositions are too high and calcium oxides too low (Figure 4.3b). The poorer performance of this parameterisation is not surprising as it is based on a smaller data set. Despite these problems, both parameterisations can predict North Atlantic MORB at steady state.

4.3.2 Primary Melts from Rifting at Constant Spreading Rates

As just shown, the predicted melt composition at steady state gives a reasonable match to MORB. McKenzie et al. (2005) suggest that steady state oceanic mantle temperature is 1315 °C and that a small increase in temperature of 12.5 °C can increase crustal thickness by 1 km. Within this model, as shown by Nielsen and Hopper (2004), to generate a crustal thickness for a half spreading rate of 10 mm yr^{-1} at steady state that is close to the 8 to 11 km crustal thickness of the Reykjanes Ridge (Smallwood and White, 1998; Weir et al., 2001; Jacoby et al., 2007) requires a slightly hotter mantle potential temperature of 1325 °C. Therefore within the following analysis of the evolution of
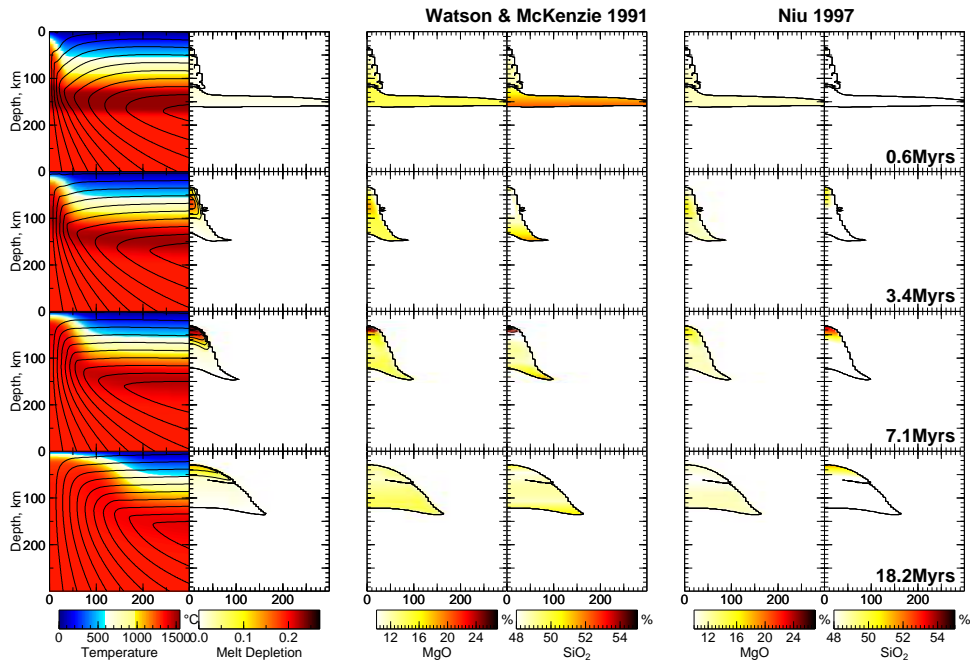
FIGURE 4.4: Temperature and flow, melt depletion, instantaneous % MgO and % SiO$_2$ composition of primary melt for WM91 (Watson and McKenzie, 1991) and N97 (Niu, 1997) parameterisation with a sub-lithospheric hot layer of 200 °C, mantle potential temperature of 1325 °C and half spreading rate of 10 mm yr^{-1}. Plots show a region of 300 × 300 km.

the Southeast Greenland margin, a mantle potential temperature of 1325 °C and a half spreading rate of 10 mm yr^{-1} is assumed.

The lithospheric mantle is thought to have been between 100 and 200 °C hotter than normal mantle when the North Atlantic opened (e.g. White and McKenzie, 1989; Larsen et al., 1999). Given this idea and following Nielsen and Hopper (2004), we have tested 100 and 200 °C hot layers as initial conditions to represent a remnant plume head that has ponded under the lithosphere. Due to the hot layer, there is initially an elongated deep layer of low melt generation (less than 1 %, see Figure 4.4). Because of its buoyancy and low viscosity the hot layer is advected through the melt region (between 2 and 8 Myrs of evolution) and the extent of melting rapidly increases, peaking at just below 30 %. Figure 4.4 also shows the instantaneous primary melt concentration of magnesium and silicon oxides for both parameterisations. We expect there to be a pressure dependance on the partitioning of iron, magnesium and silicon for both parameterisations. The deep melts should be dominated by those oxides that preferentially partition under high pressure, and this can be seen for iron and magnesium in both parameterisations (Figures 4.4, 4.5 and 4.6). It is likely however, that WM91 over estimates the concentration of
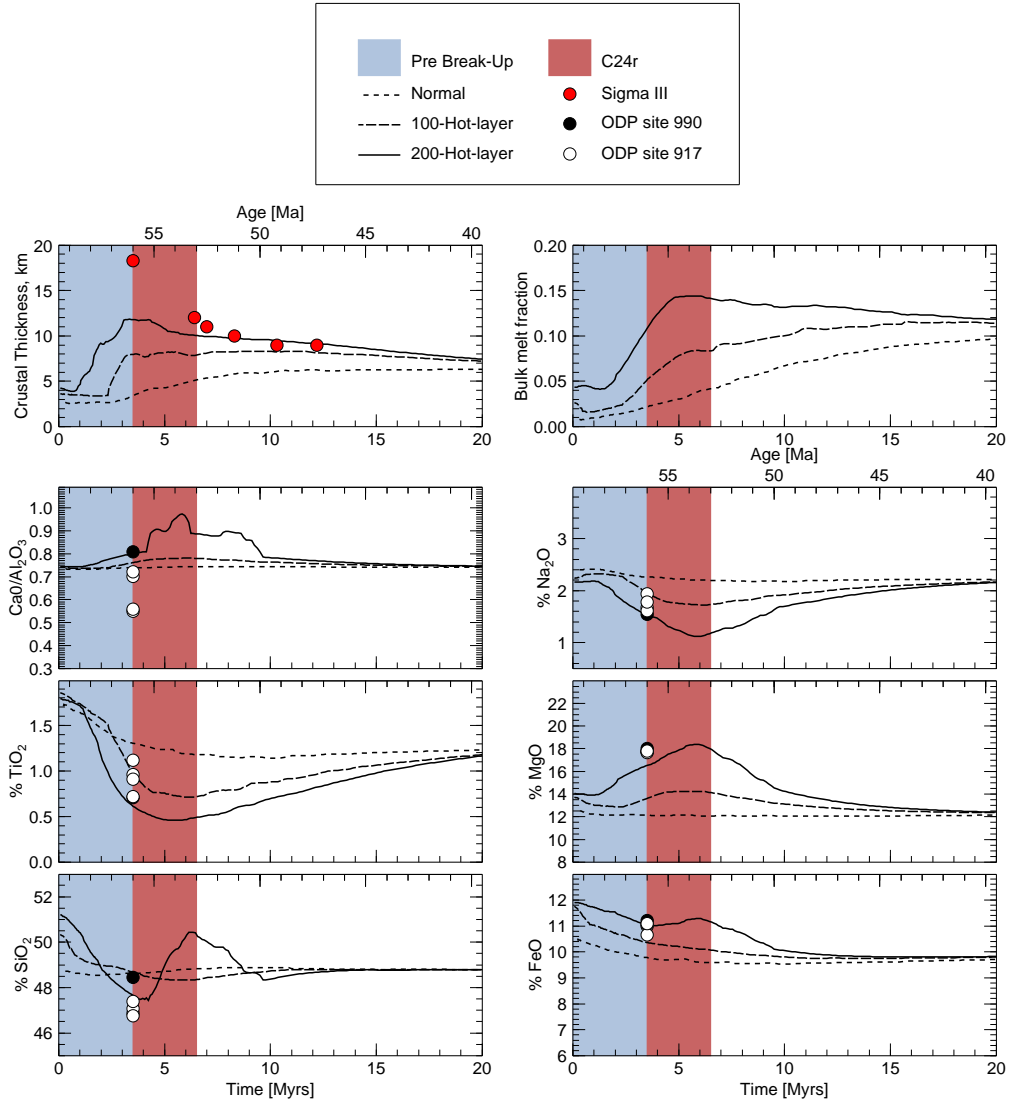
FIGURE 4.5: Evolution of predicted igneous crustal thickness, bulk melt fraction and
major element composition of primary melt for the WM91 parameterisation. The line
plots show the prediction for a model without a sublithospheric hot layer, for a 100 °C
hot layer and a 200 °C hot layer. The blue shaded area marks the time interval when
melt is initially being produced in small quantities. 'breakup' occurs when there is a
peak in melt production. The dark red shaded area represents the age rage of magnetic
anomaly C24r (Cande and Kent, 1995; Berggren et al., 1995). The red circles show
estimated crustal thickness from Holbrook et al. (2001). The black circles show primary
composition from ODP site 990, the white circles show primary composition from ODP
site 917 (see Table 4.1, Larsen et al., 1998; Thy et al., 1998; Larsen et al., 1999).

FIGURE 4.6: Evolution of predicted crustal thickness and major element composition
of primary melt for the N97 parameterisation. Other details as in Figure 4.5.

silica at depth. This is possibly due to an underestimation of the other elements at
depth, as silica concentration is calculated as 100 % minus all the other oxides.

As the hot layer is advected through the melt region the melt generation increases
significantly. The increased melt production is reflected in increased igneous crustal
thickness and bulk melt fraction. With the addition of a 200 °C hot layer the bulk
melt fraction peaks at 15 % and the igneous thickness peaks at 12 km during early
rifting (Figure 4.5). The increased melt generation alters major element composition
of the primary melt further. The two elements to consider closely are magnesium and

sodium (White and McKenzie, 1989). Magnesium oxides should become enriched within the melt with increasing melt depletion. Sodium oxides should deplete with increasing melt depletion (Klein and Langmuir, 1987). The WM91 model reproduces this basic trend well: sodium and titanium oxides are incompatible and so partition into the early melt at low melt fractions. As the melt production increases these elements take up a smaller fraction of the melt as the other more compatible oxides: magnesium, silicon and iron partition into the melt (Figure 4.5). Furthermore the WM91 parameterisation predicts the exhaustion of clinopyroxene within the regions of high melt production (melt fractions > 20 %) as predicted from melting of a fertile mantle peridotite by Herzberg and O'Hara (2002). This causes the peak in the ratio of aluminium to calcium seen during early evolution (Figure 4.5).

The high melt fractions have quite a different effect on the primary melt composition according to the N97 parameterisation (see Figure 4.6). Magnesium oxide trends are not close to what would be expected. The parameterisation fails to reproduce a significant increase in magnesium oxides that is matched with any increase in iron oxides during periods of high melt production. Sodium oxides do show a depletion as melt production increases. The calcium aluminium ratio and silicon oxide composition show an evolution that fits well with the arguments presented: an increase in the ratio when melt fractions are high. Silicon oxide composition begins low and increases with melt production as is expected (Klein and Langmuir, 1987). Finally for titanium the N97 parameterisation is in very close agreement with WM91.

The N97 model gives reasonable trends for calcium, aluminium, titanium and silicon oxide concentrations, however as a first order tool for calculating primary melt compositions, magnesium and sodium oxide trends must match reasoned geochemical arguments. It would appear that WM91 performs better than N97 from the sodium and magnesium oxide trends with melt production. A likely reason for this is that N97 miss-represents high pressure and low fraction melt due to a lack of supporting data.

The results from the both models are compared with the estimated primary melt composition during early breakup of the Southeast Greenland margin from ODP sites 917 and 990 (Fitton et al., 1998; Thy et al., 1998; Larsen et al., 1999; Figures 4.5 and 4.6). The time of peak melt production in the model is matched to the maximum igneous thickness measured by Holbrook et al. (2001). The site 917 and 990 basalts were likely erupted during the final stages of breakup at 56 Ma (Larsen and Saunders, 1998; Fitton et al., 2000). Given these observations the estimated primary compositions from ODP sites 917 and 990 (see Table 4.1) at 56 Ma, are plotted to match peak production.

TABLE 4.1: Measured and calculated primary melt compositions from ODP leg 152, site 917 and ODP leg 163, site 990

Site - unit	SiO_2	TiO	Al_2O_3	FeO	MgO	CaO	Na_2O	K_2O
917 - 14	46.77	0.72	14.30	10.65	17.67	7.86	1.61	0.06
917 - 16	47.38	0.91	13.09	11.09	17.80	7.31	1.78	0.23
Calculated								
917 - 11R4	46.88	0.96	12.40	11.00	17.76	8.71	1.67	0.17
917 - 17	47.81	0.90	13.93	9.68	15.31	9.52	2.12	0.31
990 - 7	48.45	0.71	10.89	11.21	18.01	8.88	1.54	0.08

Units 917-14 and 917-16 from Larsen et al. (1998), 11R4 and 917-17 are estimated by Thy et al. (1998); unit 990-7 primary composition was estimated by Larsen et al. (1999).

For all oxides except calcium and aluminium, the WM91 model with the inclusion of a hot layer predicts a composition that is in closer agreement than a model without the hot layer, although the maximum igneous thickness is underpredicted (see Figure 4.5). The result from the N97 model is perhaps in better agreement with predicted primary melt for the calcium aluminium ratio and silicon oxide, but for iron, and more importantly magnesium, the parameterisation gives results that are quite inaccurate. Given these inaccuracies and the poorer agreement of the N97 model with North Atlantic MORB at steady state, the WM91 parameterisation is therefore more suitable for modelling the South East Greenland margin.

4.3.3   Prediction of Southeast Greenland Basalt Compositions

ODP leg 152 site 918 sampled mildly altered basalts from the seaward dipping reflector series (SDRS) off Southeast Greenland (Fitton et al., 1998; Hopper et al., 2003). Site 918 also penetrated a younger iron and titanium oxide rich sill, possibly emplaced by an off axis volcano (Fitton et al., 1998; Larsen et al., 1998). The basalt from the SDRS is dated at 54 Ma (Tegner and Duncan, 1999) therefore it was emplaced soon after sea floor spreading had begun. Here I do not wish to get into a debate on the crystallisation processes that take place within the evolving Southeast Greenland margin. I am however aware that it would be ideal to validate our model results against further rock samples. Rather than attempt to predict primary melts from the observed compositions, the script driven front end to *Melts*: *Adiabat_1ph* (Smith and Asimow, 2005) has been used to crystallise our predicted primary composition for this site.
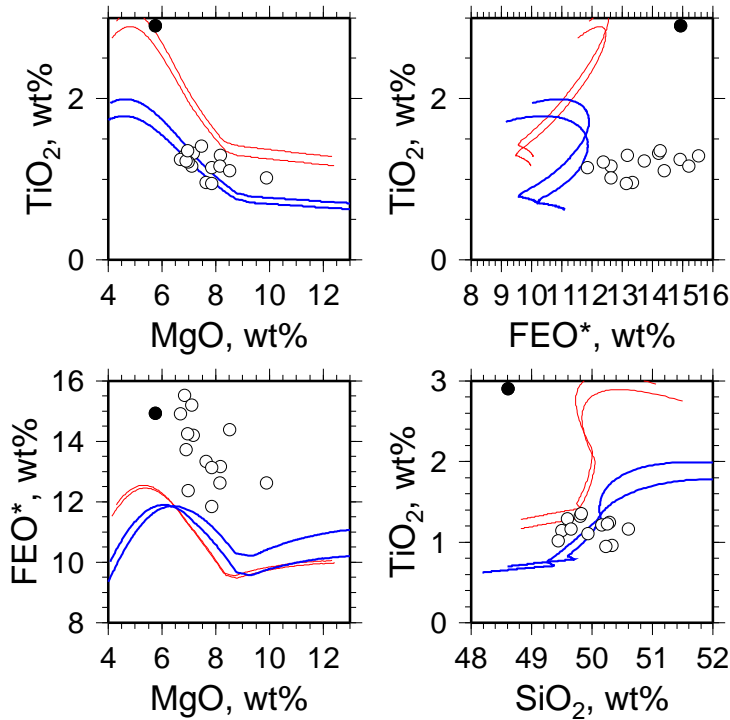
FIGURE 4.7: Element ratios for magnesium, titanium, iron and silicon oxides. Plotted are the liquid lines of descent, red lines from steady state primary melts that were batch crystallised isobarically assuming magma pools at 200 MPa. Blue lines are from the peak magnesian primary melts similarly crystallised at 200 MPa, from 5 and 10 Myrs model time (54.5 Ma and 49.5 Ma respectively). Open circles show seaward dipping reflector series (SDRS) composition data from ODP leg 152, site 918, the black circle shows the composition for the younger sill at site 918 (Larsen et al., 1998).

Atlantic MORB crystallises at pressures of around 200 MPa (Herzberg, 2004). Assuming isobaric batch crystallisation within pooled melt at that pressure, liquid lines of descent for crystallisation of primary melts generated during breakup are plotted in Figure 4.7. A comparison of the simple liquid lines of descent is made with the SDRS sampled at ODP site 918. I find that the low titanium, high magnesium primary melt, when crystallised, can account for the titanium magnesium ratio seen in the SDRS. Furthermore when younger steady state primary melt is crystallised, basalts with a titanium magnesium ratio representative of the sill basalt are generated.

The crystallisation path chosen has been less successful at predicting other major element ratios, although it is not far off for some elements such as silicon and iron oxides (see Figure 4.7). This is likely due to the liquid line of descent being more complicated than the simple isobaric approach taken here. Given that the primary melts we generate are picritic and are generated at depths of up to 100 km, there may be some significant

crystallisation en route to magma pools and/or fractures. There will also be mixing and crystallisation within magma pools, and further crystallisation and interaction with rock upon eruption. Given all the possible scenarios it is encouraging that major element compositions are generated that are close to the basalts erupted soon after breakup.

4.3.4   Primary Melts from Rifting at Variable Spreading Rates

Sea floor spreading rates are not constant. When the Southeast Greenland margin opened it did so at a faster spreading rate of around $\sim 40\,\mathrm{mm\,yr^{-1}}$ for approximately $4\,\mathrm{Myr}$ and then spreading settled to its current rate of around $10\,\mathrm{mm\,yr^{-1}}$. This simplification of the extension history of the opening of the margin is based on two sources. From the SIGMA III survey if it is assumed that the continent-ocean boundary (COB) forms at 56 Ma and everything farther west is erupted on continental crust, from the COB to Anomaly C24n is a little more than $100\,\mathrm{km}$ or about $33\,\mathrm{mm\,yr^{-1}}$ on average (Hopper et al., 2003). Larsen and Saunders (1998) suggest a slightly higher $44\,\mathrm{mm\,yr^{-1}}$ peak half spreading rate that abates to $11\,\mathrm{mm\,yr^{-1}}$ based on the interpretation of magnetic anomalies and argon-argon ages (Larsen et al., 1994; Sinton and Duncan, 1998).

Using the WM91 parameterisation I have modelled the rifting of the Southeast Greenland margin using a step change in spreading rate. It can be clearly seen that if a sublithospheric hot layer of $200\,^{\circ}\mathrm{C}$ is introduced, then the crustal thickness measured by Holbrook et al. (2001) can be recreated with a high degree of accuracy if we match peak volume with the opening of the rift. Equally, the duration, $\sim 1\,\mathrm{Myrs}$, of peak melt production matches very closely the duration of peak magma productivity estimated from Greenland - Faeroes lavas (Storey et al., 2007b). Previous models have attempted to explain thick igneous crusts by purely thermal anomalies (e.g. White and McKenzie, 1989; Boutilier and Keen, 1999; Nielsen and Hopper, 2004; Figure 4.5); it is found that in order to recreate the crustal thickness off South East Greenland initial fast spreading is required in addition to a thermal anomaly.

From Figure 4.8, composition variations may be better predicted by a slightly cooler hot layer than is required to generate the igneous crustal thickness. A $100\,^{\circ}\mathrm{C}$ hot layer predicts primary MORB compositions that are close for all major elements with the exception of the calcium aluminium ratio and the silica concentration. Inclusion of a $200\,^{\circ}\mathrm{C}$ hot layer tends to over-predict the magnesium concentration of primary melt with a very high peak in magnesium oxides. The increased spreading rate during early rifting causes increased upwelling and so even greater melting rates than when the spreading is only $10\,\mathrm{mm\,yr^{-1}}$. Thus the trends seen in Figure 4.5 are exaggerated as there is more melt present, with the bulk melt fraction exceeding $25\,\%$.
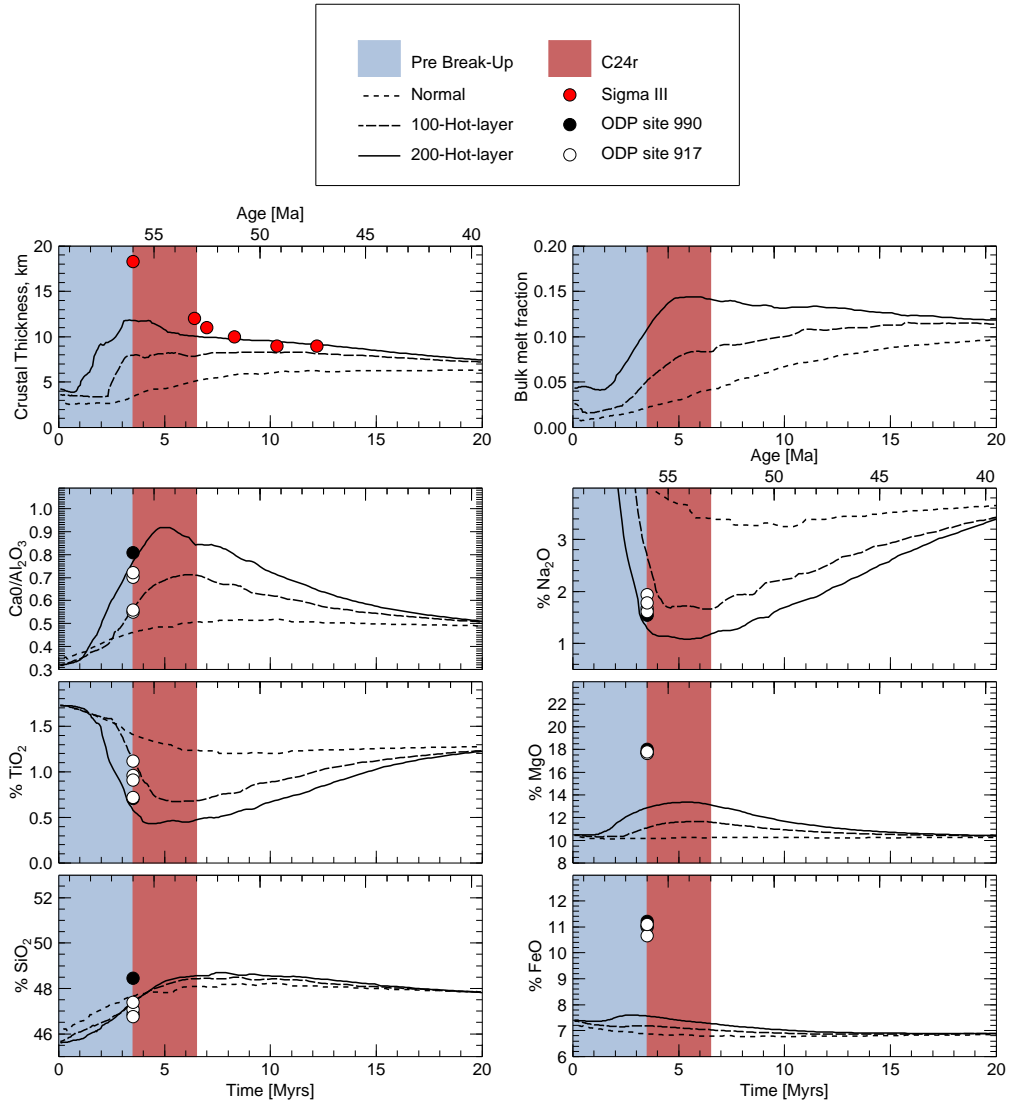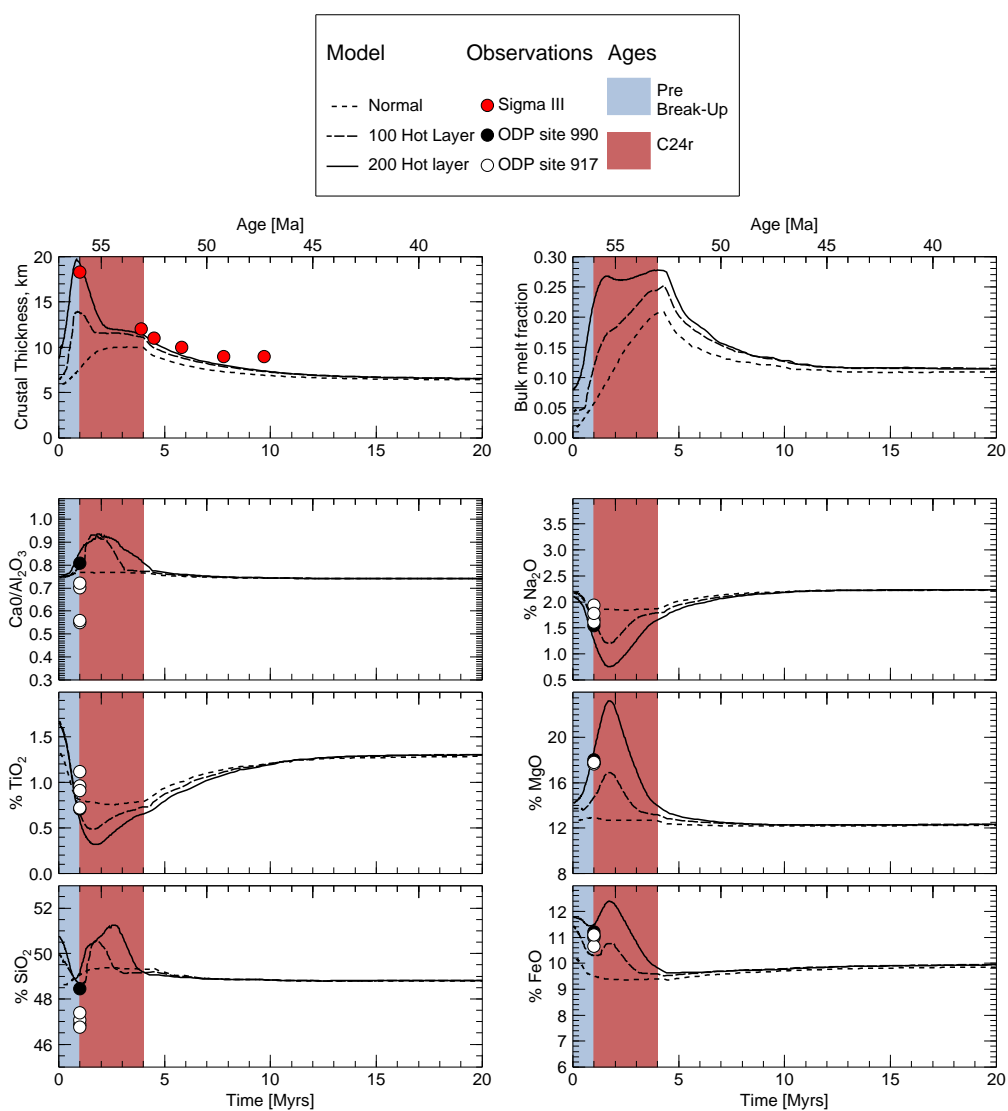
FIGURE 4.8: Plot of predicted crustal thickness and major element composition of primary melt for the WM91 parameterisation with a variable spreading rate of $40 \, \mathrm{mm \, yr^{-1}}$ for the first $4 \, \mathrm{Ma}$ of evolution followed by constant spreading at $10 \, \mathrm{mm \, yr^{-1}}$. Other details as in Figure 4.5.

Even if the major element composition is not completely recreated, as clearly the case for silicon oxide concentrations (Figure 4.8), a strong geochemical signature within the primary melt has been recreated that following crystallisation can generate compositions like that of Southeast Greenland MORB (Figure 4.7). It is generally believed that the mantle material that generated the North Atlantic igneous province can be traced back to an Iceland plume signature, e.g. Fitton et al. (1997). I have shown in this section, and for when there is no variation in spreading rate, that no anomalous mantle source composition is required to generate the anomalous major element composition of the primary melt. The generation of thick igneous crust upon breakup requires a thermal anomaly. This thermal anomaly is likely a layer of hotter mantle that may be from the lateral spreading of a thermal plume. This is consistant with active upwelling and lateral channelling of hot asthenosphere along the Southeast Greenland margin during breakup (Nielsen and Hopper, 2004; Holbrook et al., 2001; Nielsen and Hopper, 2002; Tegner et al., 1998).

4.4 Conclusions

I set out to study two variables within the rift evolution of the Southeast Greenland margin: firstly, the effect that initial temperature structure has on melt production and melt composition; and secondly, the effect of initial spreading rates on melt production and composition. In doing so I have produced a robust model that can generate North Atlantic MORB at steady state and match the igneous thickness of the Reykjanes Ridge, whilst generating a pulse of picritic, thick igneous crust during early rifting.

To generate the major element composition of primary melts that closely match the expected composition of primary melts in the distal field of the possible Iceland plume at the Southeast Greenland margin (ODP sites 917,918 and 990) has not required a compositional Iceland plume source signature. Rather it is found that the presence of an exhaustible sublithospheric hot layer during continental breakup can account for the region of thickened crust off shore Southeast Greenland. Importantly, when coupled with a pulse of fast extension, such a layer can also account for the observed picritic composition of primary melts.

This analysis does not address the origin of such a hot layer, however its presence is consistant with the lateral movement of a thermal plume based under Iceland (Holbrook et al., 2001). This thermal anomaly migrated south prior to the breakup of the North Atlantic, giving the observed volumes and picritic compositions of the oceanic crust off Southeast Greenland.

Chapter 5

Lithospheric Controls on Melt Production During Continental Breakup at Slow Rates of Extension: Application to the North Atlantic

Abstract

It is typically assumed that extension and rifting of the lithosphere above a hot astheno-sphere produces excessive volcanism. Such an assertion does not hold when the rates of extension are slow. Here I present results of numerical simulations of the extension and rifting of normal lithosphere above a thermal anomaly. I find that unless the lithosphere has undergone some extension prior to rifting, then the thermal anomaly cools signifi-cantly due the heat conduction. The result is that when mantle wells upwards due to extension of the lithosphere, it no longer increases melt production.

Therefore, to model the formation of volcanic rifted margins, the pre-rift conditions should be carefully considered. It is found that the series of extensional events prior to the formation of the Southeast Greenland and Hatton Bank margins influence mag-amtism during breakup. The extension that led to the Hatton-Rockall Basin and a pre-rift sedimentary basin off the Southeast Greenland margin thinned the lithosphere

prior to the arrival of the probable thermal anomaly. This thinnig was sufficient to enhance upwelling leading to excessive volcanism off the Southeast Greenland and Hatton Bank margins.

5.1 Introduction

Previous kinematic and dynamic models of continental rifting and associated melt production tend to consider a relatively simple rifting history (for example Nielsen and Hopper, 2004; Boutilier and Keen, 1999; Bown and White, 1995). However the history of many regions is more complicated, for example multiple phases of rifting in one place or a failed rifting event followed by a jump to a nearby location where eventual breakup occurs. Some pre-thinning of the lithosphere is often assumed when modelling extension, to encourage small scale convection and focus the melting at the ridge axis (for example Nielsen and Hopper, 2004; Boutilier and Keen, 1999). Nielsen and Hopper (2004) suggested that the presence of such a numerical device makes little difference when there is no thermal anomaly present. Here the impact of a pre-thinned region on the development of a rift above a mantle thermal anomaly will be explored. The effect of rift history of the evolution of a successful rift will be assessed and the results will be applied to the complex rifting history of the North Atlantic.

5.2 Methods

The model space is a region 2800 km long by 700 km deep of upper lithosphere and mantle. Mantle potential temperature is chosen to be 1325 °C such that the crustal thickness is 8-11 km, consistant with the North Atlantic (Armitage et al., 2008; Nielsen and Hopper, 2004). Boundary conditions are of free slip except at the top where spreading is imposed, and of no flow across the boundary. The bottom and side boundaries are kept far from the melting region to minimise the impact of these boundary conditions on the evolving system. A modified version of *CitCom* (Armitage et al., 2008; Nielsen and Hopper, 2004; Moresi and Solomatov, 1995) is used.

Models are set up with a 125 km thick, buoyant and cool lithosphere, with a 50 km thick 200 °C thermal anomaly below (Figure 5.1). The thermal anomaly is included to simulate an exhaustible layer of hot mantle that generates the enhanced breakup magmatism as seen off the Southeast coast of Greenland, the Vøring Plateau, Hatton Bank and the Edoras Bank (White et al., 2008; Voss and Jokat, 2007; Mjelde et al.,
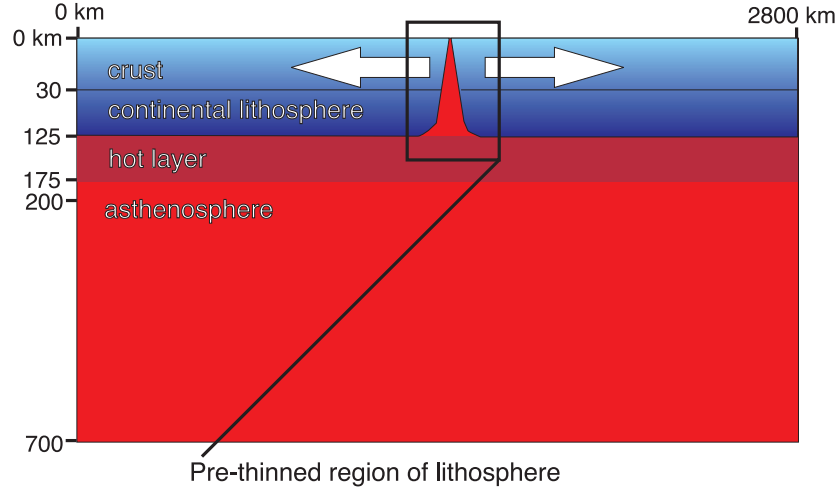
FIGURE 5.1: Diagram of model space showing the thermally and rheologically defined 125 km thick lithosphere with the option of imposing pre-thinning at the centre of extension as an initial condition. Finally there is 50 km thick thermal anomaly below.

2005; Holbrook et al., 2001; Barton and White, 1997). The lithosphere is also depleted by the factor X as defined by Scott (1992),

$$X(1 - F) = 1 \tag{5.1}$$

where F is the melt fraction (Plank et al., 1995). Thus if the material is fertile un-melted mantle, X is unity and increases as the mantle becomes increasingly depleted. Variation in X by advection and melting is modelled following Scott (1992),

$$\frac{dX}{dt} + \mathbf{u} \cdot \nabla X = \frac{X}{1 - \phi} \dot{m} \tag{5.2}$$

where $\mathbf{u}$ is the mantle velocity calculated from solving the combined Stokes and energy equations for a non-Newtonian fluid (Moresi and Solomatov, 1995), ϕ is the melt porosity and $\dot{m}$ is the melt production rate.

To calculate the melt production rate, a solidus, T_s must be defined. Normally the solidus is defined as a function of depth (*e.g.* McKenzie and Bickle, 1988). However here it is a function of depth, and depletion (X),

$$T_s^{dry} = T_{s0} + z \left(\left(\frac{\partial T_s}{\partial z} \right)_X - \left(\frac{\partial T}{\partial z} \right)_S \right) + \left(\frac{\partial T_s}{\partial X} \right)_z (X - 1) \tag{5.3}$$

The dependence on depletion adjusts the solidus as melting continues. The depth and depletion derivatives, $(dT_s/dz)_X$ and $(dT_s/dX)_z$, of the solidus are constant and equal to $3.4 \times 10^{-3}\,\mathrm{K\,m^{-1}}$ and $440\,\mathrm{K}$ respectively (Scott, 1992). Water and other volatiles,

such as CO_2, are known to weaken the mantle (e.g. Dasgupta et al., 2007; Hirth and Kohlstedt, 1996). As the mantle rock rises and melts by decompression these volatiles are preferentially partitioned into the melt. Volatiles are completely stripped out after 2 % melting (Hirth and Kohlstedt, 1996). Melting beyond 2 % is then 'dry', as all the volatiles have left the solid. I assume wet melting occurs until 2 % of melting has occurred (*i.e.* while $X < 1.02$; Braun et al., 2000). The wet solidus is defined as being an amount below the dry solidus following Braun et al. (2000):

$$T_s^{wet} = T_s^{dry} - 200 \left(\frac{1.02 - X}{0.02} \right) \tag{5.4}$$

The parametrisation of Niu (1997) is chosen to calculate the melt major element primary composition. The Niu (1997) parameterisation does have its limitations at low melt fractions and at high pressures (see Chapter 4). Yet this parameterisation can recreate MORB reasonably and it can track the depletion of the mantle as melting progresses. This is desirable as here I am interested in understanding the consequences of multiphase rifting events on melt production and chemistry. Although the melting characteristics include wet melt production, the composition parametrisation does not. Since water is assumed to be removed by the time the melt fraction reaches 2 % any errors will be small in predicted compositions.

Previous modelling work included pre-thinned regions to focus the position of rifting within the model. In the first section I assess the effect of this assumption in both cases: with and without a thermal anomaly. I will then test the effect of tectonic history on melt production and distribution by varying the extension rate, the duration of pre-thinning event and age of a failed rifting event.

5.3   Results and Discussion

I begin with simple simulations where only half of the spreading centre is modelled, with a mirror boundary down the centre of extension. Such a simplification to the model is acceptable provided that the evolving ridge is symmetric about the centre of extension. Five cases of extension are considered: *Case 1* has no thermal anomaly and no necking region imposed. This is the base model against which comparisons will be made. *Case 2* has a 200 °C, 50 km thick hot layer beneath the 125 km thick lithosphere, but still no necking region imposed. *Case 3* increases the thickness of the hot layer to 100 km keeping the temperature the same. *Case 4* has no thermal anomaly but does include a necking region, and *Case 5* is as case 2 but with a necking region. First cases 1, 2

and 3 are compared. Then I shall impose the necking region and compare cases 4 and 5, finally making some general comments of the difference between all four cases.

I have chosen these five simplified studies as I believe they are broadly representative of reasonable parameters for a thermal anomaly that would give the voluminous magmatism seen at the North Atlantic. The thermal anomaly associated with the North Atlantic igneous province is suggested to be in the range of 50 to 250 °C (Holbrook et al., 2001; White and McKenzie, 1989). Furthermore, away from the centre of the system this thermal anomaly is likely to be exhaustible (Armitage et al., 2008; Nielsen and Hopper, 2004) and by increasing the thickness I can test how quickly or slowly the anomaly must be exhausted within a realistic rifting simulation. In this phase of the study the goal is less to replicate the observed magmatism than to test the physics of the model simulations and to validate, or not, the use of a pre-thinned lithosphere as an initial condition within realistic models of rifting.

5.3.1 Models With no Necking Region: Cases 1, 2 and 3

Case 1 is a model representing background stretching with no pre-thinning, flat lithosphere, and no thermal anomalies. Rifting of the lithosphere under these conditions gives a margin that evolves through a gradual increase in oceanic crustal thickness, with a gradual depletion in titanium, sodium and little to no variation in magnesium oxides (Figure 5.2). This reflects low melt fractions within the melt region. Increased volumes of material arise from the expansion of the melt region only, as the melt region evolves to the steady state triangular region as expected under a mid-ocean ridge. Addition of a 200 °C thermal anomaly within the model of rifting (case 2) has the effect of increasing the igneous crustal thickness and making the continent to ocean transition much more rapid (Figure 5.2).

The thermal anomaly must be advected to shallower regions if it is to influence melt generation; this hot layer is however losing heat by conduction to the cooler surroundings. Thus for the hot layer to give enhanced melt production, it must rise fast enough to avoid cooling significantly. For this to occur the continental lithosphere must extend and become thinner. Yet at slow spreading rates, the extension and thinning of the lithosphere is not sufficient to draw the thermal anomaly into the melt region (see Figure 5.3). At the faster spreading rates thinning of the lithosphere is sufficient to bring the thermal anomaly into the melt region and produce significant excess melt production.

The peak in melt production, reflected in igneous thickness, at fast spreading rates is an effect of the hot layer in this case: FeO and MgO enrichment reflect high melt fractions.
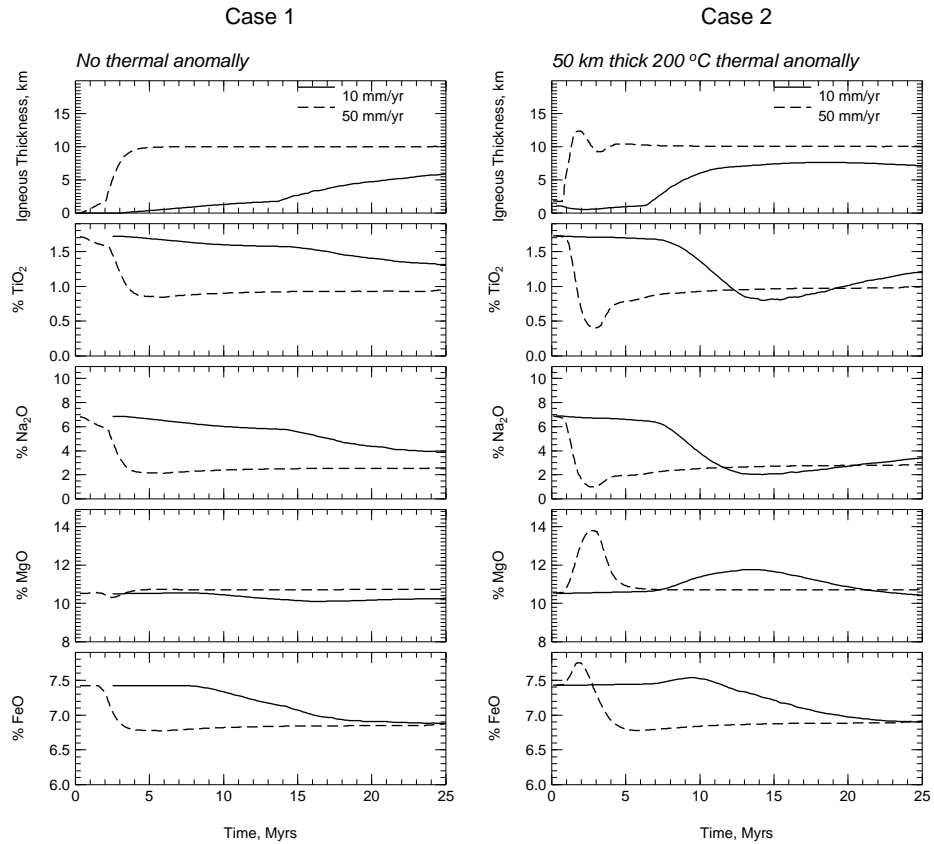
FIGURE 5.2: Igneous crustal thickness and selected major element composition of melt for the two initial conditions: *Case 1*, where the lithosphere is a flat layer with no thinned regions and no thermal anomaly beneath, and *Case 2*, where a 50 km thick 200 °C thermal anomaly exists beneath the flat lithosphere. Half spreading rate is increased from 10 to 50 mm yr^{-1}.

Thickened crust upon breakup is a reflection of the size of the melt region and of high melt fractions within the melting region. In the fast spreading case FeO concentrations peak due to the formation of deep melts, then as the thermal anomaly rises the MgO concentration peaks reflecting high melt fractions (Figure 5.2). Peaks are also observed in the model of slow extension, but diminished and much delayed.

By increasing the thickness of the thermal anomaly to 100 km (Case 3), the hot layer is not exhausted as fast as the 50 km anomaly (Figure 5.3). Therefore, less thinning of the continental lithosphere is required to sufficiently melt the mantle. An increase of hot layer thickness has the effect of introducing a sustained peak in igneous thickness and upwelling at all spreading rates. The thicker thermal anomaly broadens the region of lithosphere thinning and so slightly reduces the velocity of material upwelling within the melting region. The peak in melt production however lasts too long when the thermal
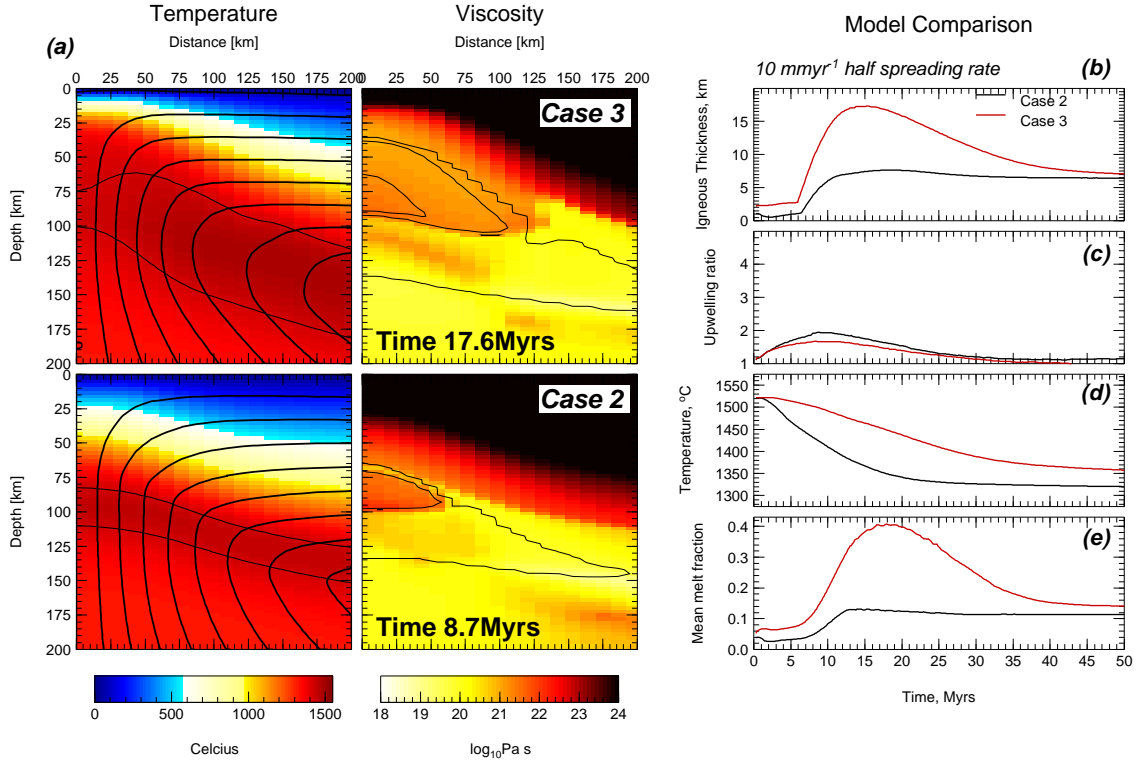
FIGURE 5.3: A comparison of *Case 2* with *Case 3*, where the thickness of the 200 °C thermal anomaly is increased from 50 km to 100 km. (a) in these four panels are plots of temperature and flow of the mantle; and viscosity and contours of 0, 2 and 10 % melt production. These properties are plotted for a 200 by 200 km region at the centre of extension. The ages chosen are that of peak melt generation for each model. On the right are comparisons of: (b) igneous crustal thickness; (c) ratio of the average upwelling velocity within the melting region against the half spreading rate; (d) mean mantle temperature within the melting region; and (e) mean melt fraction within the melt region.

anomaly is 100 km thick: with the hot layer providing excess melting for up to 30 Myrs (Figure 5.3). Such a sustained period of excess production is not seen at rifted margins. The models indicate that the presence of a thermal anomaly alone is insufficient to generate high syn-rift melt thicknesses at slow spreading rates. This is because the thermal anomaly cools before it is delivered to the melting region.

5.3.2   Models With an Imposed Necking Region: Cases 4 and 5

Within the final sets of simulations, a narrow pre-thinned region at the centre of extension has been included as an initial condition. The hot layer is not assumed to have
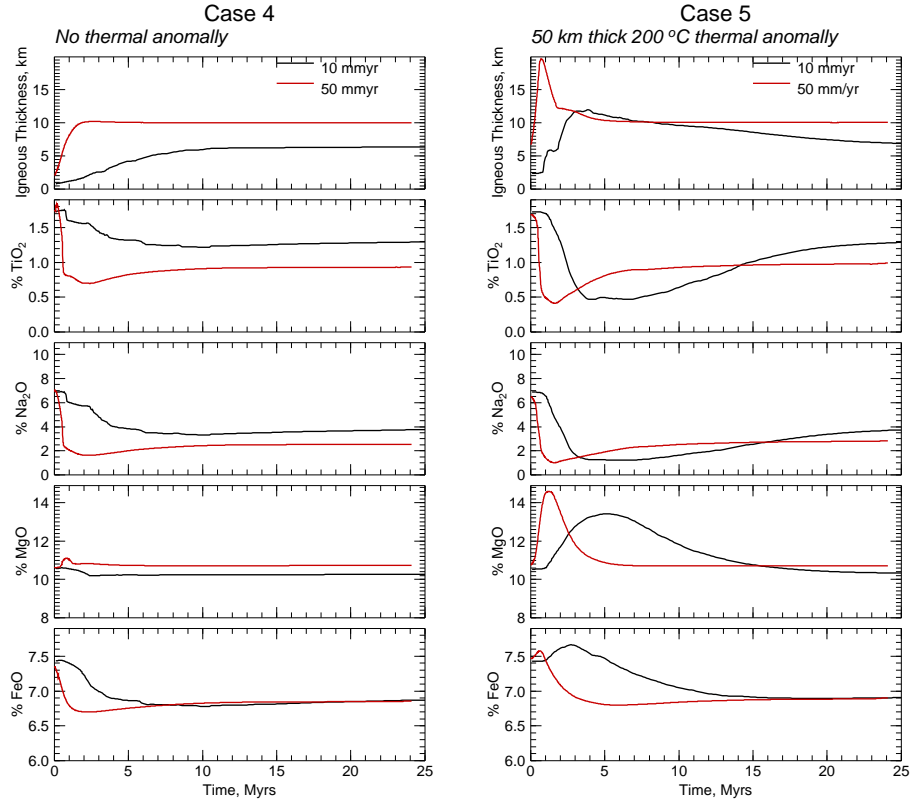
FIGURE 5.4: Igneous crustal thickness and selected major element composition of melt for the two initial conditions: *Case 4*, where the lithosphere is pre-thinned as an initial condition, with no thinned regions and no thermal anomaly beneath, and *Case 5*, where a 50 km thick 200 °C thermal anomaly exists beneath the pre-thinned lithosphere. Half spreading rate is increased from 10 to 50 mm yr^{-1}.

advected into this narrow region prior to rifting. The evolution without and with a 50 km 200 °C hot layer beneath the lithosphere (case 4 and 5) is tested. The most obvious outcome is that rifting above a thermal anomaly leads to thickened crust at all spreading rates (Figure 5.4). Yet if Figures 5.2 and 5.4 are compared, the pre-thinning has had the clear effect of increasing the melt generation during early rifting. This is clear from the upwelling ratio (Figure 5.5). Without the presence of a thermal anomaly, the pre-thinned model (case 4) has a significantly increased upwelling velocity compared to the half spreading rate (Figure 5.5). The pre-thinned region focuses flow upon breakup, which increases the igneous crustal thickness more rapidly as the model evolves. When there is no thermal anomaly present, however the onset of significant melting is merely delayed (Nielsen and Hopper, 2004). From the profiles of igneous thickness, the flat lithosphere model (case 1) extends for 14 Myrs before significant crust is generated, which is much delayed when compared to the pre-thinned model (case 4).
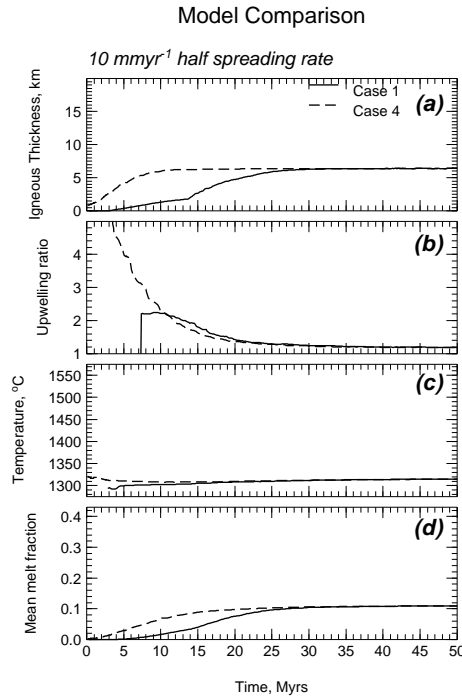
FIGURE 5.5: Effect of a pre-thinned region as an initial condition without the presence of a thermal anomaly (*case 1* and *4*): (a) Igneous crustal thickness; (b) ratio of the average upwelling velocity within the melting region against the half spreading rate; (c) mean mantle temperature within the melt region; and (d) mean melt fraction within the melt region.

The melt production characteristics of case 1 at a slow half spreading rate of $10\,\mathrm{mm\,yr^{-1}}$ shows a resemblance margins where there is a lack of excess magmatism (Figure 5.5). It has been suggested that the rate of spreading should be ultra slow ($< 10\,\mathrm{mm\,yr^{-1}}$) for melting to be suppressed significantly at a rifted margin (Bown and White, 1995). Here however by simply passively extending the lithospheric lid, I have shown that it is not stretched sufficiently at slow rates of extension to allow for significant decompression melting.

The presence of the pre-thinned region in combination with a thermal anomaly has a far greater effect on the volumes of material generated than when there is not a pre-thinned region (Figure 5.6). Upon the pulse of increased melt production there is a peak of enrichment of FeO and MgO, and increased depletion in TiO_2 and Na_2O (Figure 5.4). This reflects the presence of early deep melt combined with slightly later shallow and high ($\sim 18\,\%$) melt fractions. This is not the major effect though: the upwelling ratio is greatly enhanced by the thinned lithosphere reflecting the focussing of extension,
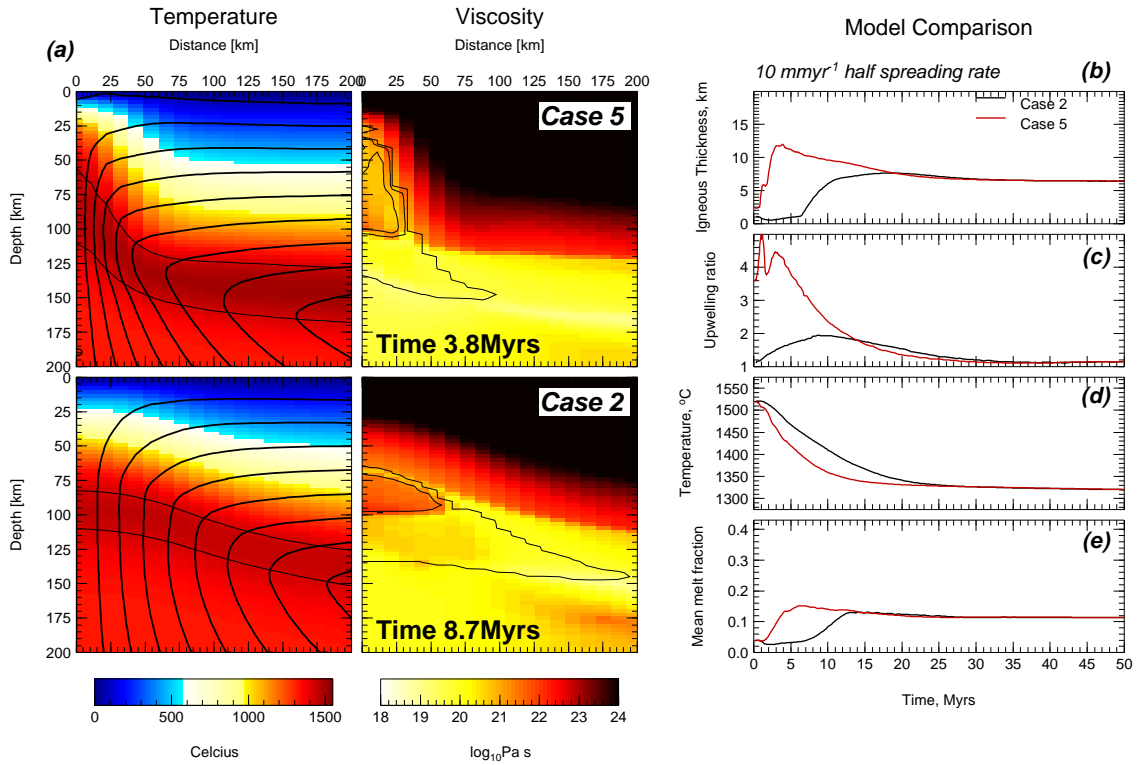
FIGURE 5.6: Comparison of the effect of a pre-thinned region as an initial condition in the presence of a 50 km 200 °C thermal anomaly (*case 2* and *5*). (a) in these four panels are plots of temperature and flow of the mantle; and viscosity and contours of 0, 2 and 10 % melt production. These properties are plotted for a 200 by 200 km region at the centre of extension. The ages chosen are that of peak melt generation for each model. On the right are comparisons of: (b) igneous crustal thickness; (c) ratio of the average upwelling velocity within the melting region against the half spreading rate; (d) mean mantle temperature within the melting region; and (e) mean melt fraction within the melt region.

resulting in greatly enhanced melt production. The pre-thinned wedge within a model of rifting clearly has a large effect on melting within the model at slow spreading rates.

The pre-thinned initial condition reduces the viscosity of the upper lithosphere as the viscous lid has been extended and replaced by lower viscosity mantle. This creates a region where the flow of mantle material can reach shallower depths. The models indicate that if an exhaustible thermal anomaly is to have a large effect on the melt generation at slow spreading rates it must be combined with some pre-thinning of the lithosphere. Such thinning can be provided in two forms: first there could be a period of fast extension that thins the lithosphere rapidly, then spreading rates reduce and extension continues. Such a scenario has been shown to reproduce major element chemistry and igneous thickness

of Southeast Greenland (Armitage et al., 2008). Alternativly the thermal anomaly may
be introduced after rifting has begun, or after a prior rifting event. Such a scenario may
be present given the complex rifting history of the North Atlantic with many extensional
basins that formed prior to the onset of rifting ~ 56 Ma (Smythe, 1989; Larsen et al.,
1998; Smith et al., 2005; Storey et al., 2007a).

5.3.3   Multiphase Rifting Events

The consequences of realistically thinning the lithosphere prior to the arrival of a thermal
anomaly are now explored. A multiphase rifting event is simulated: A flat lithosphere
is extended causing some thinning. This is followed by the arrival of a thermal anomaly
and re-initialisation of rifting. Sensitivity to three parameters is tested: The amount of
extension during the initial extensional event; the distance between the initial extensional
event and subsequent rifting event above a thermal anomaly; and the time between both
events. Rather than confining extension to a narrow region I allow the extension to
evolve through time as the initially flat lithosphere extends. In these simulations I do
not address what may cause the relocation, merely impose the shift in rift position.

Ridge jumps may be the consequence of the arrival of the plume head. The plume
will erode the lithosphere by the advection of material due to the buoyant upwelling of
the new hot material (Jurine et al., 2005). Re-localisation of the centre of extension
is then encouraged by the eventual penetration of plume material through the crust
(Mittelsteadt et al., 2008). The spreading centre may otherwise jump into a region of
older crust, such as a slab of continental crust. As extension continues the weaker crust
is replaced by stronger mantle (Newman and White, 1997). Therefore if there is a region
of older crust near the new rift the strain may re-focus there (Davis and Kusznir, 2002).

The extension that forms the pre-thinned region of lithosphere inherently generates some
melt due to decompression, even at the slowest rates of extension. For example, at a half
spreading rate of $5\,\mathrm{mm\,yr^{-1}}$ about 1 km of melt is generated after 10 Myrs of extension.
As the spreading rate is increased the melting occurs sooner and in greater volumes (see
Figure 5.7). The continental lithosphere correspondingly thins at a faster rate when the
spreading rates are increased. To understand the spatial and temporal sensitivity to a
prior extensional event I will therefore generate a suite of models with initial conditions
formed by extending the lithosphere at different rates. A set of physically realistic ini-
tial conditions, shown diagrammatically in Figure 5.8, are then formed. Rifting at a
half spreading rate of $10\,\mathrm{mm\,yr^{-1}}$ is then imposed over a $200\,^{\circ}\mathrm{C}$, $50\,\mathrm{km}$ thick thermal

Extension of Lithosphere
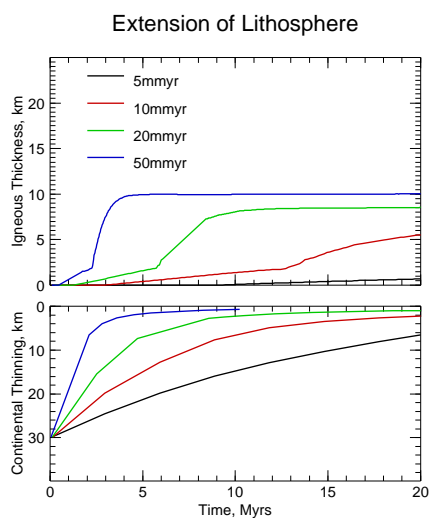
FIGURE 5.7: Igneous crustal thickness and thinning of the continental lithosphere at different half rates of extension.

Pre-thinned region of lithosphere

Rifting offset from the pre-thinned region
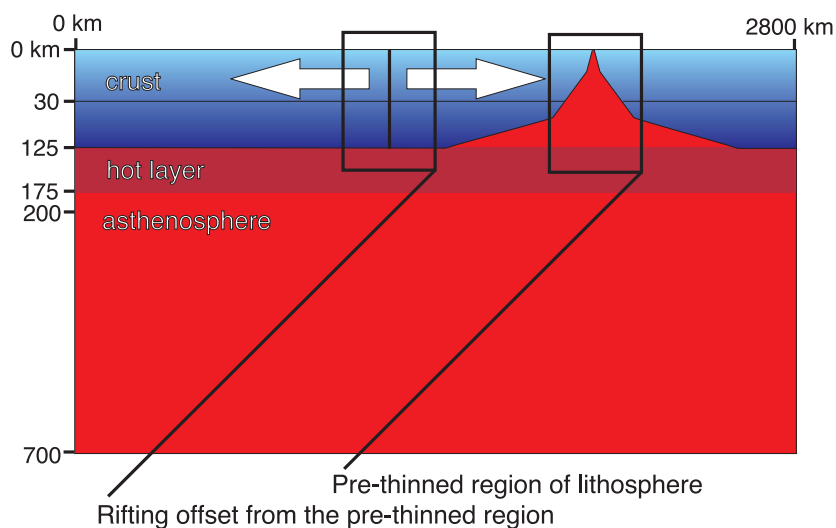
FIGURE 5.8: Diagram of a hypothetical situation where there is a previous region of extension offset from the position of the new rift. I extend the lithosphere at $5\,\mathrm{mm\,yr^{-1}}$ for a set period of time to gain the appropriate stretching factor (see Figure 5.7). The rifting is offset to the left by shifting the kinematic boundary condition of spreading.

anomaly. This rift event occurs at increasing distances from the centre of the old extensional event and after increasing periods of passive conductive cooling (see Figure 5.8).

In the following sections, initially the focus will be on the distance between the prior extension and subsequent rift. In these cases the prior extension is slow ($5\,\mathrm{mm\,yr^{-1}}$) to limit the melt generated during the prior extension. Then the effect of the rate of extension (between 5 and $50\,\mathrm{mm\,yr^{-1}}$) and the degree of extension during the prior event (stretching factors of up to 9) will be explored. Finally the effect of passive conductive cooling between the prior extension and rift will be simulated.

5.3.3.1 Rifting at Increasing Distances From Pre-thinning Event

First, the effect of distance between the prior extension and subsequent rifting of the lithosphere upon the evolution of the multiphase rifting scenario will be looked at. Three distinct steps are considered. In step 1, the lithosphere is thinned by extension at a half rate of $5\,\mathrm{mm\,yr^{-1}}$ for a period of between 2 and $30\,\mathrm{Myr}$ (Figure 5.7). In step 2, the extended lithosphere at the chosen time interval is then used as the initial condition. In step 3, lithosphere immediately rifts following a simulated ridge jump of 44, 88, 175, or $350\,\mathrm{km}$. The shift in rift axis is purely imposed by the divergent boundary condition shifting. The evolution of this scenario for a $44\,\mathrm{km}$ shift in centre of extension is displayed in Figure 5.9. The second phase of extension or 'rift' forms above a $50\,\mathrm{km}$ thick $200\,^{\circ}\mathrm{C}$ thermal anomaly (Figure 5.10a).

Second, the effect of the rate of extension during the initial extensional phase upon the evolution of the multiphase rifting scenario will be looked at. The sequence of events was as before, but this time the lithosphere is thinned by extension at half rates between 5 and $50\,\mathrm{mm\,yr^{-1}}$. Then a ridge jump of $44\,\mathrm{km}$ was simulated, and rifting followed immediately after (Figure 5.10b).

As with the wedge shaped necking region in Section 5.3.2, the hot layer is advected into the thinned region of lithosphere when second phase of extension is initiated. The thinning due to the first extensional phase also leaves the lithosphere depleted due to the melting that occurred (for example the depletion in titanium oxides, see Figure 5.9). The effect of the second phase of extension occurring at increasing distances from the first phase of extension, is that melt production during breakup of the lithosphere is reduced (Figure 5.10a). The reasons are as outlined previously: for a thin thermal anomaly to have an impact on the melting characteristics it needs a region of pre-thinned lithosphere. As the rift event jumps successively further from the pre-thinned
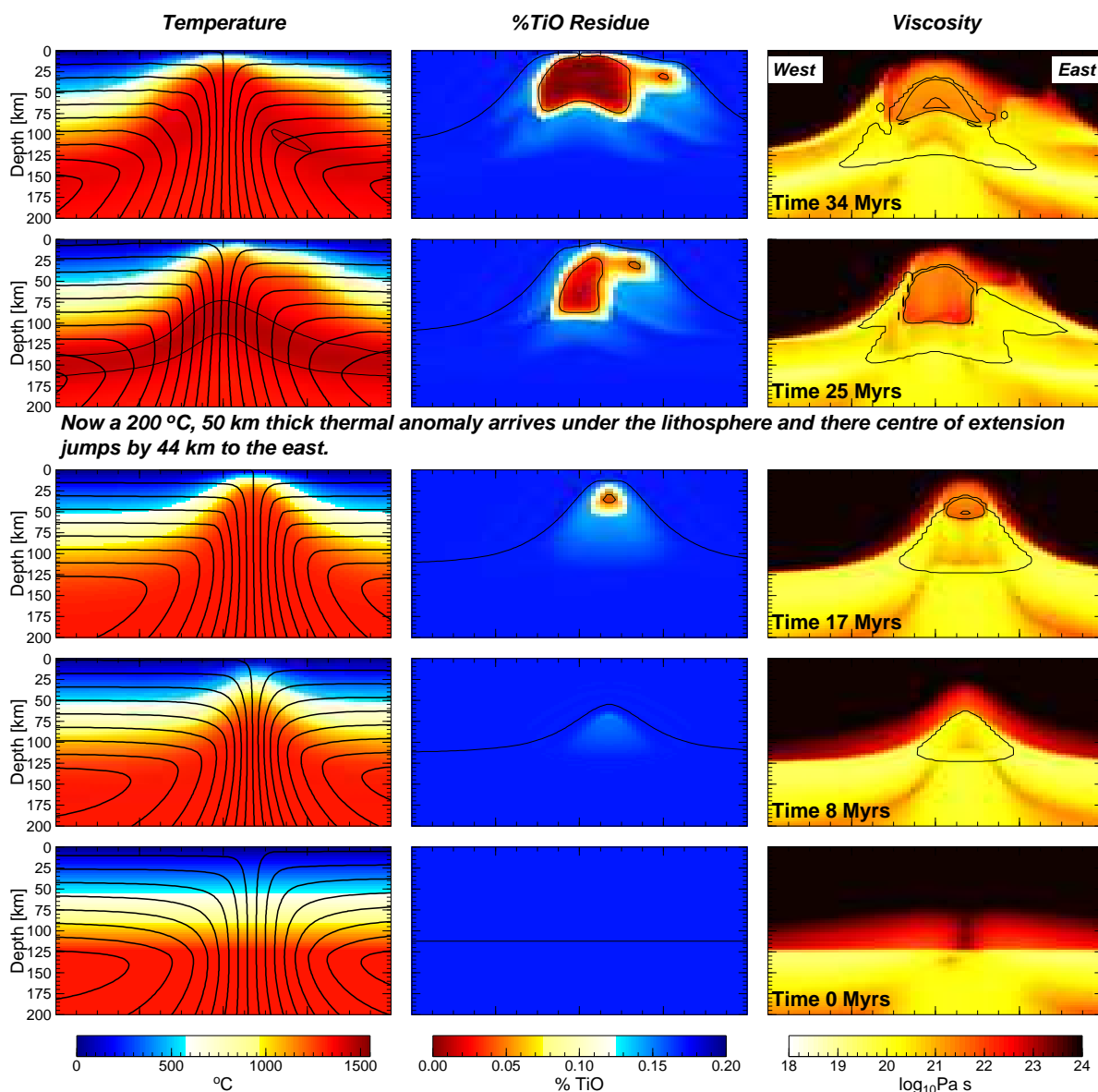
FIGURE 5.9: Evolution of a multiphase rifting event where time begins at the beginning of the first phase of extension. The rift occurs in two stages: an initial period of extension at a half spreading rate of $10\,\mathrm{mm\,yr^{-1}}$ that lasts $17\,\mathrm{Myrs}$. At this point the lithosphere is extended by a factor of 10. Then the centre of extension shifts to the east by $44\,\mathrm{km}$, and a $50\,\mathrm{km}$ thick $200\,^{\circ}\mathrm{C}$ thermal anomaly is emplaced beneath the lithosphere. Extension continues thereafter at a half spreading rate of $10\,\mathrm{mm\,yr^{-1}}$. Plotted are temperature and flow with $1425\,^{\circ}\mathrm{C}$ contoured to help show the thermal anomaly. Titanium oxide concentration in the solid mantle is also sown, with $10\,\%$ depletion contoured, which helps define the base of the lithosphere. Viscosity is plotted with the melt region outlined including the $2\,\%$ and $10\,\%$ melt intervals contoured.
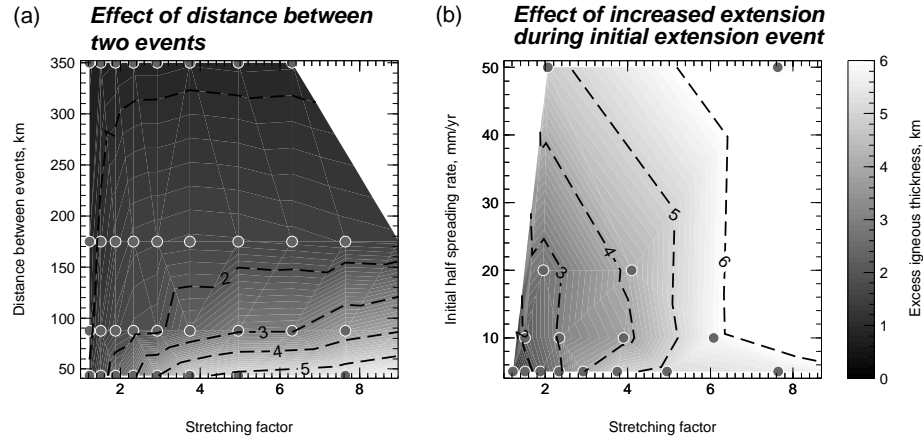
FIGURE 5.10: Comparisons of the excess igneous thickness, which is the difference between peak thickness and a steady state crustal thickness of 7 km (a) Initial phase of extension at $5\,\mathrm{mm\,yr^{-1}}$ followed by the second phase of extension at a half spreading rate of $10\,\mathrm{mm\,yr^{-1}}$ above a 50 km thick $200\,°\mathrm{C}$ thermal anomaly. The second phase of extension, 'rift', occurs after increasing stretching of the lithosphere and at increasing distances from the initial extensional event. (b) Initial phase of extension at different half spreading rates followed by the second phase of extension at a half spreading rate of $10\,\mathrm{mm\,yr^{-1}}$ above a 50 km thick $200\,°\mathrm{C}$ thermal anomaly. The grey circles mark data points, which have been interpolated to produce the contours of excess igneous crust.

region that pre-thinning has progressively less influence. Extending the lithosphere for greater periods of time prior to rifting has minimal impact on melt volumes, especially when compared to the effect of proximity between phases of extension (Figure 5.10a). If 3 km of igneous crust, which is in excess of the 7 km thickness at steady state, is the boundary between a rift being highly volcanic or not, then the critical distance for the influence of the pre-thinned region to have an affect is around 100 to 120 km.

As the half spreading rate of the initial phase of extension is increased, melt production during extension is increased (Figure 5.7). Likewise the excess igneous thickness from the second phase of extension is increased (Figure 5.10b). There are two competing processes within this observation: First there is the thinning of the lithosphere during the initial extension event that leads to enhanced melting. Second, there is a degree of depletion of the upper lithosphere due to prior melting during the initial extensional event. At slow spreading rates the volumes of melt generated are very small (Figure 5.7). With a half spreading rate of $5\,\mathrm{mm\,yr^{-1}}$ the degree of extension is the main control on peak igneous thickness. Extension of the lithosphere when the half spreading rates are $20\,\mathrm{mm\,yr^{-1}}$ is still the main control on peak igneous thickness (Figure 5.10b). It is only when the lithosphere is extended rapidly during the first extension phase that depletion of the mantle begins to affect melt production during the second extension phase.

To summarise, the primary control on the excess melting upon rifting other than the presence of the thermal anomaly, is the proximity of the secondary extensional phase to the region that is thinned by the initial extension phase. The second consideration is the spreading rate of the initial extensional phase, as this controls the width of the base of the thinned region prior to rifting.

5.3.3.2 Rifting After an Increasing Period of Time

By removing all kinematic boundary conditions of spreading the lithosphere cools by passive conduction. The viscosity of the lithospheric lid is defined by its depletion to be 10^{23} Pa s (Nielsen and Hopper, 2004). Viscosity within the mantle beneath is given by the rheological definition,

$$\eta = A\chi_{H_2O}\chi_m exp\left(\frac{E + PV}{nRT}\right)\dot{\epsilon}^{\frac{1-n}{n}} \tag{5.5}$$

where E and V are the activation energy and volume, R is the gas constant, T is the absolute real temperature, $\dot{\epsilon}$ is the strain rate and n is the stress exponent. A is calculated from a reference state that is set at the start of each model run. χ_{H_2O} and χ_m parametrise the effect of dehydration and melt respectively. When there is no strain rate and no melt production, which is the case for most of the model space when convection is not imposed then this relationship becomes,

$$\eta = A exp\left(\frac{E + PV}{nRT}\right) \tag{5.6}$$

and the viscosity is a function of temperature and pressure. The effect of this is that the viscosity contrast between the base of the lithospheric lid at 125 km and upper mantle is only one to two orders of magnitude. The result is that the thermally defined lithosphere thickens due to thermal conduction. Drip like instabilities and small scale convection do not form as would be expected (Solomatov and Moresi, 2000), as a source of internal heating to maintain a high viscosity contrast is not included within this model.

I wish to assess the period of time that a region of thinned lithosphere requires to thicken sufficiently such that the rift characteristics are as that with no pre-thinning. The sequence of events are now; firstly, the lithosphere is thinned by the first phase of extension at a half rate of $5\,\text{mm}\,\text{yr}^{-1}$ until the lithosphere is extended by a stretching factor of 9 (approximately 30 Myr); secondly, the lithosphere is allowed to cool for a period of time between 0 and 100 Myrs by removing the surface boundary conditions; thirdly, the second phase of extension at a half spreading rate of $10\,\text{mm}\,\text{yr}^{-1}$ follows a

(a) ***Melt Generation***

(b) ***Effect of Cooling Lithosphere***
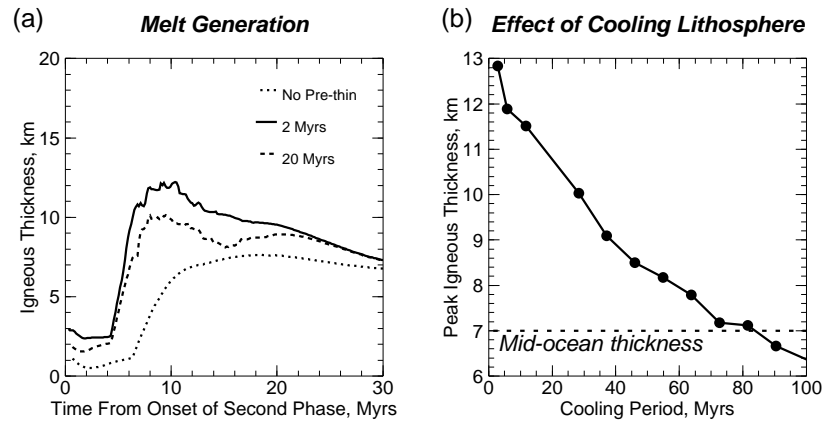
FIGURE 5.11: (a) Plot of igneous thickness (taken from half the melt region) for rifting after a hiatus of 2 and 20 Myrs from the initial extensional event of extension at $5\,\text{mm}\,\text{yr}^{-1}$ for 30 Myrs. For comparison I have displayed the results for a rift system where there is no pre-thinning or prior extensional event. (b) Peak igneous thickness is plotted as a function of the period of cooling between prior extension and rifting for the multiphase rift scenario: Extension at $5\,\text{mm}\,\text{yr}^{-1}$ for 30 Myrs followed by a period of cooling and then rifting at $10\,\text{mm}\,\text{yr}^{-1}$ above a 50 km thick $200\,^\circ\text{C}$ thermal anomaly

simulated ridge jump of 44 km. The second phase of extension is once again forms above a 50 km thick $200\,^\circ\text{C}$ thermal anomaly.

The static lid will cool to a thickness that is greater than what would be expected as there is no internal heating or convection in the model to maintain a high viscosity contrast beneath the lithosphere. The effect of this is that if the model is held static for more than 80 Myrs, then the lithosphere thickens beyond 125 km and melt generation becomes reduced (see Figure 5.11). Yet as long as the lithosphere does not remain static for a period of time greater than 80 Myrs, then this simple approach of removing the boundary conditions as a simulation of a hiatus between two extensional events is valid.

With increasing periods of cooling it is clear that the pulse of high volume melt production is reduced (Figure 5.11). By around 30 Myrs the peak igneous thickness is half as much when compared to the steady state thickness of 7 km. As I suggested earlier, when the second extension phase has more than 3 km of excess igneous thickness it is highly volcanic, then for a initial extension phase in conjunction with a thermal anomaly to be the cause of this excess melting, that extensional event must have occurred no more than 30 Myrs prior to rifting.
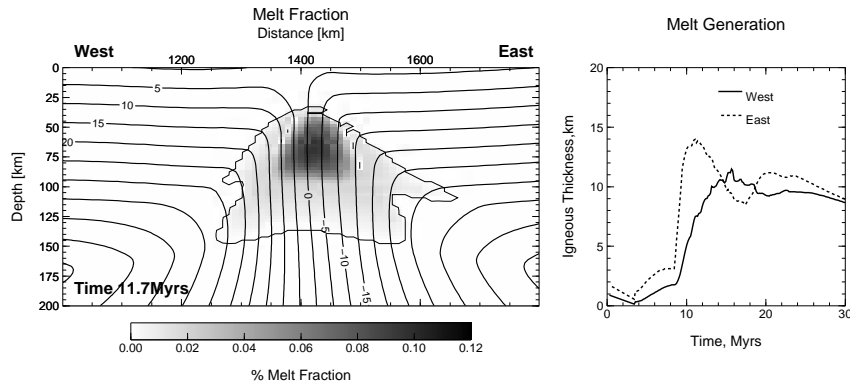
FIGURE 5.12: Left: Time slice of the lithosphere after 11.7 Myrs of rifting. The rift has formed from a pre-thinned condition 43.75 km to the left of the rift, with a stretching factor of 9 that has cooled for 20 Ma. A 200 °C thermal anomaly was placed under the lithosphere after pre-thinning and extension re-initiated at half spreading rates of 10 mm yr^{-1}. The contours are of streamlines of flow, the shaded region is of melt fraction within the melt region. Right: Igneous thickness plotted comparing right and left sides of the rift, as the rift evolves the volume of melt generated oscillates from more on the right, then left, then right side of the rift.

5.3.3.3 Asymmetry in the Melt Region

The melt region that forms from these multiphase rifting scenarios may become asymmetric (as is clear in Figure 5.9). From studies of the East Pacific Rise there is clear evidence that asymmetric melt regions exist and in this case asymmetry is commonly attributed to ridge migration (Carbotte et al., 2004; Toomey et al., 2002), or alternatively, this is equivalent to asymmetric rifting speeds in a frame in which the extensional axis is stationary. There is some evidence that an asymmetric melt region expresses itself in asymmetric lithospheric thickness at fast spreading centres such as the East Pacific Rise (Dunn and Forsyth, 2003). The method used here to solve the combined Stokes and energy equations of flow use a centre of mass formulation. To understand the focussing of melt requires a two phase flow model that can separate the flow of melt from the creep of the solid mantle, such as Spiegelman (1996). These models have been used to try to understand how melt is focused towards the centre of extension (Katz et al., 2006).

In the absence of more detailed information there are two choices: to split the melt region down the centre of extension, and assume all melt within the left half is emplaced on the left side of the extensional regime and so on; or we can assume all melt is equally divided between both regions. The previous sections, 5.3.3.1 and 5.3.3.2, have followed the second approach, that all melt is split evenly between both margins. In the following we split the melt region in two (Figure 5.12).

From a time slice of the shape of the melt region and the distribution of melt within the melt region, during breakup there is quite significant asymmetry (Figure 5.12). After 11 Myrs of rifting we can see that melt production is greater towards the left, side of the melt region. Counter balancing this is the asymmetry of the shape of the melt region about the centre of extension (at 1400 km). Due to this asymmetry the overall igneous thickness predicted on left and right sides varies a little erratically as the rift evolves. As the pre-thinned condition is to the right of the rift, the solidus will be at shallow depths to the right giving increased initial melting. Furthermore the viscosity within the pre-thinned region is lower, so the flow is increased generating further melt. This produces the variation in igneous thickness on left and right sides of the model. Therefore when considering asymmetries in melt accretion to the crust, off axis extensional events should be included.

5.4   Application to the Opening of the North Atlantic

A simulation of rifting along the Southeast Greenland margin that included variable spreading rates and a thermal anomaly reproduced the observed igneous crustal thickness (Armitage et al., 2008). The melts generated were also high in MgO, as observed (Thy et al., 1998; Armitage et al., 2008). This simulated rifting event had a pre-thinned initial condition, as in Cases 4 and 5 (Section 5.3.2). Such a thinned region prior to the final extension phase that leads to continental rifting and sea floor spreading, is likely justified given the extensive rift basins that developed in the North Atlantic off shore Southeast Greenland and the UK prior to 60 Ma. In this section, the effect of pre-thinning will be tested by forming a model of the multiphase opening of the North Atlantic. The formation of the conjugate Hatton Bank – Southeast Greenland margin was preceded by extensional events (Figure 5.13), which led to the formation of the Rockall Trough, at between 200 to 300 Ma; the Hatton-Rockall Basin, prior to 80 Ma (Edwards, 2002; Bull and Masson, 1996; Smythe, 1989); and there is a small amount of evidence from deep marine pre-rift sediments for a pre-rift sedimentary basin of Southeast Greenland, at around 61 Ma (Larsen et al., 1998). The formation of the Hatton-Rockall Basin and the pre-rift basin off Southeast Greenland are likely candidates for pre-rift extensional phases, given that the North Atlantic oceanic crust was formed at 56 Ma (Larsen et al., 1998; Hopper et al., 2003; Storey et al., 2007a).

The Hatton-Rockall Basin is separated from magnetic anomaly C24r by the Hatton Bank, which is close to 100 km wide at its widest point. This basin is within the range at which the test scenarios suggest it will influence subsequent rift development. The stretching factor at the Hatton-Rockall Basin is thought to be around 2, based on a

North Atlantic
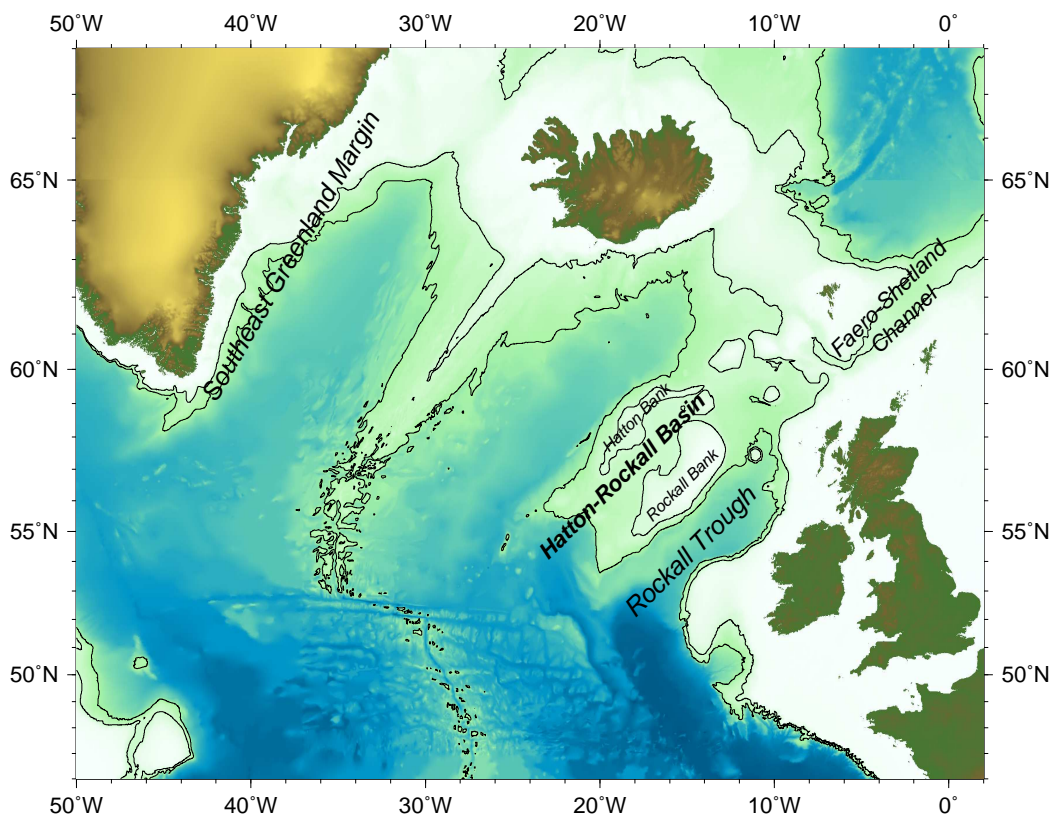
FIGURE 5.13: North Atlantic bathymetry, showing the locations of the Hatton-Rockall Basin and Rockhall Trough

decrease in crustal thickness from 30 km to 15-16 km (Smith et al., 2005). Just prior to rifting, there is evidence of a extensional basins along the Southeast Greenland margin (Larsen et al., 1998). From analyses of sediments buried under flood basalts at ODP site 917, it is suggested that this pre-rift basin was similar to the Kangerlussuaq basin (Larsen et al., 1998). The authors further suggest that the basin likely formed just prior to the most early magmatism, at around 61 Ma. Taking the similarities between this pre-rift basin and the Kangerlussuaq basin, which subsided by ~ 700 m prior to 61 Ma (Peate et al., 2003), then it is likely that the pre-rift basin was extended by only a small factor of 1.1.

Thus the regional geology indicates that there are two extensional phases prior to breakup that need to be considered, as summarised in Table 5.1. This is more complex

TABLE 5.1: Series of extension phases leading up to the opening of the Southeast Greenland and Hatton Bank margin

Age	Phase of Extension	Event
91 Ma – 80 Ma	1	Extension of the Hatton-Rockall Basin to a stretching factor of 2, at a half spreading rate of $5\,\mathrm{mm\,yr^{-1}}$.
80 Ma – 62 Ma		No extension
62 Ma – 61 Ma	2	Extension of the pre-rift basin, after a shift in the centre of extension of 100 km to the East, to a stretching factor of 1.1, at a half spreading rate of $10\,\mathrm{mm\,yr^{-1}}$.
61 Ma – 56 Ma	3	Extension and rifting of the Southeast Greenland and conjugate Hatton Bank margins above a 100 or 200 °C thermal anomaly, at a half spreading rate of $40\,\mathrm{mm\,yr^{-1}}$.
56 Ma – present		Continued rifting at $10\,\mathrm{mm\,yr^{-1}}$.

compared to the test simulations in the previous section, however the same principles should hold. The first and second phase of extension will thin the lithosphere, which may facilitate channelising of the distal plume material at 61 Ma and providing the required thermal anomaly (Storey et al., 2007a). Rapid emplacement is indicated, otherwise conductive cooling of the emplaced material would suppress subsequent melt production. The spreading rates chosen for the first two extension phases are chosen to match the estimated stretching factor, given the periods of time over which extension is thought to occur (Table 5.1). The Hatton-Rockall Basin is a wide basin (Edwards, 2002) and so may have extended over a long period of time.

The existence of increased spreading rates during breakup means that the two small extension phases prior to rifting have a large impact on the thinning, melt production and resultant igneous crustal thickness (Figures 5.14 and 5.15). Melt production is very high for a 200 °C thermal anomaly (Figure 5.14). The predicted igneous thickness off the Southeast Greenland margin is close to 23 km (Figure 5.15). This is thicker than wide angle surveys suggest (Hopper et al., 2003; Holbrook et al., 2001). A 100 °C thermal anomaly under-predicts the thickness of the Southeast Greenland margin in this multiphase rifting scenario. With a 100 °C thermal anomaly, the TiO_2 and Na_2O
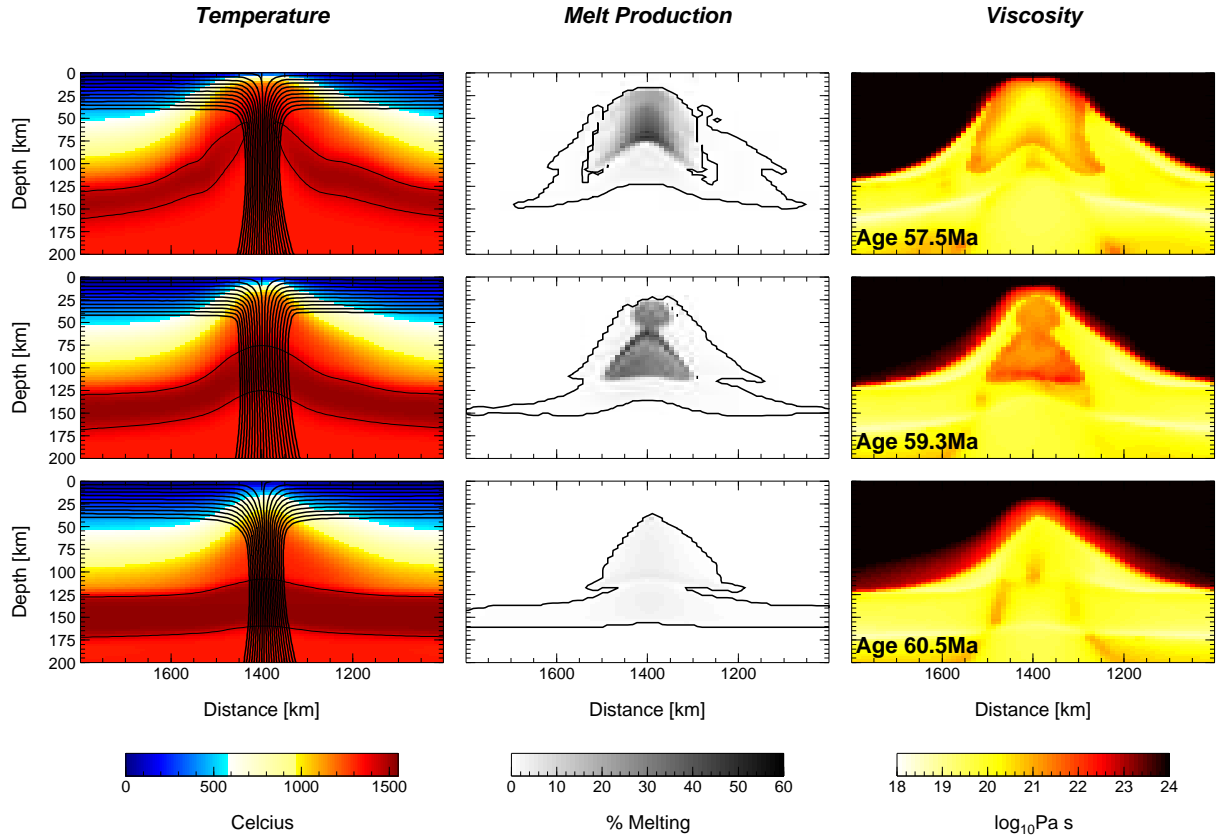
FIGURE 5.14: Temperature, melt production and viscosity during the third and final phase of extension within the simulation of the opening of the North Atlantic at the Southeast Greenland and Hatton Bank conjugate system above a 200 °C thermal anomaly (see phase 3 in Table 5.1). The thermal anomaly is outlined within the temperature plots as within Figure 5.9.

depletion is matched. MgO and FeO compositions are under predicted, although this maybe due to the choice of major element parametrisation (Armitage et al., 2008). It appears that the combined effects of extension phases 1 and 2 justify the pre-thinning assumed within Armitage et al. (2008) and Nielsen and Hopper (2004) for the rifting of Southeast Greenland.

The series of phases of extension have however not reproduced asymmetry in igneous crustal thickness, as observed between the Hatton Bank and Southeast Greenland sides of the margin (Figure 5.16; Hopper et al., 2003). The melt region generated is not asymmetric for the multiple phase extension scenario (Figure 5.14). To explain the observed asymmetry may require the possible asymmetric spreading rates to be modelled. The Hatton Bank opened at slightly fast extension rates of around $22\,\mathrm{mm\,yr^{-1}}$ (Smallwood and White, 2002). This leads to the suggestion that the fast extension off Southeast
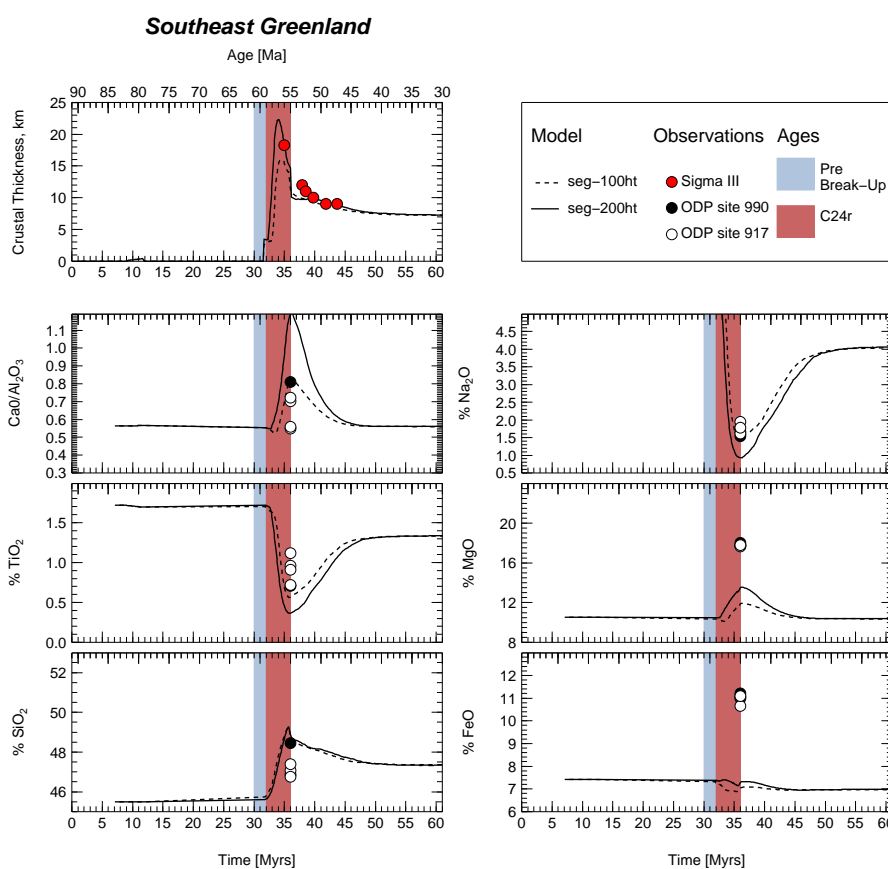
FIGURE 5.15: Comparison of simulated multiphase rift evolutions for the Southeast Greenland margin. Rifting at a half spreading rate of $10 \, \text{mm} \, \text{yr}^{-1}$ follows after a initial period of extension until the lithosphere is stretched by a factor of two and then cooled for 20 Myrs. Dashed line is for a fast initial extensional event at $50 \, \text{mm} \, \text{yr}^{-1}$ that lasts for 2 Myr. The solid line is for a slow initial extensional event at $5 \, \text{mm} \, \text{yr}^{-1}$ that lasts 10 Myr. Plotted are the igneous crustal thickness and selected major element melt composition.
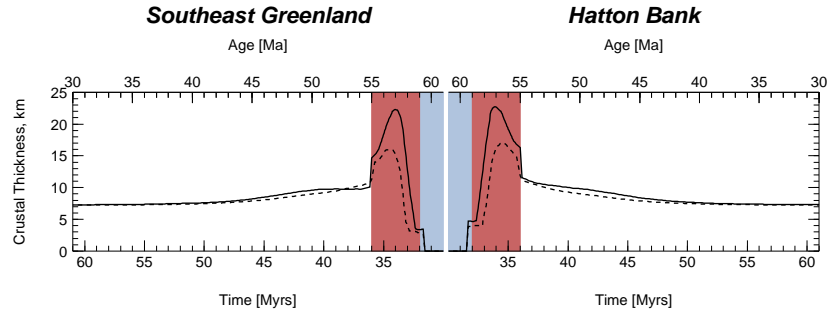
FIGURE 5.16: Igneous crustal thickness for the Southeast Greenland and Hatton Bank side of the final phase of extension of the simulated opening of the North Atlantic (see Table 5.1).

Greenland was accommodated by either ridge migration or a ridge jump (Smallwood and White, 2002; Hopper et al., 2003).

5.5 Conclusions

1. Passive far field extension of the lithosphere above a thermal anomaly, such as thought to have pooled beneath the Southeast Greenland and Hatton Bank margins, will not produce excess melt. It is only when the lithosphere is thinned prior to rifting that in combination with a thermal anomaly that excess breakup magmatism is generated.

2. Passive extension at $10 \, \text{mm} \, \text{yr}^{-1}$ of the lithosphere that has not been pre-thinned shows an igneous crustal structure that may represent a magma-poor margin. Therefore, such magma-poor margins may be a consequence of the rifting of continents without any prior extension.

3. The effect of thinning that resulted in the Hatton-Rockall Trough and a possible pre-rift basin off Greenland, in combination with a thermal anomaly of between 100 and $200 \, °\text{C}$, produce the observed igneous thickness and melt compositions off Southeast Greenland.

The importance of the thickness of the lithosphere at the time of rifting has been shown. It is clear that simple assumptions for the amount of extension cannot be made, as the rift is sensitive to the amount of pre-thinned extension undergone, and how far the rift

is from that pre-thinned region. Likewise, the pre-thinning event remains of importance to rift development for many years ($\sim 30\,\text{Myrs}$).

Given these considerations, the high volumes of material emplaced during the opening of the North Atlantic requires a pre-thinning event. Without thinned lithosphere prior to breakup there would be no excess melt production due to the thickness of the lithosphere dampening any upwelling. I therefore strongly state that, no matter the thermal state of the lithosphere, for the emplacement of large amounts of melt at slow rates of extension, the lithosphere must have undergone some extension prior to breakup.

Chapter 6

Conclusions and Future Work

6.1 Conclusions

1. The major and rare-earth element composition of melt generated during the extension and rifting of the continents has been successfully predicted within a geodynamic model of rifting. The melt composition calculations are modular, and could be incorporated within other models of rifting where the fraction of melt generated is calculated.

2. It has been shown that the strengthening of the mantle, when small fractions of melt are generated, is of fundamental importance to the evolution of rifted margins. It acts to dampen small-scale convection and reduce the volume of melt generated at slow spreading rates and mantle temperatures greater than $1300\,^\circ$C. I have shown that to match the global igneous crustal thickness variations, the mantle is between 1300 and $1325\,^\circ$C, which is in agreement with the latest estimates from heat flux calculations (McKenzie et al., 2005).

3. Around the coast of the North Atlantic there are regions of very thickened igneous crust known as the North Atlantic Igneous Province. At the Southeast Greenland margin, the igneous thickness is up to $18\,$km (Hopper et al., 2003). The melt generated at the time of rifting is picritic with very high concentrations, $18\,\%$, of MgO (Thy et al., 1998) and depleted in rare-earth elements. To reproduce high volumes of melt with this chemical signature requires three processes:

Firstly, the presence of a layer of hotter mantle beneath the lithosphere. This layer is $\sim 200\,^\circ$C hotter than the mantle, which has a potential temperature of $1325\,^\circ$C. Such a thermal anomaly is consistent with the lateral movement of a thermal plume based under Iceland (Holbrook et al., 2001; Chapter 4).

Secondly, rifting occurred initially at a faster rate of spreading, $\sim 40\,\mathrm{mm\,yr^{-1}}$ (Chapter 4). This is in agreement with observational evidence for increased spreading rates off shore Southeast Greenland (Larsen et al., 1998; Hopper et al., 2003). Such increased spreading rates are essential as it increases the amount of mantle welling upwards and so increasing the flux of material through the solidus.

Finally, extension events prior to the rifting are crucial to the generation of excessive melt upon breakup. Passive far field extension of a $125\,\mathrm{km}$ thick lithosphere above a thermal anomaly, even at the faster spreading rates of $\sim 40\,\mathrm{mm\,yr^{-1}}$, does not produce sufficient melt to match the $18\,\mathrm{km}$ thick crust observed off Southeast Greenland. The combined effect of the extension that gave the Hatton-Rockall Basin and a prior extensional basin off Southeast Greenland provides enough extension to thin the lithosphere sufficiently, enhancing the upwelling of material (Chapter 5).

The variation of seismic velocity within the underplate off Southeast Greenland with the igneous thickness is reproduced by the breakup scenario outlined above. The geodynamic model of the extension and rifting of the continents developed in this thesis has proved to be a successful tool for understanding the controls on melt generation during continental extension and breakup.

6.2 Future Work

Modelling the evolution of rifted margins is highly complex, and in this thesis I have only covered a few aspects, which are applied mainly to volcanic rifted margins. By calculating the composition of melt within the mantle, further insights have been gained into the controls on melt generation at these margins and in particular the Southeast Greenland margin. The first direction that this model should be taken, is to model other rifted margins. In the next few months I will apply this model to the Seychelles Laxmi Ridge system in the Indian Ocean. Yet, there is scope for this model to be applied to all margin styles, to try to understand what controls rifting in various settings.

Other than applying the model to new locations, there is significant room for developing this model further. In Chapter 5, the effect of pre-thinning on rift development is studied. It was found that there is the possibility that some asymmetry in the melt region is formed. The volumes of igneous material emplaced at the Southeast Greenland and Hatton Bank margins is asymmetric (Hopper et al., 2003). This asymmetry is possibly related to ridge migration (Hopper et al., 2003). Toomey et al. (2002); Conder et al. (2002) and Conder (2007) have used a geodynamic model to explore ridge migration at the East Pacific Rise. To do so their models had left and right boundary conditions

that allowed the flow of material through them. The version of *CitCom* that has been developed in this thesis is not capable of such boundary conditions. However, there is a newer version of this code where such boundary conditions have been applied (van Huenen and van Wijk, 2007). Therefore it would be possible to integrate the melting and melt composition modules within this version.

CitCom is now managed within the Computational Infrastructure for Geodynamics (http://www.geodynamics.org/). The code is available to run in parallel and in three dimensions. However this version has had the melting routines removed. Therefore, another future piece of work would be to rebuild the melting routines and begin to model the evolution of rifted margins in three dimensions. Such a model would possibly be able to resolve the importance of segmentation on the melt structure (Carbotte et al., 2004) or how small-scale convection forms in three dimensions (Sparks and Parmentier, 1993).

It would be interesting to look at the edge effects of a thermal anomaly, in both two and three dimensions. In Chapters 4 and 5, I made the simple assumption that the thermal anomaly spreads to the edge of the model space. However, the thermal anomaly drained along the sublithospheric topography (Holbrook et al., 2001), possibly constrained by the Archean root of Greenland (Nielsen and Hopper, 2002) and by the prior extension that formed the the Hatton Trough, Hatton-Rockall Basin, Faroe Shetland Basin and Møre Basin. It would be interesting to explore the effects at the edge of such a thermal anomaly. The Iceland plume was likely centred to the north of Southeast Greenland, and is suggested to have drifted under Greenland from the east to west (Storey et al., 2007a). Therefore it would not be unreasonable to assume that the thermal anomaly did not extend as far to the west, under Hatton Bank. A thermal anomaly that is asymmetric with respect to the ridge axis may be the cause of the observed asymmetry in igneous thickness between the Southeast Greenland margin and conjugate Hatton Bank (Holbrook et al., 2001; Hopper et al., 2003).

Although the mantle is quite efficient in mixing (e.g. Van Keken and Ballentine, 1998), continuous differentiation processes predominantly during rifting and spreading, and depth-dependant density differences between separated continents, will lead to a mantle that is chemically heterogeneous on all scales (e.g. Anderson, 2006; Nakagawa and Tackley, 2005; Tackley, 2000). Such compositional heterogeneity has been proposed to be the cause of various melting anomalies, including those recently found at constructive boundaries (Lizarralde et al., 2007). The effects of melt depletion on major element composition and volatile content, or incomplete melt extraction, are proposed causes for various lithospheric and mantle discontinuities and anomalies (Rychert et al., 2006; Lizarralde et al., 2004; James and Assumpcao, 1995). These signatures are thought to

depend on the mantle composition, but as far as I am aware, they have not been verified within a dynamic model of rifting.

A major advance would be to explore the consequences of mantle heterogeneity on melting. Initial work has been made to study the effect of mantle primitive composition on the solidus and melting (Ito and Mahoney, 2005). It would be ideal to include a compositional mantle within the geodynamic model presented in this thesis. The effect of enriched regions of the mantle under rifting margins could then be tested. The anomalous rifting at the Gulf of California, where the rifting style varies from high magmatism to none of a short distance (Lizarralde et al., 2007), could then be explored. It has been suggested that the change in melting at this margin is due to rifting occurring above a heterogeneously depleted and enriched mantle (Lizarralde et al., 2007).

Such a model could be taken a step further, by the inclusion of estimates of the seismic velocity within the mantle and crust. Using the methods and algorithms of Goes (2004) and Connolly (2005), it would be possible to convert the mantle chemistry and temperature to form synthetic seismic pressure- and shear-wave profile. Such synthetic structures could be compared to the wide range of seismic constraints from the young rifted margins, such as the East Africa Rift or Rio Grande. Also, the effect of dehydration in the mantle on seismic velocities could be explored. The possible causes, dehydration or melt retention, of the observed seismic discontinuity under oceanic lithosphere could be tested (Rychert et al., 2006).

The drive to model the seismic properties of the mantle is mainly due to a lack of chemical data from rifted margins. Ideally there would be a greater wealth of analyses of the composition of basaltic rocks at rifted margins. There has recently been a great deal of focus on spreading centres, such as the East Pacific Rise. However, less attention is paid to the formation of these rifted margins. Arguments for thermal or chemical heterogeneity can be tested within a model of rift evolution. Yet without observations to test predictions against, these models remain purely mathematical.

Bibliography

Anderson, D. L., 2006. Speculations on the nature and cause of mantle heterogeneity. Tectonophysics 416, 7–22.

Armitage, J. J., Henstock, T. J., Minshull, T. A., Hopper, J. R., 2008. Modelling the composition of melts formed during continental break-up of the North Atlantic. Earth Planetary Science Letters 269, 248–258, doi: 10.1016/j.epsl.2008.02.024.

Asimow, P. D., Ghiorso, M. S., 1998. Algorithmic modifications extending MELTS to calculate subsolidus phase relations. American Mineralogist 83, 1127–1132.

Asimow, P. D., Hirschmann, M. M., Stopler, E. M., 1997. An analysis of variations in isentropic melt productivity. Philosophical Transactions of the Royal Society London A 355, 255–281.

Asimow, P. D., Longhi, J., 2004. The significance of multiple saturation points in the context of polybaric near-fractional melting. Journal of petrology 45, 2349–2397, doi:10.1093/petrology/egh043.

Aubaud, C., Hauri, E. H., Hirschmann, M. M., 2004. Hydrogen partition coefficients between nominally anhydrous minerals and basaltic melts. Geophysics Research Letters 31, doi: 10.1029/2004GL021341.

Baker, M. B., Stopler, E. M., 1994. Determining the composition of high-pressure mantle melts using diamond aggregates. Geochimica et Cosmochimica Acta 58, 2811–2827.

Barton, P. F., White, R. S., 1997. Crustal structure of the Edoras Bank margin and mantle thermal anomolies beneath the North Atlantic. Journal of Geophysical Research 103, 3109–3129.

Behn, M. D., Kelemen, P. B., 2003. Relationship between seismic P-wave velocity and the composition of anhydrous igneous and meta-igneous rocks. Geochemistry Geophysics Geosystems 4 (5), doi:10.1029/2002GC000393.

Berggren, W. A., Kent, D. V., Swisher III, C. C., Audry, M.-P., 1995. A revised Cenozoic geomoetry and chronostratigraphy. In: Berggren, W. A., Kent, D. V., Audry, M.-P., Hardenbol, J. (Eds.), Geochronology, Time Scales and Global Stratigraphic Correlation. Vol. SEPM special publication, 54. SEPM, pp. 129–212.

Boutilier, R. P., Keen, C. E., 1999. Small-scale convection and divergent plate boundaries. Journal of Geophysical Research 104, 7389–7403.

Bown, J. W., White, R. S., 1994. Variation with spreading rate of oceanic crust thickness and geochemistry. Earth and Planetary Science Letters 121, 435–449.

Bown, J. W., White, R. S., 1995. Effect of finite extension rate on melt generation at rifted continental margins. Journal of Geophysical Research 100, 18011–18029.

Braun, M. G., Hirth, G., Parmentier, E. M., 2000. The effects of deep damp melting on mantle flow and melt generation beneath mid-ocean ridges. Earth and Planetary Science Letters 176, 339–356.

Braun, M. G., Kelemen, P. B., 2002. Dunite distribution in the Oman Ophiolite: Implications for melt flux through porous dunite conduits. Geochemistry Geophysics Geosystems 3, doi: 10.1029/2001GC000289.

Brooks, A. N., Hughes, T. J. R., 1982. Streamline upwind/Petrov-Galerkin formulations for convection dominated flows with particular emphasis on the incompressible Navier-Stokes equations. Computer Methods in Applied Mechanics and Engineering 32, 199–259.

Buck, W. R., Parmentier, E. M., 1986. Convection beneath young ocean lithosphere: Implications for thermal structure and gravity. Journal of Geophysical Research 91 (B2), 1961–1974.

Bull, J. M., Masson, D. G., 1996. The southern margin of the Rockall Plateau: Stratigraphy, Tertiary volcanism, and plate tectonic evolution. Journal of the Geological Society, London 153, 601–612.

Cande, S. C., Kent, D. V., 1995. Revised calibration of the geomagnetic polarity timescale for the Late Cretaceous and Cenozoic. Journal of Geophysical Research 100, 6093–6095.

Carbotte, S. M., Small, C., Donnelly, K., 2004. The influence of ridge migration on the magnetic segmentation of mid-ocean ridges. Nature 429, 743–746.

Chopra, P. N., Paterson, M. S., 1984. The role of water in the deformation of dunite. Journal of Geophysical Research 89 (B9), 7861–7876.

Conder, J. A., 2007. Dynamically driven mantle flow and shear wave splitting asymmetry across the EPR, MELT area. Geophysical Research Letters 34, doi: 10.1029/2007GL030832.

Conder, J. A., Forsyth, D. W., Parmentier, E. M., 2002. Asthenospheric flow and asymmetry of the East Pacific Rise, MELT area. Journal of Geophysical Research 107, 2344–2357, doi: 10.1029/2001JB000807.

Connolly, J. A. D., 2005. Computation of phase equilibria by linear programming: A tool for geodynamic modelling and its application to subduction zone decarbonation. Earth and Planetary Science Letters 236, 524–541, doi:10.1016/j.epsl.2005.04.033.

Cordery, M. J., Phipps Morgan, J., 1993. Convection and melting at mid-ocean ridges. Journal of Geophysical Research 98, 19477–19504.

Corti, G., Manetti, P., 2006. Asymmetric rifts due to asymmetric Mohos: an experimental approach. Earth and Planetary Science Letters 245, 315–329.

Daly, E., Keir, D., Ebinger, C. J., Stuart, G. W., Bastow, I. D., Ayele, A., 2008. Crustal tomographic imaging of a transitional continental rift: the Ethiopian rift. Geophysics Journal InternationalDoi: 10.111/j.1365-246X.2007.03682.x.

Dasgupta, R., Hirschmann, M. M., Smith, N. D., 2007. Water follows carbon: CO_2 incites deep silicate melting and dehydration beneath mid-ocean ridges. Geology 35, 135–138.

Davis, M., Kusznir, N., 2002. Are buoyancy forces important during the formation of rifted margins? Geophysics Journal International 149, 524–533.

Dean, S. M., Murton, B. J., Minshull, T. A., Henstock, T. A., White, R. S., Submitted. An integrated kinematic and geochemical model to determine lithospheric extension and mantle temperatures from syn-rift volcanic composition. Earth and Planetary Science Letters.

Detrick, R. S., Buhl, P., Vera, E., Orcutt, J., Mutter, J., Madsen, J., Brocher, T., 1987. Multi-channel seismic imaging of a crustal magma chamber along the East Pacific Rise. Nature 326, 35–41.

Dietz, R. S., 1961. Continent and ocean basin evolution by spreading of the sea floor. Nature 190, 854–856.

Dixon, J. E., Leist, L., Langmuir, C., Schilling, J., 2002. Recycled dehydrated lithosphere observed in plume-influenced mid-ocean-ridge basalt. Nature 420, 385–388.

Dixon, J. E., Stopler, E., Delany, J. R., 1988. Infrared spectroscopic measurements of CO_2 and H_2O in Juan de Fuca Ridge basaltic glasses. Earth and Planetary Science Letters 90, 87–104.

Dunn, R. A., Forsyth, D. W., 2003. Imaging the transition between the region of mantle melt generation and the crustal magma chamber beneath southern East Pacific Rise with short-period Love waves. Journal of Geophysical Research 108, doi: 10.1029/2002JB002217.

Edwards, J. W. F., 2002. Development of the Hatton-Rockall Basin, North-East Atlantic Ocean. Marine and Petroleum Geology 19, 193–205.

England, P., 1983. Constraints on extension of continental lithosphere. Journal of Geophysical Research 88, 1145–1152.

Falloon, T. J., Green, D. H., 1987. Anhydrous partial melting of MORB pyrolite and other peridotite compositions at 10kbar: Implications for the origin of MORB glasses. Mineralogoy and Petrology 37, 181–219.

Falloon, T. J., Green, D. H., Hatton, C. J., Harris, K. L., 1988. Anhydrous partial melting of a fertile and depleted peridotite from 2 to 30 kb and application to basalt petrogenesis. Journal of Petrology 29, 1257–1282.

Fitton, J. G., Larsen, L. M., Saunders, A. D., Hardarson, B. S., Kempton, P. D., 2000. Palaeogene continental to oceanic magmatism on the SE Greenland continental margin at 63°N: a review of the results of ocean drilling program legs 152 and 163. Journal of Petrology 41, 951–966.

Fitton, J. G., Saunders, A. D., Larsen, L. M., Fram, M. S., Demant, A., Sinton, C., Leg 152 Shipboard Scientific Party, 1995. Magma sources and plumbing systems during break-up of the SE Greenland margin: preliminary results from ODP leg 152. Journal of the Geological Society, London 152, 985–990.

Fitton, J. G., Saunders, A. D., Larsen, L. M., Hardarson, B. S., Norry, M. J., 1998. Volcanic rocks from the southeast Greenland margin at 63°N: composition, petrogenisis, and mantle sources. Proceedings of the Ocean Drilling Program, Scientific Results 152, 331–350.

Fitton, J. G., Saunders, A. D., Norry, M. J., Hardson, B. S., Taylor, R. N., 1997. Thermal and chemical structure of the Iceland plume. Earth and Planetary Science Letters 153, 197–208.

Fleitout, L., Yuen, D., 1984. Steady-state, secondary convection beneath lithospheric plates with temperature- and pressure- dependant viscosity. Journal of Geophysical Research 89, 9227–9244.

Forsyth, D. W., 1993. Crustal thickness and the average depth and degree of melting in fractional melting models of passive flow beneath mid-ocean ridges. Journal of Geophysics Research 98, 16073–16079.

Forsyth, D. W., Webb, S. C., Dorman, L. M., Shen, Y., 1998. Phase velocities of Rayleigh waves in the MELT experiment on the East Pacific Rise. Science 280, 1235–1238.

Fowler, S. R., White, R. S., Spence, G. D., Westbrook, G. K., 1989. The Hatton Bank continental margin - II. Deep structure for two-ship expanding spread seismic profiles. Geophysical Journal International 96, 295–309.

Fram, M. S., Lesher, C. E., 1993. Geochemical constraints on mantle melting during the creation of the North Atlantic basin. Nature 363, 712–715.

Fram, M. S., Lesher, C. E., Volpe, A. M., 1998. Mantle melting systematics: transition from continental to oceanic volcanism on the Southeast Greenland margin. Proceedings of the Ocean Drilling Program, Scientific Results 152, 373–386.

Gans, K. D., Wilson, D. S., MacDonald, K. C., 2003. Pacific Plate gravity lineaments: Diffuse extension or thermal contraction? Geochemistry Geophysics Geosystems 4 (9), doi: 10.1029/2002GC000465.

Ghiorso, M. S., Sack, R. O., 1995. Chemical mass-transfer in magmatic processes IV. A revised and internally consistent thermodynamic model for the interpolation and extrapolation of liquid-solid equilibria in magmatic systems at elevated temperatures and pressures. Contributions to Mineralogy and Petrology 119, 197–212.

Goes, S., 2004. Synthetic seismic signature of thermal mantle plumes. Earth and Planetary Science Letters 218, 403–419.

Grove, T. L., Chatterjee, N., Parman, S. W., Médard, E., 2006. The influence of H_2O on mantle wedge melting. Earth and Planetary Science Letters 249, 74–89, doi: 10.1016/j.epsl.2006.06.043.

Haxby, W. F., Weissel, J. K., 1986. Evidence for small-scale mantle convection from Seasat altimeter data. Journal of Geophysical Research 91 (B3), 3507–3520.

Henstock, T. J., Woods, A. W., White, R. S., 1993. The accretion of oceanic crust by episodic sill intrusion. Journal of Geophysical Research 98, 4143–4161.

Herzberg, C., 2004. Partial crystallisation of mid-ocean ridge basalts in the crust and mantle. Journal of Petrology 45, 2389–2405, doi: 10.1093/petrology/egh040.

Herzberg, C., Asimow, P. D., Arndt, N., Niu, Y., Lesher, C. M., Fitton, J. G., Cheedle, M. J., Saunders, A. D., 2007. Temperatures in ambient mantle and plumes: Constraints from basalts, picrites, and komatiites. Geochemistry Geophysics Geosystems 8, doi:10.1029/2006GC001390.

Herzberg, C., O'Hara, M. J., 2002. Plume-associated ultramafic magmas of phanerzoic age. Journal of Petrology 43, 1857–1883.

Hess, H. H., 1962. History of ocean basins. In: Engel, A. E. H., James, H. L., Leonard, B. F. (Eds.), Petrologic Studies: a volume to honour A. F. Buddington. Geological Society of America, Boulder, pp. 599–620.

Hirose, K., Kushiro, I., 1993. Partial melting of dry peridotites at high pressures: determination of compositions of melt segregated from peridiotite using aggregates of diamonds. Earth Planetary Science Letters 114, 477–489.

Hirschmann, M. M., 2006. Water, melting, and the deep Earth H_2O cycle. Annual Review of Earth Planetary Science 34, 629–653, doi:10.1146/annurev.earth.34.031405.125211.

Hirschmann, M. M., Asimow, P. D., Ghiorso, M. S., Stopler, E. M., 1998. Calculation of peridotite partial melting from thermodynamic models of minerals and melts. III. Controls on isobaric melt production and the effect of water on melt production. Journal of Petrology 40 (5), 831–851.

Hirschmann, M. M., Stopler, E. M., Ghiorso, M. S., 1994. Perspectives on shallow mantle melting from thermodynamic calculations. Mineralogical Magazine A 58, 418–419.

Hirth, G., Kohlstedt, D. L., 1995. Experimental constraints on the dynamics of the partially molten upper mantle 2. Deformation in the dislocation regime. Journal of Geophysical Research 100 (B8), 15441–15449.

Hirth, G., Kohlstedt, D. L., 1996. Water in the oceanic upper mantle: implications for rheology, melt extraction and the evolution of the lithosphere. Earth and Planetary Science Letters 144, 93–108.

Holbrook, W. S., Larsen, H. C., Korenaga, J., Dahl-Jensen, T., Reid, I. D., Kelemen, P. B., Hopper, J. R., Kent, G. M., Lizarradle, D., Bernstein, S., Detrick, R. S., 2001. Mantle thermal structure and active upwelling during continental breakup in the north atlantic. Earth and Planetary Science Letters 190, 251–266.

Hopper, J. R., Dahl-Jensen, T., Holbrook, W. S., Larsen, H. C., Lizarradle, D., Korenaga, J., Kent, G. M., Kelemen, P. B., 2003. Structure of the SE Greenland margin from seismic reflection and refraction data: Implications for nascent spreading centre subsidence and asymmetric crustal accretion during North Atlantic opening. Journal of Geophysical Research 108, doi: 10.1029/2002JB001996.

Huang, J., Zhong, S., 2005. Sublithospheric small-scale convection and its implications for the residual topography at old ocean basins and the plate model. Journal of Geophysical Research 110, doi: 10.1029/2004JB003153.

Hughes, T. J. R., 2000. The finite element method. Dover.

Isacks, B., Oliver, J., Sykes, L. R., 1968. Seismology and the new global tectonics. Journal of Geophysics Research 73, 5855–5899.

Ito, G., 2001. Reykjanes 'v'-shaped ridges originating from a pulsing and dehydrating mantle plume. Nature 411, 681–684.

Ito, G., Lin, J., Gable, C. W., 1996. Dynamics of mantle flow and melting at ridge-centred hotspot: Iceland and the Mid-Atlantic Ridge. Earth and Planetary Science Letters 144, 53–74.

Ito, G., Mahoney, J. J., 2005. Flow and melting of a heterogeneous mantle: 1. Method and importance to the geochemistry of ocean island and mid-ocean ridge basalts. Earth and Planetary Science Letters 230, 29–46.

Ito, G., Shen, Y., Hirth, G., Wolfe, C. J., 1999. Mantle flow, and dehydration of the Iceland mantle plume. Earth and Planetary Science Letters 165, 81–96.

Jacoby, W. R., Weigel, W., Fedorova, T., 2007. Crustal structure of the Reykjanes Ridge near $62°n$, on the basis of seismic refraction and gravity data. Journal of Geogynamics 43, 55–72.

James, J. C. V. D. E., Assumpcao, M., 1995. Seismic evidence for a fossil mantle plume beneath south america and implications for plate driving forces. Nature 378, 25–31.

Jaques, A. L., Green, D. H., 1980. Anhydrous melting of peridotite at 0-15kb pressure and the genisis of tholeiitic basalts. Contributions to Mineralogy and Petrology 73, 287–310.

Jurine, D., Jaupart, C., Brandeis, G., Tackley, P. J., 2005. Penetration of mantle plumes through depleted lithosphere. Journal of Geophysical Research 110 (B10104), doi: 10.1029/2005JB003751.

Karato, S., Jung, H., 1998. Water, partial melting and the origin of the seismic low velocity and high attenuation zone in the upper mantle. Earth and Planetary Science Letters 157, 193–207.

Karato, S., Wu, P., 1993. Rheology of the upper mantle: A synthesis. Science 260, 771–777.

Katz, R. F., Spiegelman, M., Carbotte, S. M., 2004. Ridge migration, asthenospheric flow and the origin of magmatic segmentation in the global mid-ocean ridge system. Geophysical Research Letters 31, doi:10.029/2004GL020388.

Katz, R. F., Spiegelman, M., Holtzman, B., 2006. The dynamics of melt and shear localisation in partially molten aggregates. Nature 442, 676–679, doi: 10.1038/nature05039.

Kelemen, P., Holbrook, W., 1995. Origin of thick, high velocity igneous crust along the U.S. East Coast margin. Journal of Geophysical Research 100, 10077–10094.

Kelemen, P. B., Hirth, G., Shimizu, N., Spiegelman, M., Dick, H. J. B., 1997a. A review of melt migration processes in the adiabatically upwelling mantle beneath oceanic spreading ridges. Philisophical Transactions of the Royal Society London A 355, 283–318.

Kelemen, P. B., Koga, K., Shimizu, N., 1997b. Geochemistry of gabbro sills in the crust/mantle transition zone of the Oman ophiolite: Implications for the origin of the oceanic lower crust. Earth and Planetary Science Letters 146, 475–488.

Kendall, J., Stuart, G. W., Ebinger, C. J., Bastwo, I. D., Keir, D., 2005. Magma-assisted rifting in ethiopia. Nature 433, 146–148, doi: 10.1038/nature03161.

Klein, E. M., Langmuir, C. H., 1987. Global correlations of ocean ridge basalt chemistry with axial depth and crustal thickness. Journal of geophysical research 92, 8089–8115.

Klein, E. M., Plank, T., Langmuir, C. H., 1991. Constraints on models for mantle melting beneath ocean ridges. RIDGE Events 2, 11–12.

Kojitani, H., Akaogi, M., 1997. Melting enthalpies of mantle peridotite: calorimetic determinations in the system CaO-MgO-Al_2O_3-SiO_2 and application to magma generation. Earth and Planetary Science Letters 153, 209–222.

Korenaga, J., 2007. Thermal cracking and the deep hydration of oceanic lithosphere: A key to the generation of plate tectonics? Journal of Geophysical research 112, doi: 10.1029/2006JB004502.

Langmuir, H. H., Klein, E. M., Plank, T., 1992. Petrological systematics of mid-ocean ridge basalts: constraints on melt generation beneath ocean ridges. In: Mantle flow and melt generation at mid-ocean ridges. Vol. Geophysical Monograph 71. American Geophysical Union, pp. 183–280.

Larsen, H., Saunders, A., 1998. Tectonism and volcanism at the southeast Greenland rifted margin: A record of plume impact and later continental rupture. Proceedings of the Ocean Drilling Program, Scientific Results 152, 503–533.

Larsen, H. C., Saunders, H. C., Clift, P. D., *et al* (Eds.), 1994. Proceedings of the Ocean Drilling Program, Scientific Results, 152. Ocean Drilling Program, College Station, TX.

Larsen, L. M., Fitton, J. G., Fram, M. S., 1998. Volcanic rocks of the southeast Greanland margin in comparison with other parts of the north Atlanic tertiary igneous province. Proceedings of the Ocean Drilling Program, Scientific Results 152, 315–330.

Larsen, L. M., Fitton, J. G., Saunders, A. D., 1999. Composition of volcanic rocks from the Southeast Greenland margin, leg 163: major and trace element geochemistry. Proceedings of the Ocean Drilling Program, Scientific Results 163, 63–75.

Le Pichon, X., Sibuet, J., 1981. Passive margins: a model of formation. Journal of Geophysical Research 86, 3708–3720.

Lizarralde, D., Axen, G. J., Brown, H. E., Fletcher, J. M., Gonzalez-Fernandez, A., Harding, A. J., Holbrook, W. S., Kent, G. M., Paramo, P., Sutherland, F., Umhoefer, P. J., 2007. Variation in styles of rifting in the Gulf of California. Nature 448, doi: 10.1038/nature06035.

Lizarralde, D., Gaherty, J. B., Collins, J. A., Hirth, G., Kim, S. D., 2004. Spreading-rate dependence of melt extraction at mid-ocean ridges from mantle seismic refraction data. Nature 432, 744–747.

Mackenzie, G. D., Thybo, H., Maguire, P. K. H., 2005. Crustal velocity structure across the Main Ethiopian Rift: results from two-dimensional wide-angle seismic modelling. Geophysics Journal International 162, 994–1006, doi: 10.1111/j.1365-246X.2005.02710.x.

Maclennan, J., Hulme, T., Singh, S. C., 2004. Thermal models of oceanic crustal accretion: linking geophysical, geological and petrological observations. Geochemistry Geophysics Geosystems 5 (2), doi: 10.1029/2003GC000605.

Maclennan, J., Hulme, T., Singh, S. C., 2005. Cooling of the lower oceanic crust. Geology 33, 357–360, doi: 10.1130/G21207.1.

McKenzie, D., Jackson, J., Priestley, K., 2005. Thermal structure of oceanic and continental lithosphere. Earth and Planetary Science Letters 233, 337–349.

McKenzie, D., O'Nions, R. K., 1991. Partial melt distribution from inversion of rare earth element concentrations. Journal of Petrology 32, 1021–1091.

McKenzie, D. P., 1967. Some remarks on heat flow and gravity anomalies. Journal of Geophysical Research 72, 6261–6273.

McKenzie, D. P., 1978. Some remarks on the development of sedimentary basins. Earth and Planetary Science Letters 40, 25–32.

McKenzie, D. P., 1984. The generation and compaction of partially molten rock. Journal of Petrology 25, 713–765.

McKenzie, D. P., 1985. The extraction of magma from the crust and mantle. Earth Planetary Science Letters 74, 81–91.

McKenzie, D. P., Bickle, M. J., 1988. The volume and composition of melt generated by extension of the lithosphere. Journal of Petrology 29, 625–679.

Mei, S., Kohlstedt, D. L., 2000. Influence of water on plastic deformation of olivine aggregates 2. Dislocation creep. Journal of Geophysical Research 105 (B9), 21471–21481.

Michael, P. J., 1988. The concentration, behaviour and storage of H_2O in suboceanic upper mantle: implications for mantle metasomatism. Geochimica et Cosmochimica Acta 52, 555–566.

Michael, P. J., 1995. Regionally distinctive sources of depleted MORB: evidence from trace elements and H_2O. Earth Planetary Science Letters 131, 301–320.

Minshull, T. A., Dean, S. M., White, R. S., Whitmarsh, R. B., 2001. Anomalous melt production after continental break-up in the southern Iberia Abyssal Plain. Geological Society London Special Publications 187, 537–550.

Mittelsteadt, E., Ito, G., Behn, M. D., 2008. Mid-ocean ridge jumps associated with hotspot magmatism. Earth and Planetary Science Letters 266, 256–270, doi: 10.1016/j.epsl.2007.10.055.

Mjelde, R., Raum, T., Myhren, B., Shimamura, H., Murai, Y., Takanami, T., Karpz, R., Naess, U., 2005. Continent-ocean transition on the Vøring Plateau, NE Atlantic, derived from densely spaced ocean bottom seismometer data. Journal of Geophysical Research 110, doi:10.1029/2004JB003026.

Moresi, L., Solomatov, V. S., 1995. Numerical investigation of 2D convection with extremely large viscosity variations. Physics of Fluids 7, 2154–2162.

Moresi, L., Zhong, S., Gurnis, M., 1996. The accuracy of finite element solutions of Stokes' flow with strongly varying viscosity. Physics of the Earth and Planetary Interiors 97, 83–94.

Morgan, W. J., 1968. Rises, trenches, great faults and crustal blocks. Journal of Geophysical Research 73, 1959–1982.

Mutter, J. C., Buck, W. R., Zehnder, C. M., 1988. Convective partial melting 1. A model for the formation of thick basaltic sequences during the initiation of spreading. Journal of Geophysical Research 93, 1031–1048.

Nakagawa, T., Tackley, P. J., 2005. The interaction between the post-perovskite phase change and a thermo-chemical boundary layer near the core mantle boundary. Earth and Planetary Science Letters 238, 204–216.

Newman, R., White, N., 1997. Rheology of the continental lithosphere inferred from sedimentary basins. Nature 385, 621–624.

Nielsen, T. K., Hopper, J. R., 2002. Formation of volcanic rifted margins: are temperature anomalies required? Geophysical Research Letters 29, doi: 10.1029/2002GL015681.

Nielsen, T. K., Hopper, J. R., 2004. From rift to drift: mantle melting during continental breakup. Geochemistry Geophysics Geosystems 5, doi: 10.1029/2003GC000662.

Nisbet, E. G., Cheadle, M. J., Arndt, N. T., Bickle, M. J., 1993. Constraining the potential temperature of the Archaean mantle: a review of the evidence from komaliites. Lithos 30, 291–308.

Niu, Y., 1997. Mantle melting and melt extraction processes beneath ocean ridges: Evidence from abyssal peridotites. Journal of Petrology 38, 1047–1074.

Niu, Y., Batiza, R., 1991. An empirical method for calculating melt compositions produced beneath mid-ocean ridges: application for axis and off-axis (seamounts) melting. Journal of Geophysical Research 96 (B13), 21753–21777.

Parmentier, E. M., Phipps Morgan, J., 1990. Spreading rate dependance of three-dimensional structure in oceanic spreading centres. Nature 348, 325–328.

Parsons, B., McKenzie, D., 1978. Mantle convection and the thermal structure of the plates. Journal of Geophysical Research 83 (B9), 4485–4495.

Parsons, B., Sclater, J. G., 1977. An analysis of the variation of ocean floor bathymetry and heat flow with age. Journal of Geophysical Research 82, 803–827.

Peate, I. U., Larsen, M., Lesher, C. E., 2003. The transition from sedimentation to flood volcanism in the Kangerlussuaq Basin, East Greenland: basaltic pyroclastic volcanism during initial Palaeogene continental break-up. Journal of the Geological Society, London 160, 759–772.

Peirce, C., Gardiner, A., Sinha, M., 2005. Temporal and spatial cyclicity of accretion at slow-spreading ridges – evidence from the Reykjanes Ridge. Geophysics Journal International 163, 56–78.

Phipps Morgan, J., 2001. Thermodynamics of pressure release melting of a veined plum pudding mantle. Geochemistry Geophysics Geosystems 2, doi: 10.1029/2000GC000049.

Plank, T., Spiegelman, M., Langmuir, C. H., Forsyh, D. W., 1995. The meaning of 'mean F': Clarifying the mean extent of melting at ocean ridges. Journal of Geophysical Research 100 (B8), 15045–15052.

Reid, I., Jackson, H. R., 1981. Oceanic spreading rate and crustal thickness. Marine Geophysical Researches 5, 165–172.

Richter, F. M., Parsons, B., 1975. On the interaction of two scales of convection in the mantle. Journal of Geophysical Research 80, 2529–2541.

Robinson, C. J., Bickle, M. J., Minshull, T. A., White, R. S., Nichols, A. R. L., 2001. Low degree melting under the Southwest Indian Ridge: the roles of mantle temperature, conductive cooling and wet melting. Earth and Planetary Science Letters 188, 383–398.

Rychert, C. A., Fischer, K. M., Rondenay, S., 2005. A sharp lithosphere-ashenosphere boundary imaged beneath eastern North America. Nature 436, 542–545, doi: 10.1038/nature03904.

Rychert, C. A., Fischer, K. M., Rondenay, S., 2006. A sharp lithosphere-asthenosphere boundary imaged beneath eastern North America. Nature 436, doi: 10.1038/nature03904.

Sawyer, D. S., 1985. Brittle failure in the upper mantle during extension of continental lithosphere. Journal of Geophysical Research 90, 3021–3025.

Scott, D. R., 1992. Small-scale convection and mantle melting beneath mid-ocean ridges. In: Phipps Morgan, J., Blackman, D. K., Sinton, J. M. (Eds.), Mantle flow and melt

generation at mid-ocean ridges. Vol. Geophysical Monograph 71. American Geophysical Union, pp. 327–352.

Scott, D. R., Stevenson, D. J., 1989. A self-consistent model of melting, magma migration and buoyancy-driven circulation beneath mid-ocean ridges. Journal of Geophysical Research 94 (B3), 2973–2988.

Searle, R. C., Bralee, A. V., 2007. Asymmetric generation of oceanic crust at the ultra-slow spreading Southwest Indian Ridge, 64°N. Geochemistry Geophysics Geosystems 8, doi: 10.1029/2006GC001529.

Shah, A. K., Buck, W. R., 2006. The rise and fall of axial highs during ridge jumps. Journal of Geophysical Research 111, doi:10.1029/2005JB003657.

Shillington, D. J., Holbrook, W. S., Van Avendonk, H. J. A., Tucholke, B. E., Hopper, J. R., Louden, K. E., Larsen, H. C., Nunes, G. T., 2006. Evidence for asymmetric rifting and slow incipient oceanic accretion from seismic reflection data on the Newfoundland margin. Journal of Geophysical Research 111 (B09402), doi:10.1029/2005JB003981.

Sinha, M. C., Constable, S. C., Pierce, C., White, A., Heinson, G., MacGregor, L., Navin, D. A., 1998. Magmatic processes at slow spreading ridges: implications of the RAMESSES experiment at $57°\,45'$ n on the Atlantic Ridge. Geophysics Journal International 135, 731–745.

Sinha, M. C., Evans, R. L., 2004. Geophysical constraints upon the thermal regime of the ocean crust. In: Mid-Ocean Ridges: Hydrothermal Interactions Between the Lithosphere and Oceans. Vol. 148 of Geophysical Monograph Series. American Geophysical Union, pp. 19–62, doi: 10.1029/148GM02.

Sinton, C. W., Duncan, R. A., 1998. ^{40}Ar-^{39} ages of lavas from the southeast Greenland margin, ODP leg 152, and the Rockhall plateau, DSDP 81. Proceedings of the Ocean Drilling Program, Scientific Results 152, 387–402.

Smallwood, J. R., White, R. S., 1998. Crustal accretion at the Reykjanes Ridge, 61 degrees - 62 degrees n. Journal of Geophysical Research 103, 5185–5201.

Smallwood, J. R., White, R. S., 2002. Ridge-plume interaction in the North Atlantic and its influence on continental breakup and seafloor spreading. In: Jolley, D. W., Bell, B. R. (Eds.), The North Atlantic igneous province: Stratigraphy, tectonic, volcanic and magmatic processes. The Geological Society of London, pp. 15–37.

Smith, L. K., White, R. S., Kusznir, N. J., iSIMM Team, 2005. Structure of the hatton basin and adjacent continental margin. In: Doré, A. G., Vining, B. A. (Eds.), Petroleum Geology: North-West Europe and Global Perspectives - Proceedings of the 6th Petroleum Geology Conference. Geological Society, London, pp. 947–956.

Smith, P. M., Asimow, P. D., 2005. Adiabat 1ph: a new public front-end to the MELTS, pMELTS and pHMELTS models. Geochemistry Geophysics Geosystems 6, doi:10.1029/2004GC000816.

Smythe, D. K., 1989. Rockall Trough - Cretaceous or late Palaeozoic. Scottish Journal of Geology 25, 5–43.

Sobolev, S. V., Babeyko, A. Y., 1994. Modelling of mineralogical composition, density and elastic wave velocities in anhydrous magmatic rocks. Surveys in Geophysics 15, 515–544.

Solomatov, V. S., 1995. Scaling of temperature- and stress-dependent viscosity convection. Physics of Fluids 7, 266–274.

Solomatov, V. S., Moresi, L., 1996. Stagnant lid convection on Venus. Journal of Geophysical Research 101, 4737–4753.

Solomatov, V. S., Moresi, L.-N., 2000. Scaling of time-dependant stagnant lid convection: Application to small-scale convection on earth and other terrestrial planets. Journal of Geophysical Research 105 (B9), 21795–21817.

Sparks, D. W., Parmentier, E. M., 1993. The structure of three-dimensional convection beneath oceanic spreading centres. Geophysical Journal International 112, 81–91.

Spiegelman, M., 1996. Geochemical consequences of melt transport in 2-D: The sensitivity of trace elements to mantle dynamics. Earth and Planetary Science Letters 139, 115–132.

Spiegelman, M., Kelemen, P. B., Aharononv, E., 2001. Causes and consequences of flow organisation during melt transport: the reaction infiltration instability in compactible media. Journal of Geophysical Research 106 (B2), 2061–2077.

Spiegelman, M., McKenzie, D., 1987. Simple 2-D models for melt extraction at mid-ocean ridges and island arcs. Earth and Planetary Science Letters 83, 137–152.

Stein, C. A., Stein, S., 1992. A model for the global variation in oceanic depth and heat flow with lithosphere age. Nature 359, 123–129.

Storey, M., Duncan, R. A., Pederson, A. K., Larsen, L. M., Larsen, H. C., 1998. ^{40}Ar/^{39}Ar geochronolgy of the West Greenland Tertiary volcanic province. Earth and Planetary Science Letters 160, 569–586.

Storey, M., Duncan, R. A., Swisher III, C. C., 2007a. Paleocene-Eocene thermal maximum and opening of the Northeaast Atlantic. Science 316, 587–589, doi: 10.1126/science.1135274.

Storey, M., Duncan, R. A., Tegner, C., 2007b. Timing and duration of volcanism in the North Atlantic Igneous Province: Implications for geodynamics and links to the Iceland hotspot. Chemical Geology 241, 264–281.

Tackley, P. J., 2000. Mantle convection and plate tectonics: Toward an integrated physical and chemical theory. Science 288, 2002–2007.

Tegner, C., Duncan, R. A., 1999. ^{40}Ar-^{39} chronology for the volcanic history of the southeast Greenland rifted margin. Proceedings of the Ocean Drilling Program, Scientific Results 163, 53–63.

Tegner, C., Lesher, C. E., Larsen, L. M., Watt, W. S., 1998. Evidence from the rare-earth-element record of mantle melting for cooling of the Tertiary Iceland plume. Nature 395, 591–594.

Thy, P., Lesher, C. E., Fram, M. S., 1998. Low pressure experimental constraints on the evolution of basaltic lavas from site 917, southeast Greenland continental margin. Proceedings of the Ocean Drilling Program, Scientific Results 152, 359–372.

Toomey, D. R., Wilcock, W. S. D., Conder, J. A., Forsyth, D. W., Blundy, J. D., Parmetier, E. M., Hammond, W. C., 2002. Asymmetric mantle dynamics in the MELTregion of the East Pacific Rise. Earth and Planetary Science Letters 200, 287–295.

Turcotte, D. L., Oxburgh, E. R., 1967. Finite amplitude convective cells and continental drift. Journal of Fluid Mechanics 28, 29–42.

Turcotte, D. L., Schubert, G., 2002. Geodynamics, 2nd Edition. Cambridge University Press, Cambridge.

van Huenen, J., van Wijk, J., 2007. Numerical models of lithosphere-mantle interaction at continental rift zones. Eos Trans. AGU 88 (52), fall Meet. Suppl. Abstract T11C-0721.

Van Keken, P. E., Ballentine, C. J., 1998. Whole-mantle versus layered mantle convection and the role of a high-viscosity lower mantle in terrestrial volatile evolution. Earth and Planetary Science Letters 156, 19–32.

Verhoef, J., Roest, W. R., Macnab, R., Members of the Project Team, 1996. Arctic and North Atlantic Oceans and adjacent land areas, magnetic anomalies. Geological Survey of Canada, Ottawa, Open File 3125a.

Vine, F. J., 1966. Spreading of the ocean floor: new evidence. Science 154, 1405–1415.

Vine, F. J., Mathews, D. H., 1963. Magnetic anomalies over oceanic ridges. Nature 199, 947–949.

Voss, M., Jokat, W., 2007. Continent-ocean transition and voluminous magmatic underplating derived from P-wave velocity modelling of the East Greenland continental margin. Geophysics Journal International 170, 580–605.

Watson, S., 1991. Hotspots and volcanism. Ph.D. thesis, Cambridge Unversity.

Watson, S., McKenzie, D., 1991. Melt generation by plumes: a study of Hawiian volcanism. Journal of Petrology 32, 501–537.

Weertman, J., Weertman, J. R., 1975. High temperature creep of rock and mantle viscosity. Annual Review of Earth and Planetary Sciences 3, 293–315.

Weir, N. R., White, R. S., Brandisdóttir, B., Einarsson, P., Shimamura, H., Shiobara, H., the RISE Fieldwork Team, 2001. Crustal structure of the northern Rekjanes Ridge and Reykjanes Peninsula, southwest Iceland. Journal of Geophysical Research 106, 6347–6368.

White, R. S., McKenzie, D., O'Nions, R. K., 1992. Oceanic crustal thickness from seismic measurements and rare earth element inversions. Journal of Geophysical Research 97 (B13), 19683–19715.

White, R. S., McKenzie, D. P., 1989. Magmatism at rift zones: the generation of volcanic continental margins and flood basalts. Journal of Geophysical Research 94, 7685–7729.

White, R. S., Minshull, T. A., Bickle, M. J., Robinson, C. J., 2001. Melt generation at very slow-spreading oceanic ridges: Constraints from geochemical and geophysical data. Journal of Petrology 42 (6), 1171–1196.

White, R. S., Smith, L. K., Roberts, A. W., Christie, P. A. F., Kusznir, N. J., the rest of the iSIMM Team, 2008. Lower-crustal intrusion on the North Atlantic continental margin. Nature 452, 460–465, doi: 10.1038/nature06687.

White, R. S., Spence, G. D., Fowler, S. R., McKenzie, D. P., Westbrook, G. K., Bowen, A. N., 1987. Magmatism at rifted continental margins. Nature 330, 439–444.

Williamson, M., Courtney, R. C., Keen, C. E., Dehler, S. A., 1995. The volume and rare Earth concentrations of magmas generated during finite stretching of the lithosphere. Journal of Petrology 36, 1433–1453.

Wilson, J. T., 1962. Cabot fault, an Appalachian equivalent of the San Andreas and Great Glen faults and some implications for continental displacement. Nature 195, 135–138.

Wilson, J. T., 1963. Evidence from islands on the spreading of ocean floors. Nature 197, 536–538.

Winterer, E. L., Sandwell, D. T., 1987. Evidence from en-echelon cross-grain ridges for tensional cracks in the Pacific plate. Nature 329, 534–537.